
Electronic Thesis and Dissertation Repository

11-28-2014 12:00 AM

A DC Distribution System for Power System Integration of Plug-In Electric Vehicles; Modeling, Stability and Operation

Mansour Tabari
The University of Western Ontario

Supervisor
Dr. Amirnaser Yazdani
The University of Western Ontario

Graduate Program in Electrical and Computer Engineering
A thesis submitted in partial fulfillment of the requirements for the degree in Doctor of Philosophy
© Mansour Tabari 2014

Follow this and additional works at: <https://ir.lib.uwo.ca/etd>



Part of the [Controls and Control Theory Commons](#), and the [Power and Energy Commons](#)

Recommended Citation

Tabari, Mansour, "A DC Distribution System for Power System Integration of Plug-In Electric Vehicles; Modeling, Stability and Operation" (2014). *Electronic Thesis and Dissertation Repository*. 2624.
<https://ir.lib.uwo.ca/etd/2624>

This Dissertation/Thesis is brought to you for free and open access by Scholarship@Western. It has been accepted for inclusion in Electronic Thesis and Dissertation Repository by an authorized administrator of Scholarship@Western. For more information, please contact wlsadmin@uwo.ca.

A DC DISTRIBUTION SYSTEM FOR POWER SYSTEM
INTEGRATION OF PLUG-IN ELECTRIC VEHICLES; MODELING,
STABILITY, AND OPERATION
(Thesis format: Monograph)

by

Mansour Tabari

Graduate Program in Electrical and Computer Engineering

Supervisor:

Dr. Amirnaser Yazdani

A thesis submitted in partial fulfillment
of the requirements for the degree of
Doctor of Philosophy

The School of Graduate and Postdoctoral Studies
Western University
London, Ontario, Canada

© Mansour Tabari 2014

Abstract

This thesis is mainly focused on (i) modeling of dc distribution systems for power system integration of plug-in electric vehicles (PEVs), (ii) proposing a method to enhance the stability of the dc distribution systems, and (iii) proposing an energy management strategy to control the power flow in the dc distribution system. The dc distribution system is expected to be more efficient and economical than a system of ac-dc battery chargers directly interfaced with an ac grid.

In the first part, a systematic method for developing a model for a dc distribution system, based on the configuration of the system is proposed. The developed model is of the matrix form and, therefore, can readily be expanded to represent a dc distribution system of any desired number of dc-dc converters. The model captures both the steady-state and dynamic characteristics of the system, and includes the port capacitors of the converters, as well as the interconnection cables. Thus, it can be used for identifying the condition for the existence of a steady state, as well as for stability analysis.

In the second part, the thesis proposes a method for enhancing the stability of the dc distribution system. Using a nonlinear control strategy, the proposed stability enhancement method mitigates the issue of instability by altering the power setpoints of the battery chargers, bidirectional dc-dc converters, without a need for changing system parameters or hardware. The thesis presents mathematical models for the original and modified systems and demonstrates that the proposed technique expands the stable operating region of the dc distribution system.

The thesis further proposes an energy management strategy (EMS) for the dc distribution system. Using an on-line constrained optimization algorithm, the proposed EMS offers two energy exchange options to the PEV owners: (1) The fast energy exchange option for the owners wishing to minimize the energy exchange time and (2) The optimal energy exchange option for the owners intend to either minimize their costs of charging or maximize their revenues through selling their stored energy. The proposed EMS seamlessly handles all charging/discharging requests from the PEV owners with different options.

Keywords: Constant-power property, dc distribution system, dc-voltage control, plug-in electric vehicle, energy management strategy, load management, modeling, optimal charging, smart grid, stability, voltage-sourced converter.

To:

*my wife, Rokhand, for her generous support,
and the joy of our life, Abtin.*

Acknowledgement

I would like to express my sincere gratitude to Dr. Amirnaser Yazdani for his excellent supervision, bright ideas, and continuous encouragement throughout the course of this research. It has been a great privilege for me to pursue my higher education under his supervision.

Also, the financial support provided by Dr. Amirnaser Yazdani and Western University is gratefully acknowledged.

Contents

Abstract	ii
Dedication	iii
Acknowledgements	iv
List of Figures	ix
List of Tables	xiii
List of Appendices	xiv
List of Abbreviations	xv
List of Nomenclature	xvi
1 Introduction	1
1.1 Statement of Problem and Thesis Objectives	1
1.2 Background	2
1.2.1 Electric Vehicle	2
1.2.2 Battery Chargers for Electric Vehicles	3
1.2.3 Power System Integration of Electric Vehicles	4
1.3 Thesis Contributions	7
1.4 Literature Survey Pertinent to Thesis Contributions	9
2 Modeling of the DC Distribution System	13
2.1 Introduction	13
2.2 System Configuration and Components	14
2.2.1 Central VSC	15
Current-Controlled Scheme	15

Controlled dc-Voltage Power Port	18
2.2.2 dc-dc Converters	19
2.3 Mathematical Model	21
2.3.1 Existence of a steady state	23
2.3.2 State-space model	25
2.4 Simulation Results	30
2.4.1 Realistic Battery Model	30
2.4.2 Case 1: Stable Pre- and Post-Disturbance Operation	32
2.4.3 Case 2: Sensitivity to Cable Length	33
2.4.4 Case 3: Sensitivity to Network-Side Capacitances	34
2.4.5 Case 4: Sensitivity to Power Absorption	35
2.4.6 Case 5: Unstable Post-Disturbance Operation	36
2.5 dc System with Multiple Nodes of Coupling	36
2.6 Conclusion	39
3 Stability Enhancement of the DC Distribution System	40
3.1 Introduction	40
3.2 System Configuration	41
3.3 Mathematical Model	42
3.3.1 Central VSC	42
3.3.2 dc-dc converters	44
3.4 Stability Enhancement	47
3.5 Simulation Results	52
3.6 Stability Enhancement for a dc System with Single dc-dc Converter	55
3.7 Stability Enhancement for a dc System with n dc-dc Converters	60
3.8 Conclusion	64
4 Energy Management Strategy	66
4.1 Introduction	66
4.2 DC distribution System	67
4.3 Constrained Optimization Problem	70
4.4 Operation of EMS	72
4.5 Determination of Energy Exchange Intervals	75
4.6 Simulation Results	77
4.6.1 Case I: residential parking lot; evening and night time	78

Scenario I-1	78
Scenario I-2	78
Scenario I-3	79
Scenario I-4	79
Scenario I-5	80
4.6.2 Case II: business area parking lot; day time	83
Scenario II-1	83
Scenario II-2	84
Scenario II-3	85
Scenario II-4	85
4.7 Conclusion	87
5 Summary, Conclusions, and Future Work	89
5.1 Summary	89
5.2 Conclusions	90
5.3 Future Work	91
A Modeling of a droop-based dc-dc converter in a dc system	93
B Positive-Definiteness of R and L matrices	96
C Proof of Equation (2.52)	98
D Study System Parameters for Chapter 2	100
E Study System Parameters for Chapter 3	102
F Study System Parameters for Chapter 4	104
Bibliography	105
Curriculum Vitae	112

List of Figures

1.1	The structure of a typical PEV.	4
1.2	ac-dc converters for power system integration of electric vehicles.	5
1.3	A dc distribution system for power system integration of electric vehicles.	6
2.1	A dc distribution system for power integration of electric vehicles and PV modules.	15
2.2	Schematic diagram of the dc system.	16
2.3	Simplified block diagram of the controlled dc-voltage power port.	16
2.4	Block diagram of the current-control scheme of the VSC.	17
2.5	Control block diagram of dc-bus voltage controller.	18
2.6	General form of the dc-voltage controller.	20
2.7	The schematic diagram of i^{th} bidirectional dc-dc converter.	20
2.8	The simplified model of i^{th} bidirectional dc-dc converter.	21
2.9	Equivalent circuit of the dc system of Fig. 2.2.	22
2.10	Realistic battery model.	30
2.11	Response of a battery charger for two models for the battery: ideal voltage source and realistic battery model.	32
2.12	Response of the dc-system to a change in P_{dc2} from -10 kW to -20 kW when P_{dc1} is 50 kW and P_{dc3} to P_{dc6} are -20 kW.	33
2.13	Response of the dc-system to a change in P_{dc3} from 20 kW to 30 kW when P_{dc1} is 50 kW and P_{dc2} is -50 kW and P_{dc4} to P_{dc6} are -20 kW.	34
2.14	Eigenvalue migration plot as a function of the length of the interconnection cables.	34
2.15	Eigenvalue migration plot as a function of network-side capacitance.	35
2.16	Eigenvalue migration plot as a function of power consumption by dc-dc converter#2.	36
2.17	Response of the dc-system to a change in P_{dc2} from -60 kW to -80 kW when P_{dc1} is 10 kW, and P_{dc3} to P_{dc6} are -70 kW.	37

2.18	Equivalent circuit of the dc system with different nodes of coupling. . . .	38
3.1	A dc bus for distribution of power in a parking lot for PHEVs.	42
3.2	Schematic diagram of the dc system.	43
3.3	Simplified block diagram of the controlled dc-voltage power port.	43
3.4	Schematic diagram of the bidirectional dc-dc converter as a battery charger for i^{th} PHEV.	45
3.5	Simplified model of the dc-dc converter.	46
3.6	Equivalent circuit for the analysis of the dc system of Fig. 3.2.	46
3.7	Stable and unstable regions in the charging mode.	48
3.8	Modification of the power exchange setpoints of the dc-dc converters. . .	49
3.9	Simplified model of the modified dc-dc converter.	49
3.10	Connection block diagram for the proposed technique.	50
3.11	Boundaries between stable and unstable regions for unmodified and modified systems with different values of τ_i	52
3.12	Boundaries between stable and unstable regions for different values of power generation of PV modules.	53
3.13	The dc system response when the power flows from the ac power grid to the dc system.	54
3.14	The dc system response when the power flows from the dc system to the ac power grid.	54
3.15	Responses of the dc system in the first scenario; (a) the unmodified dc system (b) the modified dc system with $\tau_i = 0.1 ms$, (c) the modified dc system with $\tau_i = 0.2 ms$, (d) the modified dc system with $\tau_i = 2 ms$. . .	56
3.16	Responses of the dc system in the second scenario; (a) the unmodified dc system (b) the modified dc system with $\tau_i = 0.1 ms$, (c) the modified dc system with $\tau_i = 0.2 ms$, (d) the modified dc system with $\tau_i = 2 ms$. . .	57
3.17	Long-run simulations for v_{dc} ; the first unstable scenario for instability (top), the second unstable scenario for instability (bottom).	58
3.18	Proposed modification on a single constant-power element.	58
3.19	Proposed modification on a dc system with n dc-dc converters.	61
4.1	A dc distribution system (the dc system) for power system integration of electric vehicles.	68
4.2	Schematic diagram of the dc system.	70

4.3	Flowchart of the proposed energy management strategy.	73
4.4	Energy price and power demand in Toronto, on July 10, 2013 and July 11, 2013.	74
4.5	An example of determination of the energy exchange intervals for four PEVs with optimal energy exchange option.	76
4.6	An example of determination of the energy exchange intervals for three PEVs; The first PEV with the fast energy exchange option and the other two PEVs with the optimal energy exchange option.	77
4.7	Case I, Scenario 1: total load under uncoordinated charging of PEVs using 4-kW ac-dc battery chargers.	78
4.8	Case I, Scenario 2: total load if the PEVs are charged through the dc system without the supervision of the EMS.	79
4.9	Case I, Scenario 3: total load if the PEVs are charged through the dc system, under the supervision of the EMS, based on the optimal energy exchange option.	80
4.10	Case I, Scenario 4: total load if the PEVs are charged through the dc system, under the supervision of the EMS, based on the fast energy exchange option.	80
4.11	Case I, Scenario 5: total load if the PEVs are charged through the dc system, under the supervision of the EMS, based on a combination of both fast and optimal energy exchange options.	81
4.12	Case I: charging cost in different scenarios.	81
4.13	Total charging cost for different scenarios in Case I; (a) with degradation costs of 0.04\$/kWh (b) with degradation costs of 0.01\$/kWh.	82
4.14	Case II, Scenario 1: total load with batteries discharging if the owners all choose the optimal energy exchange option.	84
4.15	Case II, Scenario 2: total load with batteries discharging if the owners all choose the fast energy exchange option.	84
4.16	Case II, Scenario 3: total load with batteries discharging if 10% of the owners choose the fast energy exchange option.	85
4.17	Case II, Scenario 4: total load if 20% of the owners intend to charge their batteries, while the rest plan to discharge their batteries.	86
4.18	Case II: total discharging revenue in different scenarios.	86

4.19	Revenue and cost for different scenarios in Case II; (a) with degradation costs of 0.04\$/kWh (b) with degradation costs of 0.01\$/kWh.	87
5.1	Equivalent circuit of a dc system with mixed dc-dc converter and linear loads.	92
A.1	The schematic diagram of a full bridge bidirectional dc-dc converter with a voltage-droop mechanism.	94
A.2	Relation between P_{si}^* and v_i in a droop-based dc-dc converter.	94
A.3	The simplified model of the droop-based dc-dc converter of Fig. A.1. . .	95

List of Tables

1.1	Battery capacity and specifications of some electric vehicles on the market	3
1.2	Electric Vehicles Charging Levels	4
2.1	Parameters of a typical battery cell and battery module	32
4.1	Total charging cost for different scenarios in Case I	83
4.2	Net cost/revenue for different scenarios in Case II	88
D.1	Study dc System Parameters	101
D.2	Battery Chargers Parameters	101
E.1	Study dc System Parameters	102
E.2	Battery Chargers Parameters	103
F.1	Parameters of the Study System in Chapter 4	104

List of Appendices

Appendix A Modeling of a droop-based dc-dc converter in a dc system	93
Appendix B Positive-Definiteness of \mathbf{R} and \mathbf{L} matrices	96
Appendix C Proof of Equation (2.52)	98
Appendix D Study System Parameters for Chapter 2	100
Appendix E Study System Parameters for Chapter 3	102
Appendix F Study System Parameters for Chapter 4	104

Abbreviations and Symbols

ac	Alternating Current
dc	Direct Current
BEV	Battery Electric Vehicle
EMS	Energy Management Strategy
EV	Electric Vehicle
EVSE	Electric Vehicle Supply Equipment
HOEP	Hourly Ontario Energy Price
ICE	Internal Combustion Engine
MPPT	Maximum Power-Point Tracking
PCC	Point of Common Coupling
PEV	Plug-in Electric Vehicle
PFC	Power-Factor Correction
PHEV	Plug-in Hybrid Electric Vehicle
PI	Proportional-Integral
PLL	Phase-Locked Loop
PSCAD	Power System Computer-Aided Design
PV	Photo-Voltaic
PWM	Pulse-Width Modulation
SAE	Society of Automotive Engineers
TOU	Time-of-Use
SOC	State-of-Charge
VSC	Voltage-Sourced Converter

Nomenclature

P_s	Real power at PCC
Q_s	Reactive power at PCC
L_s	Linking inductance
R_s	Parasitic resistance of L_s (including on-state resistance of the VSC switches)
P_{dc}	Total power at dc terminal of the VSC
C	dc-side capacitance of the VSC
v_{dc}	dc bus voltage
P_{dci}	Power that flows to the network terminal of i^{th} dc-dc converter
v_i	Voltage of the network terminal of i^{th} dc-dc converter
R_i	Cable resistance of the dc network branches
L_i	Cable inductance of the dc network branches
V_s	Peak value of the ac grid line-to-neutral
ω	Power system frequency
V_{bati}	Voltage of i^{th} battery
P_{Bi}	Power of i^{th} battery
i_i	Current of the network-side terminal of i^{th} dc-dc converter
C_i	Capacitance of the network-side terminal of i^{th} dc-dc converter
P_{PV}	Power of PV modules
$P_{dc_{max}}$	Maximum permissible power that can be imported by the dc system
P_{rati}	Power rating of i^{th} battery charger
η_i	Efficiency of i^{th} battery charger
$\mu_{i,k}$	Duration of k^{th} energy exchange interval for i^{th} PEV
r_k	Energy price in k^{th} energy exchange interval
E_i	Exchangeable energy of i^{th} PEV
$SOC_{i,i}$	Initial value for State-of-Charge of i^{th} PEV
$SOC_{i,f}$	Final value for State-of-Charge of i^{th} PEV
T_{P_i}	Parking duration of i^{th} PEV
E_{cap_i}	Battery capacity of i^{th} PEV

Chapter 1

Introduction

1.1 Statement of Problem and Thesis Objectives

The power system integration of Plug-in Electric Vehicles (PEVs) and the possibility of bidirectional power exchange between them and the host grid have attracted attentions recently [1,2]. In addition to providing traction power, batteries in a PEV can potentially be used for bulk energy storage in such applications as peak shaving, reactive power compensation [3], and the integration of renewable energy resources. Public parking areas within hospitals, department stores, and residential and commercial premises are examples of locations where a large number of PEVs can be integrated with the power system. Thus, PEV owners can charge their batteries (or buy energy from the rest of the system) or discharge them (or sell energy to the rest of the system) based on their trip plans, cost of electricity, and the State of Charge (SOC) of the batteries; electric energy can be stored at night when the cost of electricity is low, and then sold at a higher price if there is a high demand for electricity or if the host grid is in need of ancillary services. This can be achieved through bidirectional power-electronic converters [4,5].

The increasing number of PEVs is, however, expected to adversely impact the power system [6]. Charging a large number of PEVs at the same time in the evening, when the owners come back home from work and connect their vehicles to the battery chargers, could significantly stress the power grid; causing voltage fluctuations, suboptimal generation dispatch, degraded system efficiency, and increasing the likelihood of blackouts due to network overloads [7]. Therefore, suitable infrastructure and smart charging strategies are required to circumvent or mitigate these potentially negative impacts.

This thesis concentrates on bidirectional power exchange between a large number of

plug-in electric vehicles and the ac power grid. Hereinafter, Plug-in Electric Vehicles (PEVs) and Plug-in Hybrid Electric Vehicles (PHEVs) will be used interchangeably to represent all electric vehicles.

The objectives of the thesis are:

- To introduce a dc distribution system for the integration of a large number of electric vehicles, including PEVs and PHEVs, into the ac power grid, in public parking areas.
- To develop a mathematical model for the dc distribution system to capture both the steady-state and dynamic characteristics of the system, to analyze the stability of the system, and to check for the existence of the steady-state operating point of the system.
- To develop a control strategy to mitigate the instability problem of the dc distribution system and expand the stable operation region of the system, without a need for changing system parameters or hardware.
- To develop an energy management strategy for the dc distribution system to enable an optimal energy exchange among the PEV battery chargers in the dc system and the ac power grid.

1.2 Background

1.2.1 Electric Vehicle

Electric vehicles can be generally categorized in three different groups:

- **Plug-in Electric Vehicle (PEV)**

In this category, the electric vehicles are only powered by the on-board battery and there are no internal combustion engines in the vehicles. The batteries can be charged from a power source outside of the electric vehicles, through a connector. In the literature, battery electric vehicles (BEVs) are also used to refer to these electric vehicles.

- **Plug-in Hybrid Electric Vehicle (PHEV)**

Electric vehicles in this category have both electric motors and internal combustion engines (ICEs). The batteries can be charged from a power source outside of the

Table 1.1: Battery capacity and specifications of some electric vehicles on the market

Model	Type	Battery Technology	Battery Capacity	All-Electric Range
Chevrolet Volt	PHEV	Li-Ion	17.1 kWh	61 km
Mitsubishi i-MiEV	PEV	Li-Ion	16 kWh	96 km
Ford Fusion SE Energi	PHEV	Li-Ion	7.6 kWh	30 km
Nissan Leaf	PEV	Li-Ion	24 kWh	159 km
Toyota Prius	PHEV	Li-Ion	4.4 kWh	22 km
Tesla Model S	PEV	Li-Ion	85 kWh	480 km

electric vehicles. Therefore, these electric vehicles can exchange power with the host power grid. PHEVs typically operate in a “blended” mode, using the ICE and electric motor together, to substantially reduce gasoline consumption when operating in battery charge depletion mode.

- **Hybrid Electric Vehicle (HEV)**

In this category, the vehicles have both electric motors and internal combustion engines. However, the batteries cannot be charged from a power source outside of the vehicle.

In this thesis, only the first two categories, i.e., PEV and PHEV, are considered for study, as the electric vehicles in the third category do not exchange power with the host power grid. Table 1.1 lists the type and battery capacity of some electric vehicles on the market [8–13].

1.2.2 Battery Chargers for Electric Vehicles

Battery chargers for electric vehicles have been classified in three different levels by the Society of Automotive Engineers (SAE). Table 1.2 summarizes the charging levels for PEVs based on SAE J-1772 standard [14, 15]. Level 1 is the slow charging level where the electric vehicles can be plugged in to a convenience ac power outlet and the maximum charging power level is 1.92 kW. At this level, the battery charger is usually inside the vehicle. For Level 2 charging, the maximum power is 19.2 kW and it uses 240 Vac power outlet. Level 3 offers commercially fast battery charging for electric vehicles and it typically operates with 480 V or higher three phase circuit, requiring an off-board charger.

Table 1.2: Electric Vehicles Charging Levels

Power Level Types	Charger Location	Typical Use	Energy Supply Interface	Expected Power Level	Charging Time	Vehicle Technology
Level 1 120 Vac (US) 230 Vac (EU)	On-board 1-phase	Charging at home or office	Convenience outlet	1.4kW (12A) 1.9kW (20A)	4-11 hours 11-36 hours	PHEVs (5-15kWh) EVs (16-50kWh)
Level 2 240 Vac (US) 400 Vac (EU)	On-board 1- or 3-phase	Charging at private or public outlets	Dedicated EVSE	4kW (17A) 8kW (32A) 19.2kW (80A)	1-4 hours 2-6 hours 2-3 hours	PHEVs (5-15kWh) EVs (16-30kWh) EVs (3-50kWh)
Level 3 208-600 Vac or Vdc	Off-board 3-phase	Commercial, analogous to a filling station	Dedicated EVSE	50kW 100kW	0.4-1 hour 0.2-0.5 hour	EVs (20-50kWh)

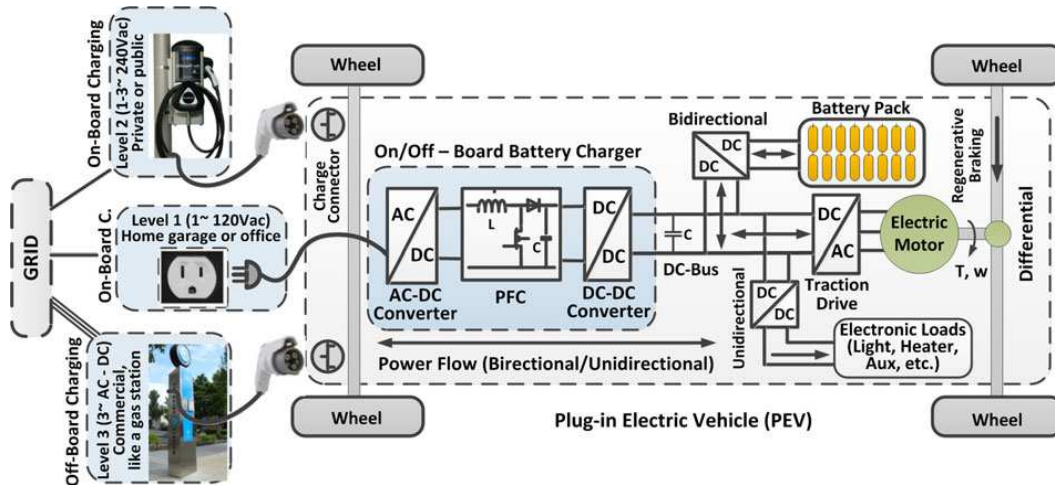


Figure 1.1: The structure of a typical PEV.

Fig. 1.1 shows the internal structure of a typical electric vehicle and the battery chargers at different levels [15]. The SAE J1772 standard prescribes that Level 1 and Level 2 battery chargers should be located on the electric vehicle. For Level 3, the standard considers off-board battery charger. In this case, the battery charger can be directly connected to the battery of the electric vehicle. This enables Level 3 battery chargers to perform fast charging in public places such as parking lots on commercial premises.

1.2.3 Power System Integration of Electric Vehicles

In most proposed strategies for power system integration of electric vehicles, ac-dc power-electronic converters act as the battery chargers and are directly interfaced with the power grid [15, 16], as is shown in Fig. 1.2. Alternatively, dc distribution networks embedding dc-dc converters (as the battery chargers) have been proposed for power system integration of electric vehicles in public parking areas, where a sizeable number

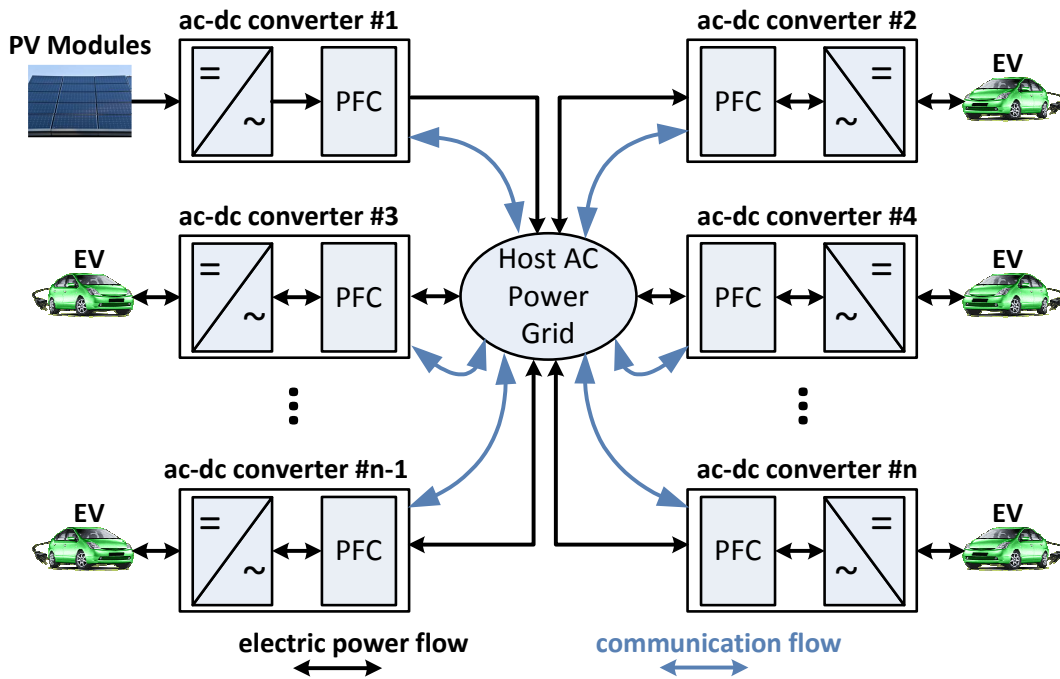


Figure 1.2: ac-dc converters for power system integration of electric vehicles.

of PEVs are interfaced with the power grid [17–20], as shown in Fig. 1.3.

Using a dc distribution system and dc-dc battery chargers has the following advantages over ac-dc battery chargers that are directly connected to the ac power grid:

- In the dc distribution system, power factor correction is sufficient to be done only at a central point where the whole system connects to the ac power grid and this reduces the cost of power factor correction modules for individual battery chargers [19, 20];
- Integration of renewable energy resources such as photo-voltaic (PV) modules will be easier in a dc infrastructure due to the omission of the intermediate dc-ac converters needed in grid-connected PV systems [17, 19, 21] ;
- A large number of PEV batteries can contribute more efficiently in providing ancillary services for the ac power grid than an individual PEV battery with a smaller energy capacity.
- The energy exchange can be done inside the dc distribution system, between PEVs themselves and also with the PV modules, without intervention of the ac power grid and this reduces the ac power grid load;

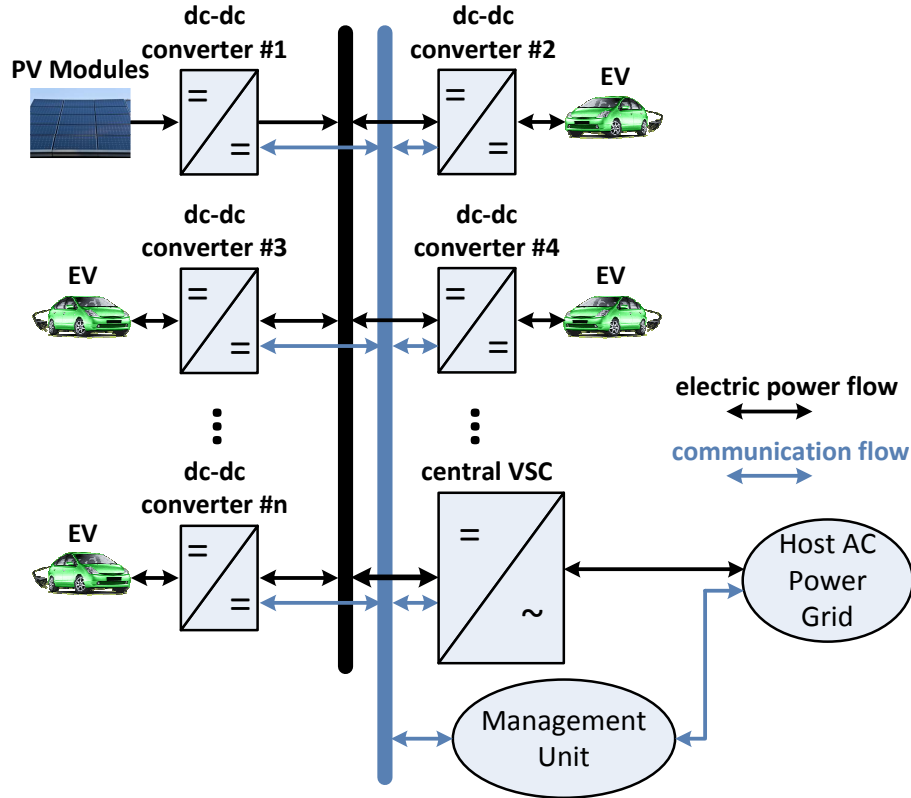


Figure 1.3: A dc distribution system for power system integration of electric vehicles.

- The host ac power grid needs to communicate only with one entity that is the intelligence of the management unit of the dc distribution system, rather than with multiple PEV battery chargers; the coordination between the PEVs is undertaken by the internal intelligence of the dc distribution system and its associated communications network. Thus, the power system operator can more quickly and efficiently invoke ancillary services.

The dc distribution systems can be installed in parking lots of commercial and residential areas, where a large number of electric vehicles can be connected to the system [22]. From the economic perspective, there are three parties that are financially interacting with each others in this system:

1. the PEV owners;
2. the parking lot operator; and
3. the ac power grid operator.

In a dc distribution system, the PEV owners can use the wholesale energy price to charge their vehicles. The wholesale energy price is usually much cheaper than the retail energy price, even considering the administration fee from the parking lot operator, and therefore, the PEV owners will financially gain when they use the dc distribution system to connect their vehicles to the ac power grid. Moreover, by using a smart charging strategy, the charging activities can be shifted to the time frames when the energy price is even cheaper, hence further reduce the cost of the battery charging.

The parking lot operator can make revenue by:

- charging the PEV owners an administration fee for charging or discharging energy (per kWh) [23, 24]; and
- charging the ac power grid for providing the ancillary services.

The ac power grid benefits from the dc system by using the ancillary services which are provided. Using the battery capacity of a large number of PEVs, the dc distribution system has the capacity to provide a variety of services to the ac power grid such as peak shaving, load shaping, frequency regulation, ac voltage support, and power regulation service [25]. By using peak shaving service, for example, the ac power grid avoids the installation of capacity only to supply the peaks of a highly variable loads. To provide this service, the dc distribution system supply energy to the high-demand customers of the ac power grid at the peak-time.

One of the problems with dc distribution systems is the possibility of instability in the system. Due to the constant-power property of dc-dc converters, the dc system becomes unstable if the powers absorbed by the converters exceed certain values [20]. This phenomenon inflicts a limit on the maximum power that can be imported to charge the batteries and, consequently, precludes full utilization of the installed capacities and prolongs the charging times. Therefore, it is imperative to devise a stability enhancement technique in order to push the limits and expand the stable operating region of the dc distribution system.

1.3 Thesis Contributions

The main contributions of this thesis can be listed as follows:

- The thesis proposes a dc distribution system for power system integration of plug-in electric vehicles. The proposed system is expected to be more efficient and

economical than an equivalent aggregate of ac-dc battery charges connected to the ac grid, since it relieves the battery chargers from the need for a bidirectional, front-end, power-factor correction (PFC) stage. Further, due to its DC nature, the proposed system is amenable to integration of Photovoltaic (PV) modules. The thesis also proposes a systematic method for developing a model of a dc distribution system, based on the configuration of the system. The developed model is of the matrix form and, therefore, can readily be expanded to represent a system of any desired number of dc-dc converters. The model captures both the steady-state and dynamic characteristics of the system, and includes port capacitors of the converters and the interconnection cables. Thus, it can be used for identifying the condition for existence of a steady state, as well as for stability analysis.

- The thesis further proposes a method for enhancing the stability of a dc distribution system that integrates plug-in electric vehicles with the ac power grid. Using a nonlinear control strategy, the proposed stability enhancement method mitigates the issue of instability by altering the power setpoints of the battery chargers, bidirectional dc-dc converters, without a need for changing system parameters or hardware. The thesis further presents mathematical models for the original and modified systems and demonstrates that the proposed technique expands the stable operating region of the dc distribution system.
- Finally, the thesis proposes an energy management strategy (EMS) for the dc distribution system for power system integration of plug-in electric vehicles (PEVs). Using an on-line constrained optimization algorithm, the proposed EMS manages the power flow within the dc system. Thus, the PEV owners can charge or discharge their batteries, based on the state-of-charge (SOC) of the batteries and their upcoming trip plans. The EMS offers two energy exchange options to the PEV owners: (i) The fast energy exchange option for the owners wishing to minimize the energy exchange time and (ii) The optimal energy exchange option for the owners intend to either minimize their costs of charging or maximize their revenues through selling their stored energy. The proposed EMS seamlessly handles all charging/discharging requests from the PEV owners with different options and, at the same time, it takes into account the power demand and power generation limits of the ac grid, to preclude under-voltage, over-voltage, and reverse power flow issues.

1.4 Literature Survey Pertinent to Thesis Contributions

Chapter 2 of this thesis focuses on the mathematical model for the dc distribution system. A dc distribution system is expected to offer a higher efficiency and to enable an easier integration of renewable energy sources such as photovoltaic (PV) and fuel-cell systems [26, 27], as compared with a system of ac-dc battery chargers. However, it is prone to instabilities due to constant-power property of the hosted dc-dc converters, if powers drawn by the dc-dc converters (to charge the batteries) exceed certain limits [20, 28, 29]. Thus, one needs a model of the system to characterize the steady-state and dynamic behaviors of the system. Such a model should be tractable, while adequately accurate, and it should also represent both the steady-state and dynamic characteristics of the system. One should also be able to systematically expand it to represent a system of any desired, and most likely large, number of dc-dc converters. To the author's best of knowledge, the published technical literature does not present a model with the aforementioned features.

Several prior studies have reported system-level models for dc distribution systems [30–33]. The main issue associated with the aforementioned studies is that they consider a limited number of dc-dc converters on the dc distribution system and develop the model for the system based on that assumption. Reference [30], proposes a model for a dc distribution system, but the model only describes the steady-state behavior of the system. Reference [31] develops a model, and proposes a method for stabilizing a dc distribution system. However, the presented model is limited to three converters and, consequently, cannot be adopted for a dc distribution system with a large number of converters. In [27] a model is proposed for a dc distribution system with multiple loads and sources, but it does not consider the interconnection cables of the system. Reference [34] proposes a reduced-order model for a generic dc microgrid. The presented model, however, does not account for the terminal capacitors of the dc-dc converters; the interconnection cables and the terminal capacitors both play important roles in the steady-state and dynamic behaviors of a dc distribution system and, therefore, cannot be ignored. To address the foregoing shortcomings, this thesis proposes a systematic approach to develop a mathematical model for a dc distribution system. The proposed mathematical model is of the matrix form and can be used to analyze small-signal dynamic behavior of the dc distribution system with an arbitrarily large number of dc-dc converters. The thesis also derives a set of computationally efficient equations for calculating the dc distribution

system eigenvalues to facilitate online stability assessment of the system on an embedded signal-processing platform.

Chapter 3 of this thesis concentrates on mitigating the instability issue of the dc distribution system. Due to the constant-power property of dc-dc converters [28,35], the dc distribution systems, that include dc-dc converters, become unstable if the powers absorbed by the converters exceed certain values [20]. This phenomenon inflicts a limit on the maximum power that can be imported to charge the batteries and, consequently, precludes full utilization of the installed capacities and prolongs the charging times. Therefore, it is imperative to systematically characterize the phenomenon and identify the prevailing constraints, and devise a stability enhancement technique, in order to push the limits and expand the stable operating region of the dc system.

To mitigate the aforementioned issue of instabilities caused by constant-power elements in a dc distribution system, various methods have been proposed in the literature, [31, 36–41]. The method proposed in [36] stabilizes a dc-link electric propulsion system where a dc-ac converter drives an induction motor, by altering the torque set-point of the motor. The proposed technique, therefore, is applied to a dc system with one constant-power element; there is no analysis for multiple constant-power elements. In reference [37], a method has been proposed to increase the stability margin of a dc system with two constant-power elements, and therefore, the method cannot be applied to a dc distribution system with multiple dc-dc converters. The stabilizing methods that have been proposed in [31, 38, 39] are also suitable for the dc systems with a limited number of constant-power elements. The techniques proposed in [40] and [41] deal with a system in which a dc-dc converter is assumed to be supplying another constant-power element. However, both techniques require information about the internal state variables and access to the PWM signal of the dc-dc converter. Moreover, the studied systems include only one dc-dc converter and one constant-load element. To address the foregoing shortcomings, this thesis proposes a stability enhancement technique to improve the dynamic behavior, and expand the stable operating region of the dc distribution system. The proposed technique is easy to implement and does not need any information internal to the dc-dc converters of the system. Therefore, the technique can be used for off-the-shelf dc-dc converters which is financially beneficial.

Chapter 4 of the thesis deals with the energy management strategy (EMS) for the dc distribution system. The EMS controls the power flow among the battery chargers and the ac power grid. The increasing number of PEVs is expected to adversely impact the

power system and, therefore, suitable infrastructure and smart charging strategies are required to circumvent or mitigate those impacts [6, 42].

Several recent reported studies have proposed charging strategies for PEVs [7, 24, 43–49]. Reference [24] proposes algorithms for optimizing the PEV charging schedule from the owner’s perspective. A real-time smart load management control strategy is proposed in [7] to coordinate the charging of PEV, to minimize the power loss and the charging cost, and to mitigate the voltage fluctuations at the host ac grid. A strategy is proposed in [43] to mitigate the adverse impacts that uncontrolled charging of the PEVs impose on the host power system. Using empirical driving profiles, reference [44] shows the economic benefits of a smart charging strategy against a uncontrolled charging strategy for charging the PEVs. In [45], it is assumed that there is a limited future knowledge of the mobility of the PEVs and it is shown that by using this information, the negative impacts of the PEV charging can be reduced. Reference [46] proposes charging control strategies for a battery swapping station, where the PEV owners can quickly swap their depleted batteries with previously charged batteries. In [47], optimal scheduling has been proposed for both charging and discharging of the PEVs. The references cited above do not necessarily concern dc systems. However, they all assume an integral entity, an aggregator, that negotiates with the PEVs, in one hand, and with the host power system in the other hand. Hence, the host ac grid deals with only one entity, the aggregator, rather than a large number of PEVs.

In the majority of the reported studies, the proposed strategies aim to only optimize the charging costs for the PEV owners, or minimize the power loss within the system, but do not offer to the owners an option for fast battery charging (by which the charging time is minimized rather than the charging cost). Further, the reported studies commonly assume that the PEV owners fully comply with the (proposed) charging strategies, i.e., they connect their vehicles to the chargers, for the entire specified period, and do not depart early. In practice, however, an owner may decide to leave before the planned period has elapsed. Most of the reported studies also assume a unidirectional power flow, that is, into the PEVs, whereas there is a possibility for bidirectional power exchange among the PEVs and the host ac grid. To address the foregoing shortcomings, this thesis proposes an energy management strategy that offers both fast and optimized energy exchange options to the PEV owners. The proposed strategy limits the power consumption and power generation of the dc distribution system to prevent the negative impacts of simultaneous charging or discharging of a large number of electric vehicles on the ac power grid. The

proposed strategy seamlessly handles requests for charging or discharging of the electric vehicles and also takes into account the likelihood of early departure of the PEV owners.

Chapter 2

Modeling of the DC Distribution System

2.1 Introduction

A dc distribution system is expected to offer a higher efficiency and to enable an easier integration of renewable energy sources such as photovoltaic (PV) and fuel-cell systems [20, 26, 27], as compared with a system of ac-dc battery chargers. However, it is prone to instabilities due to constant-power property of the hosted dc-dc converters, if powers drawn by the dc-dc converters (to charge the batteries) exceed certain limits [20, 28, 29, 35]. Thus, one needs a model of the system to characterize the steady-state and dynamic behaviors of the system. Such a model should be tractable, while adequately accurate, and it should also represent both the steady-state and dynamic characteristics of the system. One should also be able to systematically expand it to represent a system of any desired, and most likely large, number of dc-dc converters.

This chapter proposes a systematic method for developing a model of a dc distribution system, based on the configuration of the system. The developed model is of the matrix form and, therefore, can readily be expanded to represent a system of any desired number of dc-dc converters. The model captures both the steady-state and dynamic characteristics of the system, and includes port capacitors of the converters and the interconnection cables. Thus, it can be used for identifying the condition for existence of a steady state, as well as for stability analysis. This chapter further proposes an alternative set of characteristic equations that are less computationally intensive than the original matrix representation, for example, for on-line stability assessment tasks. The

adequacy of the proposed model has been demonstrated through a number of case studies conducted and compared in PSCAD/EMTDC [50] and MATLAB software environments.

2.2 System Configuration and Components

Fig. 2.1 illustrates a conceptual diagram of a dc distribution system for the integration of electric vehicles and PV modules with a host ac power grid. The dc distribution system consists of a network of interconnection cables, a central voltage-sourced converter (VSC), a management unit, and a multitude of dc-dc converters acting as battery chargers that interface the EVs with the dc distribution system. Similarly, the PV modules are interfaced with the dc distribution system via corresponding dc-dc converters. It should be noted that in this thesis, the PV modules are considered as an auxiliary source of energy due to the limitation of their energy capacity and therefore, the main source of energy for charging the electric vehicles is the ac power grid. The network interconnects the dc port of the central VSC and network-side ports of the dc-dc converters, in a so-called *bus configuration*. In the widely used bus configuration, each converter, including the central VSC, is connected to a node common to all of the converter, through a corresponding interconnection cable, while there is no other connection between any two converters [26], [51, 52]. Therefore, all the electrical power exchange inside the dc distribution system is done via the common node.

From its ac side, the central VSC is interfaced with the host ac grid, operated as a controlled dc-voltage power port [53], and regulates the dc voltage of the network. Thus, the central VSC enables a bidirectional exchange of energy between the dc distribution system and the ac grid. It is assumed that the operation is supervised by a management unit, which determines power limits for the battery chargers, and communicates them via a communication network [54]. The communication network also collects metering information, for the management unit, from the central VSC and the dc-dc converters.

Fig. 2.2 shows a schematic diagram of the dc distribution system of Fig. 2.1. As the diagram indicates, the central VSC is interfaced with the host ac power grid via a three-phase tie reactor, L_s ; the resistance R_s represents the aggregate effect of the on-state power loss of the switches of the VSC and ohmic power loss of the tie reactor. Each distribution wire/cable is represented by a corresponding series $R - L$ branch. The power leaving the network-side port of a dc-dc converter is denoted by P_{dc} , which can be positive or negative for a battery charger, and only positive for a converter that interfaces

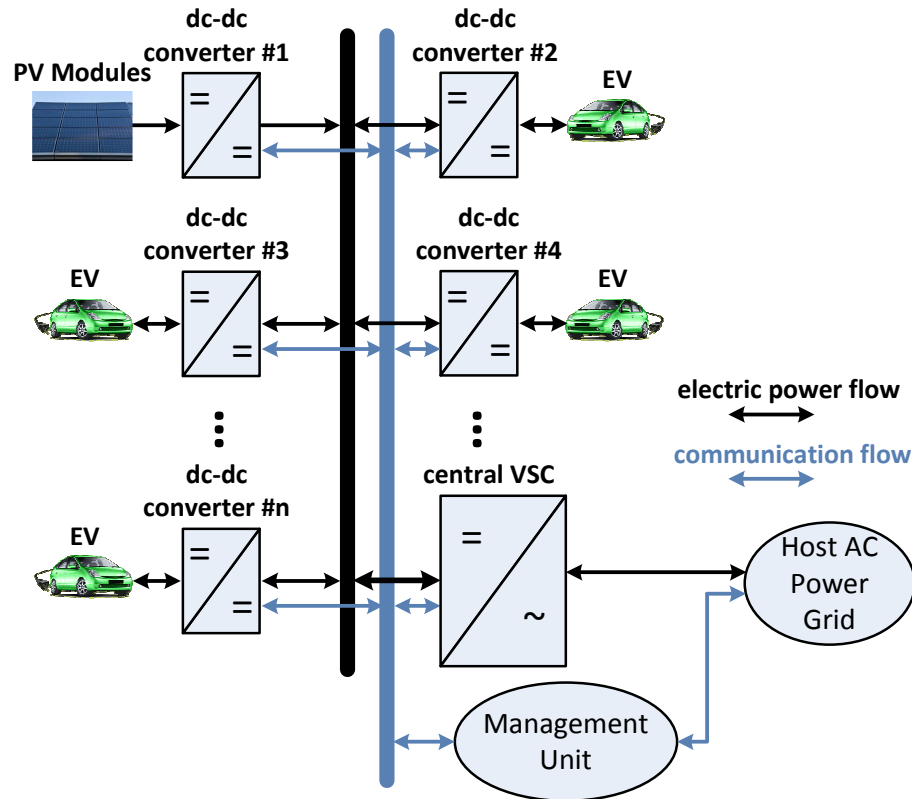


Figure 2.1: A dc distribution system for power integration of electric vehicles and PV modules.

PV modules.

2.2.1 Central VSC

The central VSC and its control scheme act as a controlled dc-voltage power port and regulate the dc voltage of the network (Fig. 2.3 illustrates the concept). The VSC is current-controlled, such that its output real power, P_s , rapidly tracks the real-power setpoint, P_s^* , issued by a dc-voltage regulation loop. P_{dc} denotes the power that the rest of the dc system delivers to the VSC. As Fig. 2.3 indicates, a measure of P_{dc} is incorporated in the control loop, as a feed-forward signal, to mitigate the dynamic coupling between the dc-voltage regulation loop and the rest of the dc system.

Current-Controlled Scheme

The function of the current-control scheme is to regulate the ac-side current of the VSC, by means of the pulse-width modulation (PWM) switching strategy. Fig. 2.4 illustrates a block diagram of the current-control scheme. As Fig. 2.4 indicates, the control is

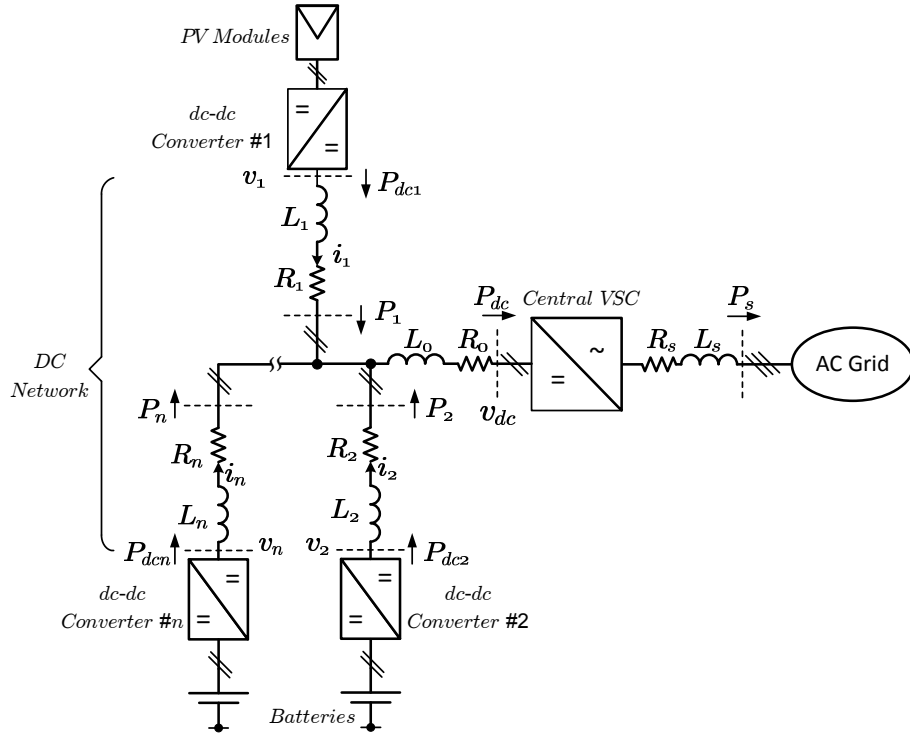


Figure 2.2: Schematic diagram of the dc system.

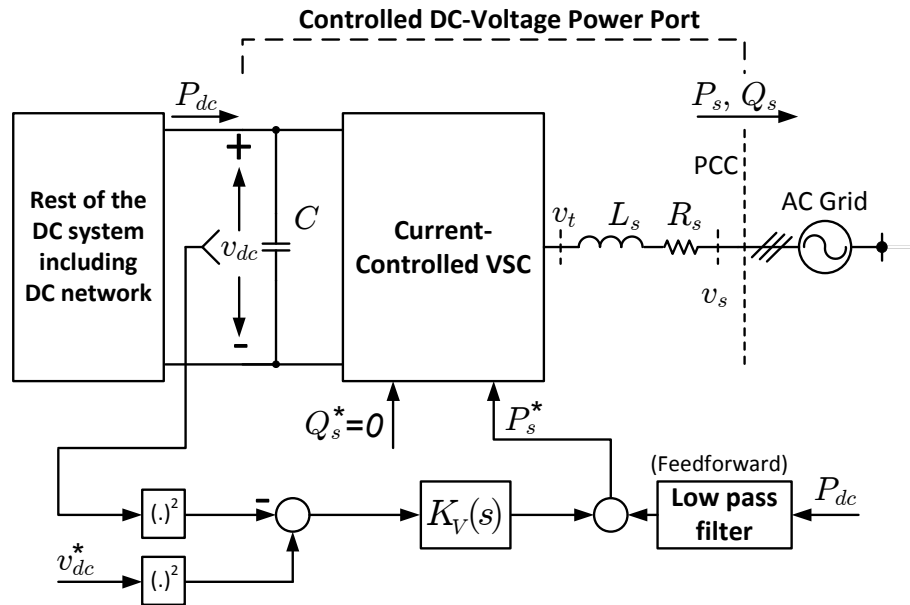


Figure 2.3: Simplified block diagram of the controlled dc-voltage power port.

performed in a dq reference frame whose d -axis makes angle ρ against the horizontal axis of the stationary frame [53]. The angle ρ is determined by a PLL (not shown here) which also calculates ω , i.e., the frequency of the ac-side terminal of the VSC. The setpoints of

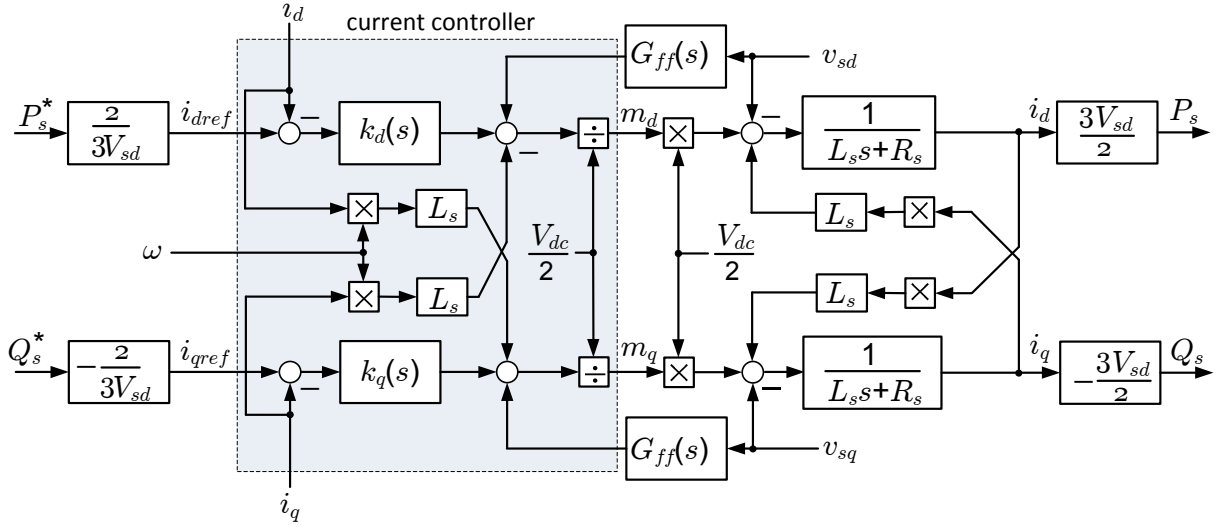


Figure 2.4: Block diagram of the current-control scheme of the VSC.

i_{dref} and i_{qref} are determined based on the power setpoints of P_s^* and Q_s^* , respectively; in this thesis, Q_s^* is set to zero as there is no reactive power exchange between the VSC and the ac power grid. The samples of i_d and i_q are first compared to their respective setpoints and the error signals are processed by two corresponding compensators, $K_d(s)$ and $K_q(s)$. The compensators outputs are then augmented with feed-forward and decoupling signals (to mitigate the impact of the ac-side voltage variations on the regulation of i_d and i_q), and the resulting signals are normalized to the VSC gain, $\frac{V_{dc}}{2}$, and produce m_d and m_q for the PWM gating pulse generator.

If the compensators are chosen as

$$k_d(s) = k_q(s) = \frac{L_s}{\tau_c} + \frac{R_s}{\tau_c s} \quad (2.1)$$

then the closed-loop transfer functions of P_s^* to P_s , and Q_s^* to Q_s become equivalent to two first-order transfer functions as

$$G_p(s) = \frac{P_s(s)}{P_s^*(s)} = \frac{Q_s(s)}{Q_s^*(s)} = \frac{1}{\tau_c s + 1}, \quad (2.2)$$

where time constant τ_c is a design choice [53]. In fact, the combination of the feed-forward blocks in Fig. 2.4 and the compensators of equation (2.1) provides a pole-zero cancellation to simplify the transfer function of the closed-loop system. This is a stable pole-zero cancellation and therefore, an imperfect cancellation does not have any effect on the stability of the system. Also, if the location of the poles and zeroes are close to each

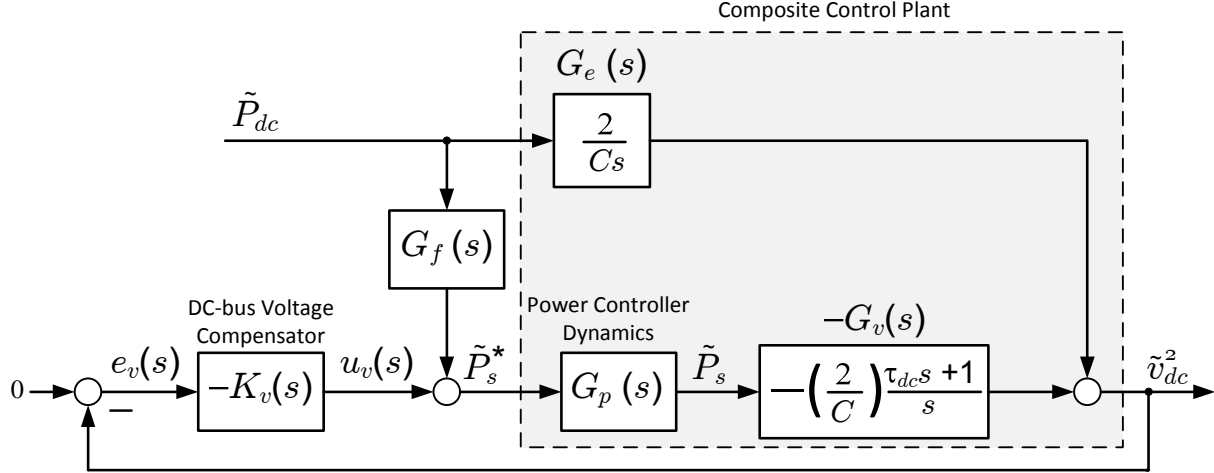


Figure 2.5: Control block diagram of dc-bus voltage controller.

other, the imperfect stable pole-zero cancellation creates a very short trace in the root-locus diagram of the system that have little impact on the behavior of the closed-loop system.

Controlled dc-Voltage Power Port

As discussed in [53], dynamics of \tilde{v}_{dc}^2 in Fig. 2.3 can be described by

$$\frac{d\tilde{v}_{dc}^2}{dt} = \frac{2}{C}\tilde{P}_{dc} - \frac{2}{C}\left[\tilde{P}_s + \left(\frac{2L_s P_{dc0}}{3V_s^2}\right)\frac{d\tilde{P}_s}{dt}\right], \quad (2.3)$$

where “ \sim ” denotes small-signal perturbation of a variable, V_s denotes the peak value of the grid line-to-neutral voltage and P_{dc0} is the steady-state value of P_{dc} .

Based on (2.3), Fig. 2.5 shows a simplified block diagram of the dc-bus voltage controller for the dc-voltage power port of Fig. 2.3. It is noted that $G_p(s)$ is defined in (2.2), and the transfer function from \tilde{P}_s to \tilde{v}_{dc}^2 is

$$\frac{\tilde{v}_{dc}^2(s)}{\tilde{P}_s(s)} = -\left(\frac{2}{C}\right)\frac{\tau_{dc}s+1}{s} = -G_v(s), \quad (2.4)$$

where τ_{dc} is a function of P_{dc0} :

$$\tau_{dc} = \frac{2L_s P_{dc0}}{3V_s^2}. \quad (2.5)$$

The value of τ_{dc} is negative (corresponding to a non-minimum phase plant) if the power flows from the ac grid towards the dc system. i.e., if P_{dc0} is negative. In Fig. 2.5, $K_v(s)$

is multiplied by -1 to compensate for the negative sign of $G_v(s)$.

Fig. 2.5 also indicates that a measure of \tilde{P}_{dc} is incorporated in the control process through a feed-forward filter, $G_f(s)$, to weaken the dynamic linkage between the the dc-voltage control loop and the rest of the dc system. The transfer function from \tilde{P}_{dc} , which is considered as a disturbance, to \tilde{v}_{dc}^2 is

$$\frac{\tilde{v}_{dc}^2(s)}{\tilde{P}_{dc}} = \frac{G_e(s) - G_f(s)G_p(s)G_v(s)}{1 + K_v(s)G_p(s)G_v(s)}. \quad (2.6)$$

To have a *perfect* cancelation of the dynamic linkage between the the dc-voltage control loop and the rest of the dc system, one should choose $G_f(s)$ as

$$G_f(s) = \frac{G_e(s)}{G_p(s)G_v(s)} = \frac{1}{G_p(s)(\tau_{dc}s + 1)}. \quad (2.7)$$

However, as mentioned in this section, the value of τ_{dc} will be negative if the power flows from the ac grid towards the dc system, which in turn, leads to a right-half pole (RHP) for the transfer function (2.7), and the system will lose the internal stability. In [53], $G_f(s)$ was chosen as an unity. Thus, to have a good disturbance rejection performance, i.e., to minimize the dynamic coupling between \tilde{P}_{dc} and \tilde{v}_{dc}^2 , one needs an adequately large controller gain for $K_v(s)$ [55].

Fig. 2.6 shows the general form of the dc-voltage controller, $K_v(s)$, which can be written as

$$K_v(s) = \frac{k_0}{s}H_1(s)H_2(s) \quad (2.8)$$

where $H_1(s)$, and $H_2(s)$ are lead filters to increase phase margin of the closed-loop system. The reason for using two lead filters is that by increasing the controller gain, k_0 , to have a better disturbance rejection performance, the required phase shift to ensure the stable operation of the system also will be increased. Each lead filter, as described in [53], can provide a maximum of 90° of phase shift. Therefore, for a total phase shift of more than 90° , two lead filters will be needed.

2.2.2 dc-dc Converters

Fig. 2.7 shows a simplified schematic diagram of a full-bridge dc-dc converter which, with no loss of generality, is assumed to represent a battery charger. The battery current, i_{Bi} , is regulated at its setpoint, i_{Bi}^* , by a feedback control loop in which a compensator, $K_i(s)$, processes the error $(i_{Bi}^* - i_{Bi})$ and generates the control signal u_i . A measure of

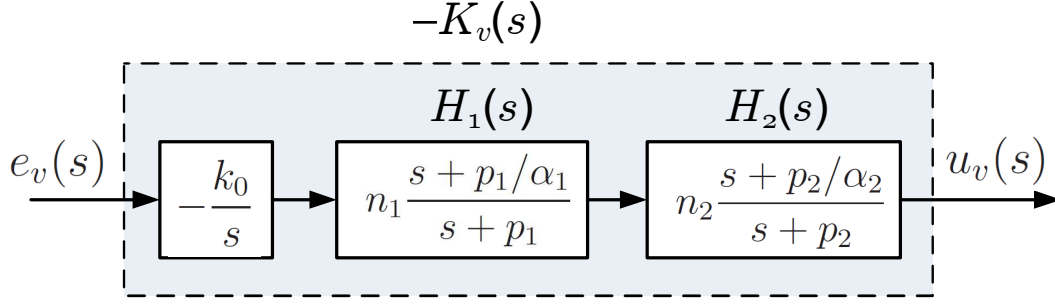
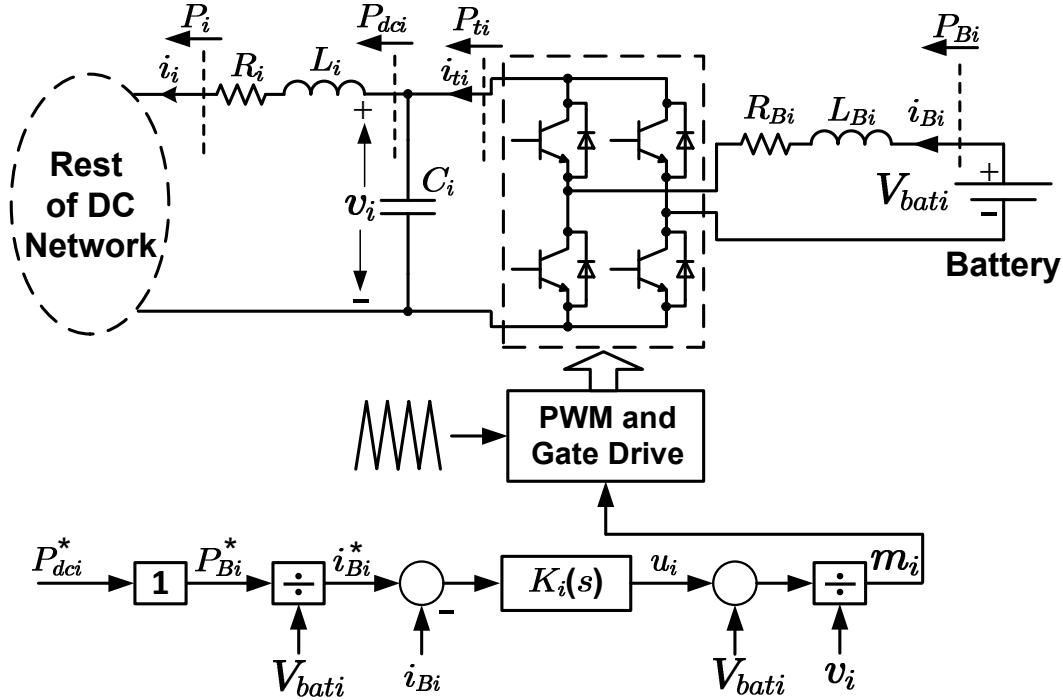


Figure 2.6: General form of the dc-voltage controller.

Figure 2.7: The schematic diagram of i^{th} bidirectional dc-dc converter.

the battery voltage, V_{bati} , is then added to u_i , and the resulting signal is divided by a measure of the network-side port voltage of the converter, v_i , to generate the pulse-width modulating (PWM) signal of the converter. In turn, i_{Bi}^* is calculated by dividing the battery power setpoint, P_{Bi}^* , by V_{bati} .

Assuming a fast and accurate current-control loop, the battery power P_{Bi} equals P_{Bi}^* . On the other hand, P_{Bi} is almost equal to the power that leaves the network-side port of the converter, P_{ti} ; the approximation is plausible in view of the typically small battery-side filter resistance R_{Bi} and inductance L_{Bi} (due to the typically large switching frequency of the converter), as well as negligible power losses of the converter. Therefore, $P_{ti} \simeq P_{Bi}^*$. Then, in a steady state, the network-side port capacitor C_i is effectively open

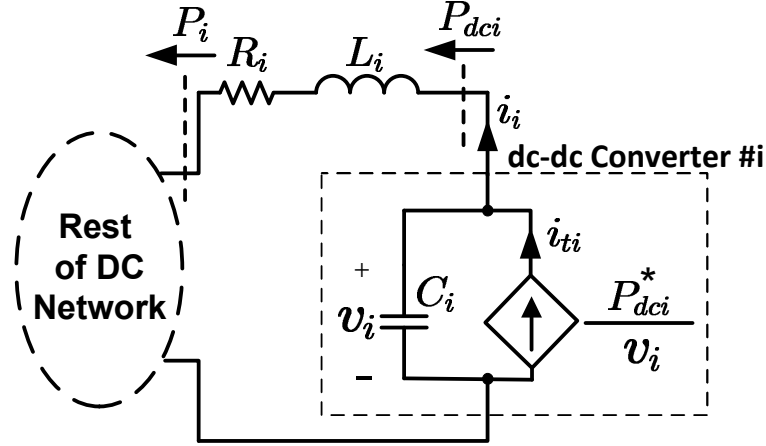


Figure 2.8: The simplified model of i^{th} bidirectional dc-dc converter.

and the power that the battery charger delivers to the rest of the dc system, P_{dci} , is equals P_{ti} and, therefore, P_{Bi}^* .

Hence, P_{Bi}^* should be determined based on value of power one desires the battery charger to deliver to the rest of the dc system, i.e, the setpoint P_{dci} , Fig. 2.7. The desirable fast current control can be ensured by proper design of $K_i(s)$. A proportional-integral (PI) compensator in generic form of

$$K_i(s) = k_{pi} + \frac{k_{ii}}{s} \quad (2.9)$$

guarantees that i_{Bi} tracks i_{Bi}^* , with zero steady-state error. Choosing $k_{ii}/k_{pi} = R_{Bi}/L_{Bi}$ and $K_{pi}/L_{Bi} = 1/\tau_{Bi}$, one obtains the first-order closed-loop transfer function of the form

$$\frac{I_{Bi}(s)}{I_{Bi}^*(s)} = \frac{1}{\tau_{Bi}s + 1}, \quad (2.10)$$

for which the time constant τ_{Bi} is a design choice.

2.3 Mathematical Model

Fig. 2.9 shows the equivalent circuit of the dc system of Fig. 2.2. In the circuit of Fig. 2.9, the central VSC is represented by a constant dc voltage source, and, as detailed in Section 2.2.2, each dc-dc converter is represented by a dependent current source in parallel with a capacitor, as depicted in Fig. 2.8. The capacitor, in turn, represents the network-side terminal capacitor of a typical dc-dc power converter, (see Fig. 2.7). The current source, however, is a representation of the fact that, in a power-electronic

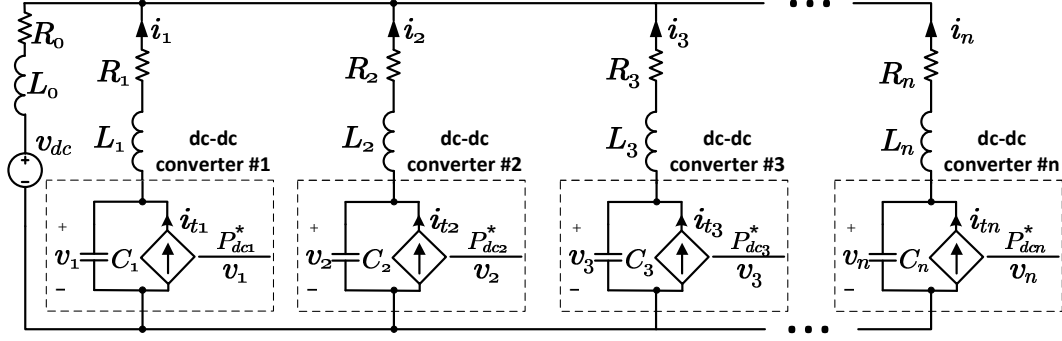


Figure 2.9: Equivalent circuit of the dc system of Fig. 2.2.

converter with regulated output (battery current, PV array voltage, etc.), the network-side port power does not depend on the network-side port voltage. Thus, the value of the current for the i^{th} , ($i = 1, 2, \dots, n$), converter is

$$i_{ti} = \frac{1}{v_i} P_{dci}^* \quad (2.11)$$

where P_{dci}^* and v_i are the power setpoint and network-side terminal voltage of the converter, respectively. For a converter serving as a battery charger, P_{dci}^* is the setpoint for the power delivered by (i.e., discharging) the battery; a negative value for P_{dci}^* , thus, corresponds to a charging power. For a converter interfacing PV modules, P_{dci}^* can only be positive and is determined by a so-called maximum power-point tracking (MPPT) algorithm, to equal the maximum power that the PV modules can deliver at the prevailing sunlight and temperature conditions. Thus, the assumption is that the control of the dc-dc converter is fast and, therefore, the power exchanged with the battery, or that delivered by the PV modules, equals P_{dci}^* . For a dc-dc converter with a voltage-droop mechanism, the modeling process has been presented in In Appendix A.

Let us regard the dc bus of the system of Fig. 2.9 as a node, i.e., the per-unit-length inductance and resistance of the bus are ignored (the model without this assumption is presented in Section 2.5). Thus, the following family of differential equations describe dynamics of the dc system of Fig. 2.9:

$$-v_i + R_i i_i + L_i \frac{di_i}{dt} + L_0 \sum_{k=1}^n \frac{di_k}{dt} + R_0 \sum_{k=1}^n i_k + v_{dc} = 0, \quad (2.12)$$

$$C_i \frac{dv_i}{dt} = \frac{P_{dci}^*}{v_i} - i_i, \quad (2.13)$$

where $i = 1, 2, \dots, n$.

Rewriting (2.12) in the matrix form, one finds

$$-\mathbf{v} + \mathbf{R}_b \mathbf{i} + \mathbf{L}_b \frac{d\mathbf{i}}{dt} + \mathbf{L}_0 \frac{d\mathbf{i}}{dt} + \mathbf{R}_0 \mathbf{i} + \mathbf{v}_{dc} = \mathbf{0} \quad (2.14)$$

where

$$\mathbf{v} = \begin{bmatrix} v_1 \\ v_2 \\ \vdots \\ v_n \end{bmatrix}, \quad \mathbf{i} = \begin{bmatrix} i_1 \\ i_2 \\ \vdots \\ i_n \end{bmatrix}, \quad \mathbf{v}_{dc} = v_{dc} \begin{bmatrix} 1 \\ 1 \\ \vdots \\ 1 \end{bmatrix}_{n \times 1}, \quad (2.15)$$

and

$$\mathbf{L}_b = \begin{bmatrix} L_1 & 0 & \cdots & 0 \\ 0 & L_2 & \cdots & 0 \\ \vdots & \vdots & \ddots & \vdots \\ 0 & 0 & \cdots & L_n \end{bmatrix}, \quad \mathbf{R}_b = \begin{bmatrix} R_1 & 0 & \cdots & 0 \\ 0 & R_2 & \cdots & 0 \\ \vdots & \vdots & \ddots & \vdots \\ 0 & 0 & \cdots & R_n \end{bmatrix}, \quad (2.16)$$

$$\mathbf{L}_0 = \begin{bmatrix} L_0 & L_0 & \cdots & L_0 \\ L_0 & L_0 & \cdots & L_0 \\ \vdots & \vdots & \ddots & \vdots \\ L_0 & L_0 & \cdots & L_0 \end{bmatrix}_{n \times n}, \quad \mathbf{R}_0 = \begin{bmatrix} R_0 & R_0 & \cdots & R_0 \\ R_0 & R_0 & \cdots & R_0 \\ \vdots & \vdots & \ddots & \vdots \\ R_0 & R_0 & \cdots & R_0 \end{bmatrix}_{n \times n}. \quad (2.17)$$

2.3.1 Existence of a steady state

With the derivatives set to zero for the steady state, the equation set (2.14) assumes the form

$$\mathbf{V} = \mathbf{R}\mathbf{I} + \mathbf{V}_{dc} \quad (2.18)$$

where

$$\mathbf{V} = \begin{bmatrix} V_1 \\ V_2 \\ \vdots \\ V_n \end{bmatrix}, \quad \mathbf{I} = \begin{bmatrix} I_1 \\ I_2 \\ \vdots \\ I_n \end{bmatrix}, \quad \mathbf{V}_{dc} = V_{dc} \begin{bmatrix} 1 \\ 1 \\ \vdots \\ 1 \end{bmatrix}_{n \times 1}, \quad \mathbf{R} = \mathbf{R}_0 + \mathbf{R}_b, \quad (2.19)$$

with the upper-case symbols denoting the steady-state values of variables.

Pre-multiplication of (2.18) by \mathbf{I}^T , the transpose of \mathbf{I} , yields

$$\mathbf{I}^T \mathbf{V} = \mathbf{I}^T \mathbf{R} \mathbf{I} + \mathbf{I}^T \mathbf{V}_{\text{dc}} \quad (2.20)$$

and

$$\begin{aligned} P_T &= \mathbf{I}^T \mathbf{V} \\ &= \sum_{i=1}^n V_i I_i \\ &= \sum_{i=1}^n P_{dci}^* \\ &= \mathbf{I}^T \mathbf{R} \mathbf{I} + \mathbf{I}^T \mathbf{V}_{\text{dc}}, \end{aligned} \quad (2.21)$$

where P_T is the sum of the powers leaving the network-side ports of all dc-dc converters.

Equation (2.21) describes the steady-state power flow in the dc system. The term $\mathbf{I}^T \mathbf{R} \mathbf{I}$ is the total power dissipated in the network cables, and $\mathbf{I}^T \mathbf{V}_{\text{dc}}$ is the power that enters the dc port of the central VSC and flows to the ac grid. The extreme value of P_T can be found by setting the derivative of (2.21) with respect to \mathbf{I} to zero:

$$\left. \frac{\partial P_T}{\partial \mathbf{I}} \right|_{\mathbf{I}=\mathbf{I}_{\text{ext}}} = 2\mathbf{R}\mathbf{I}_{\text{ext}} + \mathbf{V}_{\text{dc}} = \mathbf{0} \quad (2.22)$$

which implies

$$\mathbf{I}_{\text{ext}} = -\frac{1}{2}\mathbf{R}^{-1}\mathbf{V}_{\text{dc}}. \quad (2.23)$$

It can then be shown that the second derivative of (2.21) is $2\mathbf{R}$. If $R_i \neq 0$ ($i = 1, 2, \dots, n$), then \mathbf{R} is symmetric and positive-definite (see Appendix B for proof) and, therefore, also nonsingular. Hence, $2\mathbf{R}$ is also a positive-definite matrix and, thus, P_T is minimum for the current given by (2.23), \mathbf{I}_{ext} . Substituting for \mathbf{I}_{ext} from (2.23) in (2.21), one finds

$$P_{T,\min} = -\frac{1}{4}\mathbf{V}_{\text{dc}}^T \mathbf{R}^{-1} \mathbf{V}_{\text{dc}}, \quad (2.24)$$

where $P_{T,\min}$ is the minimum of P_T and is always negative.

Equation (2.24) gives the minimum of P_T for a real-valued set of currents. In other words, if P_T is smaller than $P_{T,\min}$, i.e., if the power collectively absorbed by the dc-dc converters exceeds the absolute value of $P_{T,\min}$, then the power loss of the dc network becomes excessive and (2.21) fails to yield a real-valued solution. Thus, if a steady state

exists, the following inequality holds:

$$P_T \geq P_{T,min}. \quad (2.25)$$

Inequality (2.25) represents a necessary condition for the existence of a steady state for the dc system. Thus, a steady state does not exist if the aggregate power absorbed by the dc-dc converters is greater than the absolute value of $P_{T,min}$. However, if inequality (2.25) holds, one cannot guarantee the existence of a steady state for the system. It is also interesting to note that for a single-source/single-load resistive circuit, the absolute value of the right-hand side of (2.25) is the maximum power that can be transferred to the load, corresponding to the case of the source Thevenin resistance being equal to the load resistance.

2.3.2 State-space model

Linearizing the equation set (2.13), one finds

$$C_i \frac{d\tilde{v}_i}{dt} = -\frac{P_{dc_i}^*}{V_i^2} \tilde{v}_i - \tilde{i}_i \quad (2.26)$$

where “ \sim ” denotes small-signal perturbation of a variable, and V_i is the steady-state value of v_i .

Rewriting equation sets (2.12) and (2.26) in the matrix form, one obtains

$$\mathbf{L} \frac{d\tilde{\mathbf{i}}}{dt} = -\mathbf{R}\tilde{\mathbf{i}} + \tilde{\mathbf{v}} \quad (2.27)$$

$$\mathbf{C} \frac{d\tilde{\mathbf{v}}}{dt} = -\tilde{\mathbf{i}} - \mathbf{P}\tilde{\mathbf{v}} \quad (2.28)$$

where

$$\mathbf{L} = \mathbf{L}_0 + \mathbf{L}_b, \quad (2.29)$$

and

$$\mathbf{C} = \begin{bmatrix} C_1 & 0 & \cdots & 0 \\ 0 & C_2 & \cdots & 0 \\ \vdots & \vdots & \ddots & \vdots \\ 0 & 0 & \cdots & C_n \end{bmatrix}, \quad \mathbf{P} = \begin{bmatrix} \frac{P_{dc1}^*}{V_1^2} & 0 & \cdots & 0 \\ 0 & \frac{P_{dc2}^*}{V_2^2} & \cdots & 0 \\ \vdots & \vdots & \ddots & \vdots \\ 0 & 0 & \cdots & \frac{P_{dcn}^*}{V_n^2} \end{bmatrix}. \quad (2.30)$$

If $C_i \neq 0$ and $L_i \neq 0$ ($i = 1, 2, \dots, n$), then \mathbf{C} and \mathbf{L} are symmetric, positive-definite (see Appendix B), and, therefore, nonsingular matrices.

Equations (2.27) and (2.28) can be combined into a classical state-space form as

$$\dot{\mathbf{x}} = \mathbf{A}\mathbf{x} \quad (2.31)$$

where

$$\mathbf{x} = \begin{bmatrix} \tilde{\mathbf{i}} \\ \tilde{\mathbf{v}} \end{bmatrix}_{2n \times 1}, \quad \mathbf{A} = \begin{bmatrix} -\mathbf{L}^{-1}\mathbf{R} & \mathbf{L}^{-1} \\ -\mathbf{C}^{-1} & -\mathbf{C}^{-1}\mathbf{P} \end{bmatrix}_{2n \times 2n}. \quad (2.32)$$

Matrix \mathbf{A} can be expressed as

$$\begin{aligned} \mathbf{A} &= \begin{bmatrix} -\mathbf{L}^{-1} & \mathbf{0}_{n \times n} \\ \mathbf{0}_{n \times n} & -\mathbf{C}^{-1} \end{bmatrix} \begin{bmatrix} \mathbf{R} & -\mathbf{I}_{n \times n} \\ \mathbf{I}_{n \times n} & \mathbf{P} \end{bmatrix} \\ &= \mathbf{N}^{-1}\mathbf{M} \end{aligned} \quad (2.33)$$

where

$$\mathbf{N} = \begin{bmatrix} -\mathbf{L} & \mathbf{0}_{n \times n} \\ \mathbf{0}_{n \times n} & -\mathbf{C} \end{bmatrix}, \quad \mathbf{M} = \begin{bmatrix} \mathbf{R} & -\mathbf{I}_{n \times n} \\ \mathbf{I}_{n \times n} & \mathbf{P} \end{bmatrix}, \quad (2.34)$$

and \mathbf{N} is a symmetric, negative-definite (and, therefore, non-singular) matrix.

For stability analysis, one must evaluate the eigenvalues of \mathbf{A} in (2.31). Let λ be an eigenvalue of \mathbf{A} . Then one can write

$$\mathbf{A}\mathbf{w} = \lambda\mathbf{w}, \quad \mathbf{w} \neq \mathbf{0}, \quad (2.35)$$

where \mathbf{w} is an eigenvector of \mathbf{A} , associated with λ . Substituting for \mathbf{A} in (2.35) from (2.33), one finds

$$\mathbf{N}^{-1}\mathbf{M}\mathbf{w} = \lambda\mathbf{w}. \quad (2.36)$$

Pre-multiplying (2.35) by \mathbf{N} , one obtains

$$\mathbf{M}\mathbf{w} = \lambda\mathbf{N}\mathbf{w}, \quad (2.37)$$

Calculating the conjugate transpose of (2.37), one finds

$$\bar{\mathbf{w}}\mathbf{M}^T = \bar{\lambda}\bar{\mathbf{w}}\mathbf{N}, \quad (2.38)$$

where $\bar{\lambda}$ is the complex conjugate of λ , $\bar{\mathbf{w}}$ is the adjoint of \mathbf{w} , and \mathbf{M}^T is the transpose

of \mathbf{M} .

Pre-multiplying both sides of (2.37) by $\bar{\mathbf{w}}$, and post-multiplying both sides of (2.38) by \mathbf{w} , one finds

$$\bar{\mathbf{w}}\mathbf{M}\mathbf{w} = \lambda\bar{\mathbf{w}}\mathbf{N}\mathbf{w} \quad (2.39)$$

$$\bar{\mathbf{w}}\mathbf{M}^T\mathbf{w} = \bar{\lambda}\bar{\mathbf{w}}\mathbf{N}\mathbf{w}. \quad (2.40)$$

Adding the corresponding sides of (2.39) and (2.40), one concludes

$$\bar{\mathbf{w}}(\mathbf{M} + \mathbf{M}^T)\mathbf{w} = 2\text{Re}(\lambda)\bar{\mathbf{w}}\mathbf{N}\mathbf{w}. \quad (2.41)$$

In (2.41), \mathbf{N} is a real, symmetric, negative-definite matrix. Therefore, the real part of λ is negative if $(\mathbf{M} + \mathbf{M}^T)$ is a positive-definite matrix.

$$\bar{\mathbf{w}}(\mathbf{M} + \mathbf{M}^T)\mathbf{w} = \begin{bmatrix} \bar{\mathbf{w}}_1 & \bar{\mathbf{w}}_2 \end{bmatrix} \begin{bmatrix} 2\mathbf{R} & \mathbf{0}_{n \times n} \\ \mathbf{0}_{n \times n} & 2\mathbf{P} \end{bmatrix} \begin{bmatrix} \mathbf{w}_1 \\ \mathbf{w}_2 \end{bmatrix} \quad (2.42)$$

$$= 2\bar{\mathbf{w}}_1\mathbf{R}\mathbf{w}_1 + 2\bar{\mathbf{w}}_2\mathbf{P}\mathbf{w}_2 \quad (2.43)$$

where

$$\mathbf{w} = \begin{bmatrix} \mathbf{w}_1 \\ \mathbf{w}_2 \end{bmatrix}. \quad (2.44)$$

As mentioned earlier, \mathbf{R} is a positive-definite matrix and, based on (2.35) and (2.44), \mathbf{w}_1 and \mathbf{w}_2 cannot both be zero. Therefore, $(\mathbf{M} + \mathbf{M}^T)$ is positive-definite if \mathbf{P} is positive-definite. Hence, the dc system is stable if \mathbf{P} is positive-definite:

$$\mathbf{P} > 0 \Rightarrow \text{Re}(\lambda) < 0. \quad (2.45)$$

Since \mathbf{P} is a diagonal matrix, it is positive-definite if its diagonal elements are all positive, i.e., if the dc-dc converters all deliver power to the dc system. However, it should be pointed out that the inequality (2.45) is a sufficient condition for stability of the dc system. Thus, one cannot comment on the stability of the dc system if \mathbf{P} is positive-semidefinite, negative-definite, or indefinite, i.e., if some converters absorb power. Therefore, to evaluate the stability of the dc system, one must evaluate the eigenvalues of \mathbf{A} , as explained next.

Equation (2.37) can be rewritten as

$$(\mathbf{M} - \lambda\mathbf{N}) \mathbf{w} = \mathbf{0}, \quad \mathbf{w} \neq \mathbf{0}. \quad (2.46)$$

Substituting for \mathbf{M} and \mathbf{N} from (2.34) in (2.46), one can arrive at the following expression for the determinant of $\mathbf{M} - \lambda\mathbf{N}$, which, in turn, is the characteristic equation associated with (2.31):

$$\begin{vmatrix} \mathbf{R} + \lambda\mathbf{L} & -\mathbf{I}_{n \times n} \\ \mathbf{I}_{n \times n} & \mathbf{P} + \lambda\mathbf{C} \end{vmatrix} = 0, \quad (2.47)$$

which can be rewritten as [56]

$$\left| (\mathbf{R} + \lambda\mathbf{L})(\mathbf{P} + \lambda\mathbf{C}) + \mathbf{I}_{n \times n} \right| = 0. \quad (2.48)$$

Let us now express (2.48) in the form

$$\begin{vmatrix} \alpha_1 + \beta_1 & \alpha_2 & \cdots & \alpha_n \\ \alpha_1 & \alpha_2 + \beta_2 & \cdots & \alpha_n \\ \vdots & \vdots & \ddots & \vdots \\ \alpha_1 & \alpha_2 & \cdots & \alpha_n + \beta_n \end{vmatrix} = 0 \quad (2.49)$$

where

$$\alpha_i = \lambda^2 L_0 C_i + \lambda \left(R_0 C_i + \frac{P_{dci}^*}{V_i^2} L_0 \right) + \frac{P_{dci}^*}{V_i^2} R_0 \quad (2.50)$$

and

$$\beta_i = \lambda^2 L_i C_i + \lambda \left(R_i C_i + \frac{P_{dci}^*}{V_i^2} L_i \right) + \left(1 + \frac{P_{dci}^*}{V_i^2} R_i \right). \quad (2.51)$$

It can then be shown (see Appendix C) that (2.49) is equivalent to the $2n$ th-order polynomial equation

$$\prod_{i=1}^n \beta_i + \sum_{i=1}^n (\alpha_i \prod_{\substack{k=1 \\ k \neq i}}^n \beta_k) = 0, \quad (2.52)$$

which is remarkably easier to solve, from a computational burden standpoint, relative to a direct calculation of the eigenvalues of \mathbf{A} (i.e., using matrix operations); this facilitates physical implementation of the method on an embedded signal-processing platform.

A special case deserves some inspection: let R_0 and L_0 be zero. Then, matrices \mathbf{R}

and \mathbf{L} are diagonal and, therefore, $\mathbf{R} + \lambda\mathbf{L}$ takes the form

$$\mathbf{R} + \lambda\mathbf{L} = \begin{bmatrix} R_1 + \lambda L_1 & 0 & \cdots & 0 \\ 0 & R_2 + \lambda L_2 & \cdots & 0 \\ \vdots & \vdots & \ddots & \vdots \\ 0 & 0 & \cdots & R_n + \lambda L_n \end{bmatrix}. \quad (2.53)$$

Since \mathbf{C} and \mathbf{P} are diagonal matrices, (2.48) can be rewritten as

$$\begin{vmatrix} (R_1 + \lambda L_1) \left(\frac{P_{dc1}^*}{V_1^2} + \lambda C_1 \right) + 1 & \cdots & 0 \\ \vdots & \ddots & \vdots \\ 0 & \cdots & (R_n + \lambda L_n) \left(\frac{P_{dcn}^*}{V_n^2} + \lambda C_n \right) + 1 \end{vmatrix} = 0 \quad (2.54)$$

and

$$\prod_{k=1}^n \left[(R_k + \lambda L_k) \left(\frac{P_{dck}^*}{V_k^2} + \lambda C_k \right) + 1 \right] = 0. \quad (2.55)$$

Equation (2.55) implies that the dc system is stable if the power setpoint of each dc-dc converter satisfies the corresponding following two constraints:

$$P_{dck}^* > -\frac{V_k^2}{R_k}, \quad (2.56)$$

and

$$P_{dck}^* > -\frac{R_k C_k V_k^2}{L_k}, \quad (k = 1, 2, \dots, n). \quad (2.57)$$

It should be pointed out that, typically, (2.57) is the ruling constraint.

The foregoing conclusion is expected in view of the fact that the special case corresponds to a dc system that consists of n independently energized dc-dc converters, and it is important as it enables one to gain insights into the impact of parameters on the stability, in general. For example, one can expect the stability to improve as larger capacitances are chosen for the dc-dc converters, whereas larger network inductances are detrimental to the stability. Further, (2.57) indicates that larger line resistances improve the stability. However, an increase in resistances is not a remedial option as the power loss in the system will also increase. Therefore, to overcome this problem, an active damping method has been proposed in [40] to virtually increase the resistance while avoiding physical resistances. An increase in the dc voltage level of the system also improves the stability, as (2.57) indicates. However, a higher dc voltage level has safety and

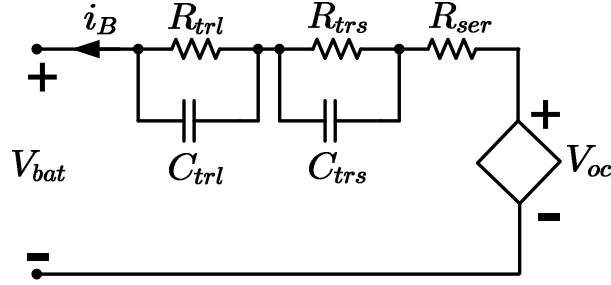


Figure 2.10: Realistic battery model.

operational implications and, naturally, translates into a higher cost.

2.4 Simulation Results

To demonstrate the accuracy of the developed model, the equation set (2.31)-(2.32), hereafter referred to as the “linear model”, is numerically solved in the MATLAB software environment, and the response predicted by it is compared with the response obtained from a detailed switched model of the dc system, Fig. 2.2, in the PSCAD/EMTDC software environment. The parameters used for simulation studies and model validation are given in Appendix D, unless otherwise is mentioned.

The study dc system includes six dc-dc converters, one for a PV system and the remainder for five vehicles. The network-side current of the PV system converter is represented by i_1 , whereas i_2 through i_6 signify the network-side currents of the vehicle converters (battery chargers).

2.4.1 Realistic Battery Model

The battery in Fig. 2.7 has been modeled by an ideal voltage source. Figure 2.10 shows a more realistic model of a Li-ion battery [57]. The model consists of a dc voltage source, V_{oc} to represent the open-circuit voltage of the battery, a series resistor, R_{ser} , and two RC parallel network, (R_{trs}, C_{trs}) and (R_{trl}, C_{trl}) to model the transient behavior of the battery. It can be assumed that the value of the resistors and capacitors in the model are constant over the SOC range of 20% to 100% [57].

To build a battery module with high voltage and capacity, multiple low-voltage, low-capacity battery cells should be connected in series and parallel. In this thesis, the voltage of the battery module in the PEVs is considered to be 320 V. Therefore, using a 4.1 V, 0.85 Ah battery cell, 78 battery cells must be connected in series to form a branch and

build the voltage ($N_{cell_ser} = 78$). To increase the battery capacity, multiple branches are needed to be connected in parallel. Thus, for a typical 40 kWh battery module, 147 branches are needed ($N_{branch_par} = 147$). To find the parameters of the realistic model for the battery module, one can use the following equations [58]

$$V_{oc}(module) = N_{cell_ser}V_{oc}(cell), \quad R_{ser}(module) = \frac{N_{cell_ser}}{N_{branch_par}}R_{ser}(cell),$$

$$R_{trs}(module) = \frac{N_{cell_ser}}{N_{branch_par}}R_{trs}(cell), \quad C_{trs}(module) = \frac{N_{branch_par}}{N_{cell_ser}}C_{trs}(cell),$$

$$R_{trl}(module) = \frac{N_{cell_ser}}{N_{branch_par}}R_{trl}(cell), \quad C_{trl}(module) = \frac{N_{branch_par}}{N_{cell_ser}}C_{trl}(cell).$$

Table 2.1 lists the parameters of a 4.1 V, 850-mAh TCL PL-383562 Li-ion battery cell which is the building block of a 320 V, 40 kWh battery module [57]. As Table 2.1 indicates, the time constants $R_{trs}C_{trs}$ and $R_{trl}C_{trl}$ for the battery module are 31.8 s and 219.2 s, respectively. These time constant values are very large comparing to the time scale of the network-side dynamics of the dc-dc converter, and therefore, their impact on the transient behavior of the dc-dc converter is negligible. Fig. 2.11 shows the responses of a battery charger to a step change in the power setpoint from 0 to -10 kW. The responses have been illustrated for two cases: (i) when the battery has been modeled by an ideal voltage source of 320 V, and (ii) when the battery has been modeled by a realistic battery model of Fig. 2.10 with parameters of Table 2.1. In this test, at $t = 0.8$ s, the power setpoint of the battery charger is changed from 0 to -10 kW, meaning that the battery is started to being charged. As Fig. 2.11 shows, although there are some discrepancies in battery voltage, V_{bat1} , between realistic model and the ideal voltage source, the battery current, i_{B1} , and the power between the battery charger and the rest of dc system, P_{dc2} , are almost identical for two cases. In fact, due to constant-power property of the dc-dc converter, the battery voltage fluctuations don't have any impact on the network-side dynamics of the converter as depicted in Fig. 2.11, and therefore, hereafter in this thesis, the ideal voltage source will be used to model the batteries. It should also be noted that in commercially-available standard chargers on the market, the maximum charging or discharging power of the battery is a function of the battery voltage which is a function of length of charging or discharging. However, as the power setpoint of the battery charger is updated infrequently, this is not a source of instability in this thesis. A more sophisticated treatment would still result in a monotonically changing value and hence

Table 2.1: Parameters of a typical battery cell and battery module

	Parameter	Battery cell	Battery module
Nominal Voltage (V)	V_{oc}	4.1	320
Capacity (Ah)	B_{cap}	0.85	125
Internal resistance (m Ω)	R_{ser}	74	39
Transient resistances (m Ω)	R_{trs}	46	24
	R_{trl}	49	26
Transient capacitances (F)	C_{trs}	703	1326
	C_{trl}	4475	8433

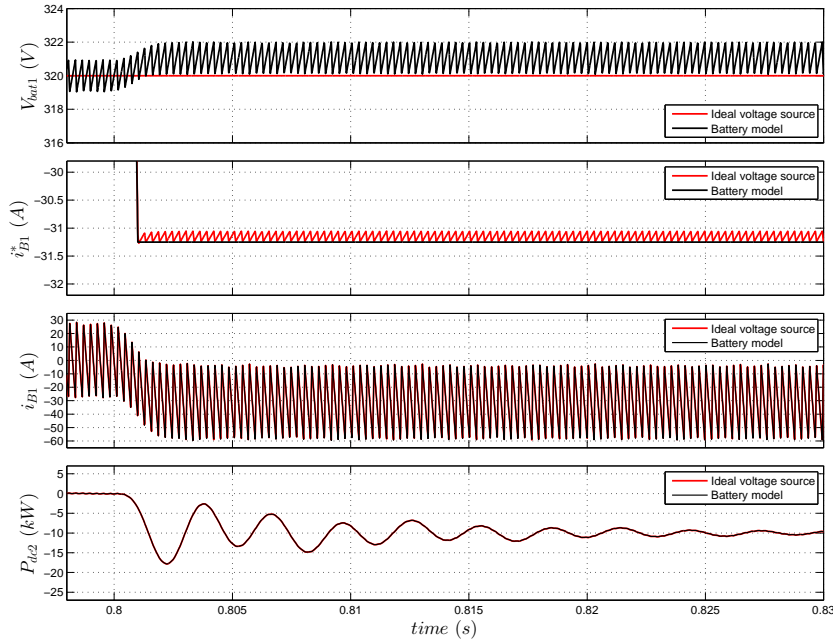


Figure 2.11: Response of a battery charger for two models for the battery: ideal voltage source and realistic battery model.

would still not affect stability.

2.4.2 Case 1: Stable Pre- and Post-Disturbance Operation

Initially, the dc system is in a steady state, while the PV system delivers 50 kW (through Converter #1), the first vehicle absorbs 10 kW (via Converter #2), the second and third electric vehicles deliver 20 kW each, and the remaining two vehicles absorb 20 kW each. Then at $t = 1.3$ s, the power setpoint of Converter #2 is changed stepwise from -10 kW to -20 kW. Fig. 2.12 depicts the responses of the variables i_1 , i_2 , i_3 , and P_{dc2} , and demonstrating a close agreement between the linear and detailed models. Fig. 2.12 also shows that, as assumed, v_{dc} remains tightly regulated about its pre-disturbed steady-state

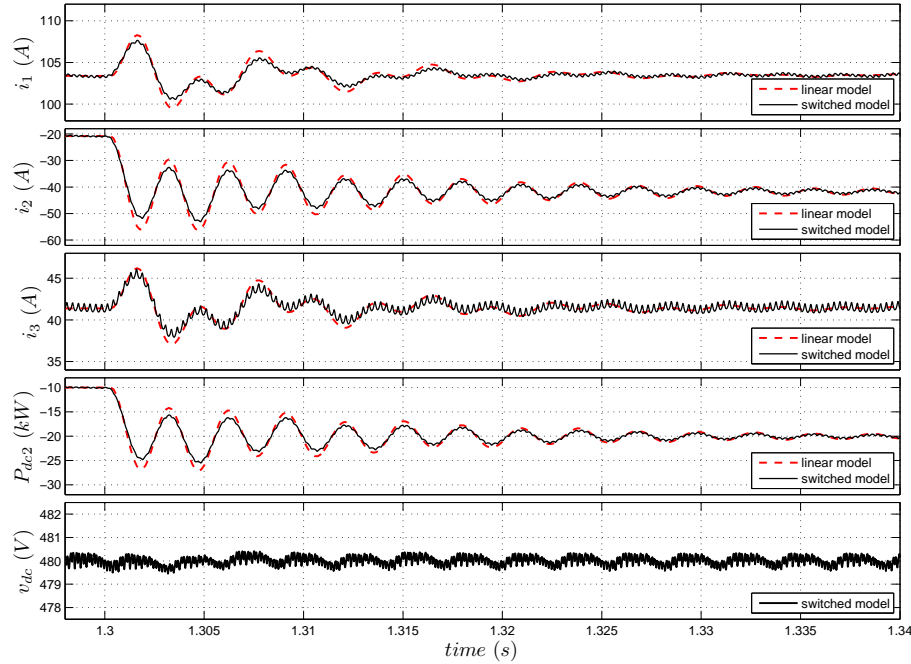


Figure 2.12: Response of the dc-system to a change in P_{dc2} from -10 kW to -20 kW when P_{dc1} is 50 kW and P_{dc3} to P_{dc6} are -20 kW.

value.

Fig. 2.13 shows the results of another test, one in which Converter #3 (corresponding to the second vehicle) delivers power to the rest of the dc system. In this case, the dc system is initially in a steady state, while the PV system produces 50 kW, Converter #2 absorbs 50 kW, Converter #3 delivers 20 kW, and every other converter absorbs 20 kW. Then, the power setpoint of Converter #3 is changed stepwise from 20 kW to 30 kW, at $t = 1.3$ s. Fig. 2.13 illustrates a close agreement between the linear and detailed models in predicting the responses of i_1 , i_2 , i_3 , and P_{dc3} .

2.4.3 Case 2: Sensitivity to Cable Length

To evaluate the sensitivity to the length of the interconnection cables, an eigenvalue analysis has been conducted using the linear model, and Fig. 2.14 illustrates the dependence of the dominant eigenvalues of the dc system on the network cable length. In this case, the PV system generates a power of 10 kW, Converter #2 absorbs 70 kW, and every other converter absorbs 60 kW. Thus, the length of the cables, connecting the dc bus to the central VSC and the dc-dc converters, are increased from 100 m to 500 m. As illustrated in Fig. 2.14, the eigenvalues move toward the imaginary axis if the length of

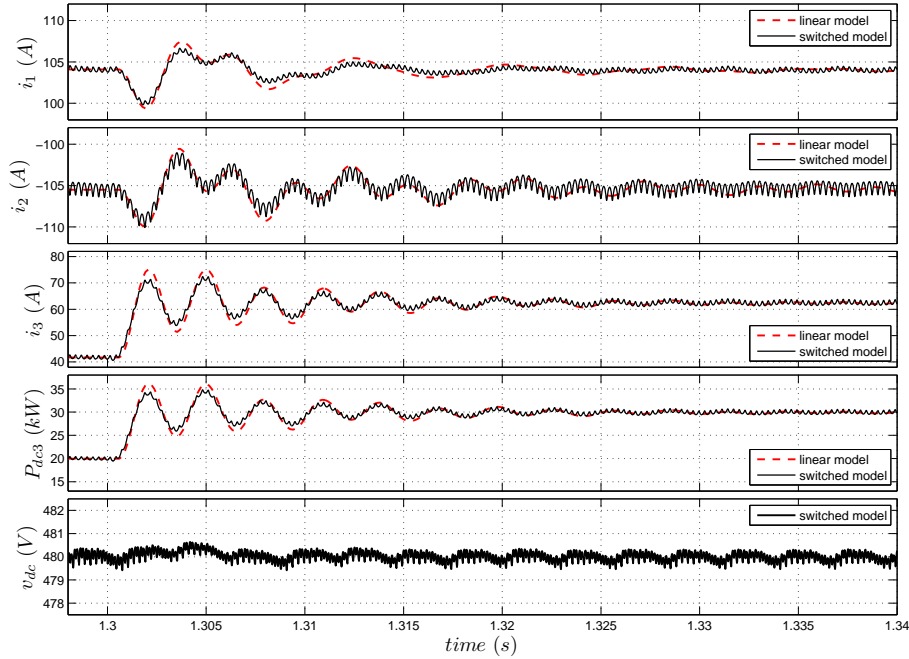


Figure 2.13: Response of the dc-system to a change in P_{dc3} from 20 kW to 30 kW when P_{dc1} is 50 kW and P_{dc2} is -50 kW and P_{dc4} to P_{dc6} are -20 kW.

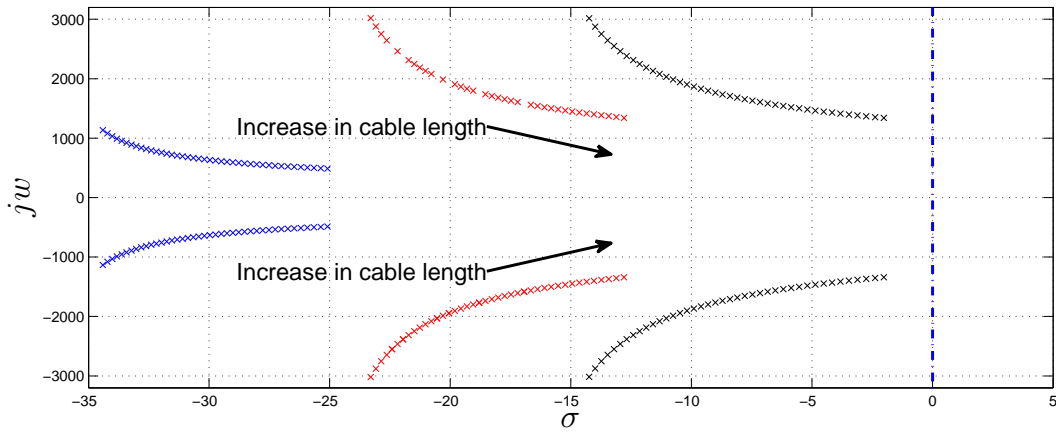


Figure 2.14: Eigenvalue migration plot as a function of the length of the interconnection cables.

the interconnection cables increase.

2.4.4 Case 3: Sensitivity to Network-Side Capacitances

Fig. 2.15 illustrates the dependance of the stability of the dc system on the network-side capacitances of the converters. For this case, it is assumed that the PV system delivers 10 kW, Converter #2 absorbs 80 kW, and any other converter absorbs 70 kW. Thus, three

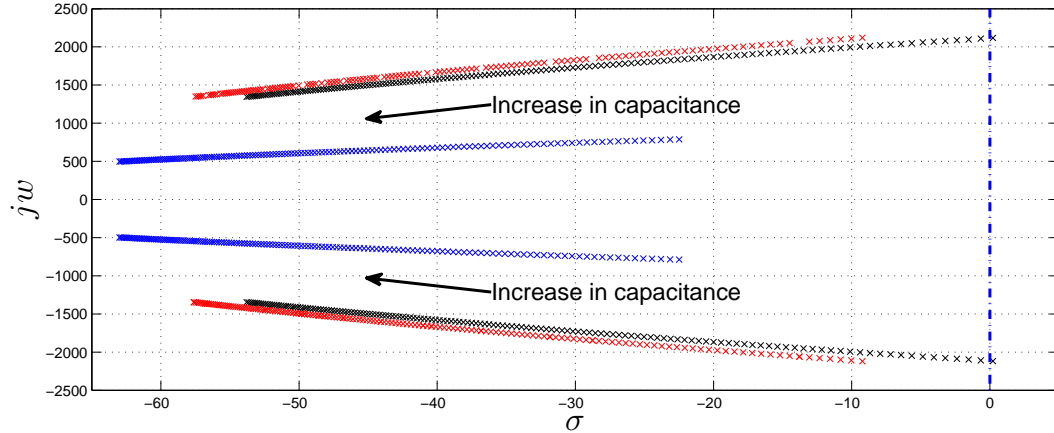


Figure 2.15: Eigenvalue migration plot as a function of network-side capacitance.

dominant pairs of eigenvalues have been marked on the complex plane for the network-side capacitances equally ranging from $2000 \mu F$ to $5000 \mu F$. As Fig. 2.15 shows, the eigenvalues move away from the imaginary axis as the network-side capacitances increase, indicating the stabilizing effect of the network-side capacitances.

2.4.5 Case 4: Sensitivity to Power Absorption

Fig. 2.16 illustrates the migration of the dominant pair of eigenvalues (i.e., the pair with the real part smallest in absolute value), as the power absorbed by Converter #2 is increased, for three different values of network-side capacitances of the converters. It is assumed for this case that the PV system generates 10 kW, while, except Converter #2, each converter absorbs 70 kW. Thus, the eigenvalue loci are mapped on the complex plane for the power of Converter #2 ranging from -20 kW to -80 kW. As Fig. 2.16 indicates, irrespective of the value of the network-side capacitances, the eigenvalues approach the imaginary axis as the power absorbed by Converter #2 increases. This study case illustrates what is well known as the destabilizing effect of the so-called constant-power loads [20], [28], [59], [40]- [60].

Fig. 2.16 also indicates that the maximum amount of power that Converter #2 can absorb before the system becomes unstable decrease as the network-side capacitances are made smaller. This is consistent with the findings of Fig. 2.15.

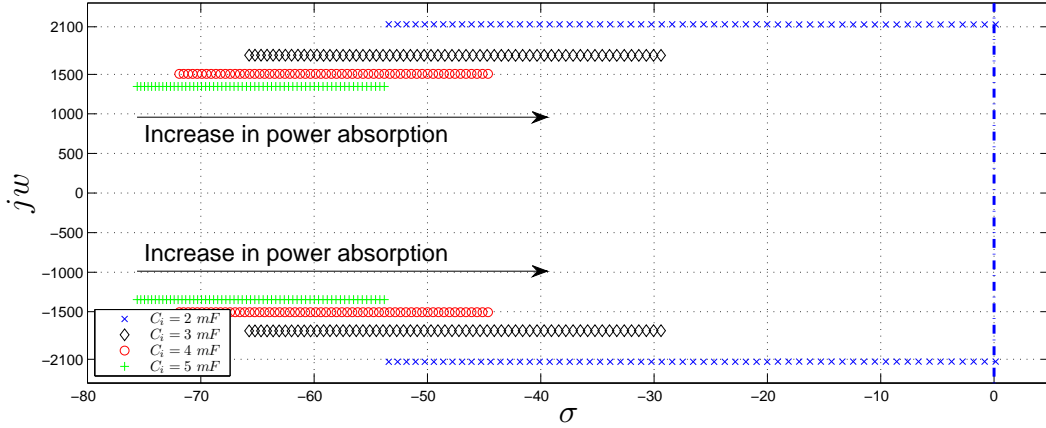


Figure 2.16: Eigenvalue migration plot as a function of power consumption by dc-dc converter #2.

2.4.6 Case 5: Unstable Post-Disturbance Operation

In the last study case, the dc system is assumed to initially be in a steady state, with the PV system generating 10 kW, Converter #2 absorbing 60 kW, and every other converter absorbing 70 kW. Moreover, each converter has a network-side capacitance of $2000 \mu F$. Then, the power setpoint of Converter #2 is changed stepwise from -60 kW to -80 kW, at $t = 1.3$ s. As previously illustrated by Figs. 2.15 and 2.16, the new set of powers results in a pair of imaginary eigenvalues, about $\pm 2100j$ rad/s, and, consequently, destabilizes the system, as Fig. 2.17 indicates. It is observed that the period of oscillations is about 3 ms ($\simeq 2\pi/2100$ s), confirming that the linear and detailed models closely agree.

2.5 dc System with Multiple Nodes of Coupling

Fig 2.18 illustrates a configuration where no common node of coupling exists, but the converters are connected to the network at different corresponding nodes of coupling; the impedance between two adjacent nodes is represented by the series connection of an inductance, L_{bi} , and a resistance, R_{bi} .

The dynamics of the system of Fig. 2.18 are governed by the following differential

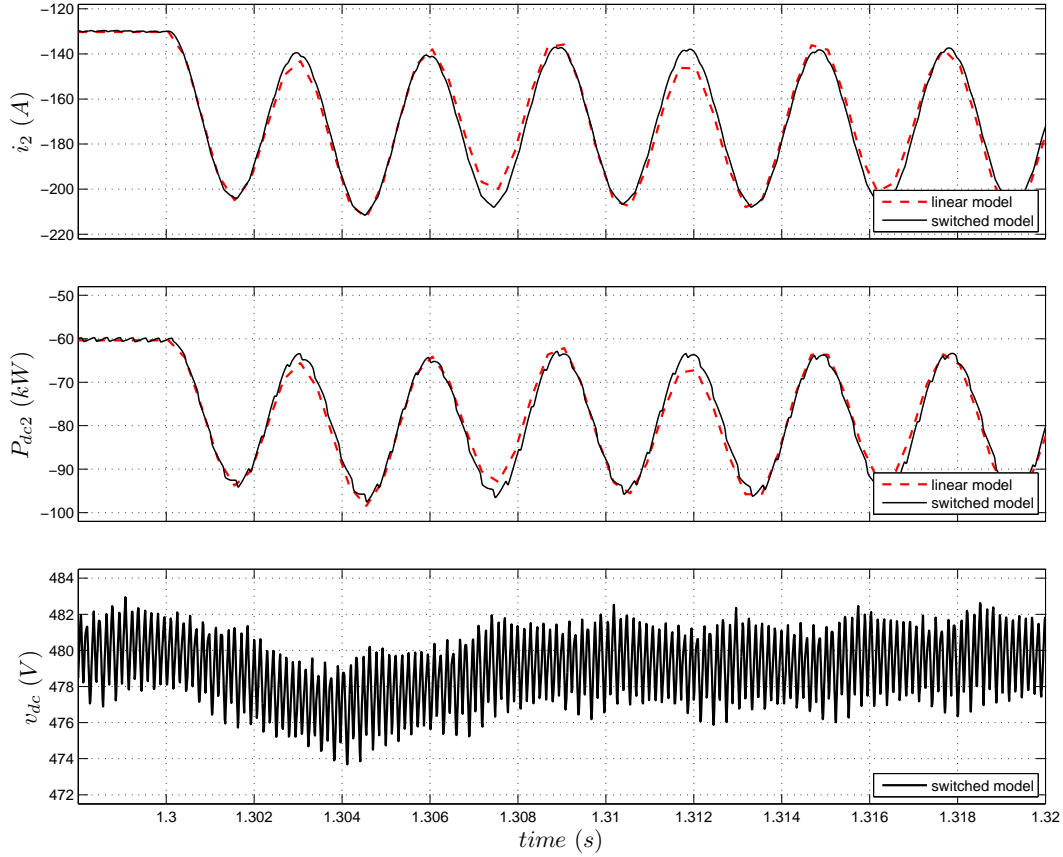


Figure 2.17: Response of the dc-system to a change in P_{dc2} from -60 kW to -80 kW when P_{dc1} is 10 kW, and P_{dc3} to P_{dc6} are -70 kW.

equations:

$$-v_i + R_i i_i + L_i \frac{di_i}{dt} + R_{b1} \sum_{k=1}^n i_k + L_{b1} \sum_{k=1}^n \frac{di_k}{dt} \quad (2.58)$$

$$+ \dots + R_{bi} \sum_{k=i}^n i_k + L_{bi} \sum_{k=i}^n \frac{di_k}{dt} + v_{dc} = 0,$$

for $i = 1, 2, \dots, n-1$, and

$$-v_n + R_n i_n + L_n \frac{di_n}{dt} + R_{b1} \sum_{k=1}^n i_k + L_{b1} \sum_{k=1}^n \frac{di_k}{dt} \\ + \dots + R_{b(n-1)} \sum_{k=n-1}^n i_k + L_{b(n-1)} \sum_{k=n-1}^n \frac{di_k}{dt} + v_{dc} = 0,$$

$$C_i \frac{dv_i}{dt} = \frac{P_{dci}^*}{v_i} - i_i, \quad i = 1, 2, \dots, n. \quad (2.59)$$

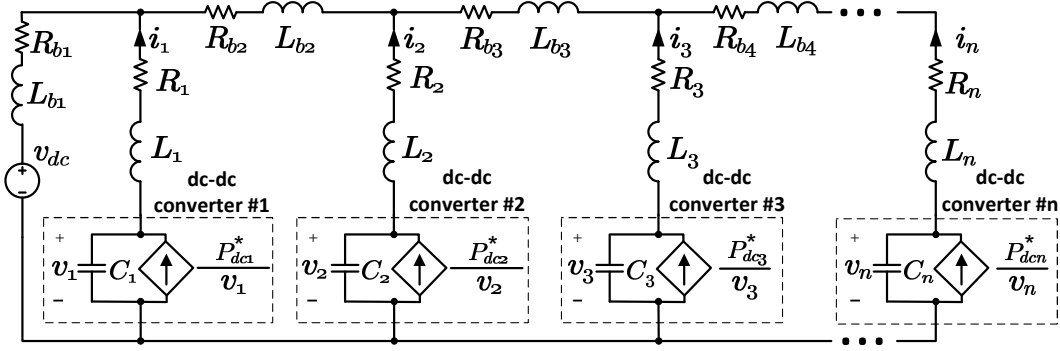


Figure 2.18: Equivalent circuit of the dc system with different nodes of coupling.

Linearizing (2.58) and (2.59), and expressing the resulting equations in the matrix form, one finds

$$\mathbf{L}_m \frac{d\tilde{\mathbf{i}}}{dt} = -\mathbf{R}_m \tilde{\mathbf{i}} + \tilde{\mathbf{v}} \quad (2.60)$$

$$\mathbf{C} \frac{d\tilde{\mathbf{v}}}{dt} = -\tilde{\mathbf{i}} - \mathbf{P}\tilde{\mathbf{v}} \quad (2.61)$$

where

$$\mathbf{L}_m = \mathbf{L}_n + \mathbf{L}_b, \quad (2.62)$$

$$\mathbf{R}_m = \mathbf{R}_n + \mathbf{R}_b, \quad (2.63)$$

$$\mathbf{L}_n = \begin{bmatrix} L_{b1} & L_{b1} & L_{b1} & \cdots & L_{b1} \\ L_{b1} & L_{b1} + L_{b2} & L_{b1} + L_{b2} & \cdots & L_{b1} + L_{b2} \\ L_{b1} & L_{b1} + L_{b2} & \sum_{i=1}^3 L_{bi} & \cdots & \sum_{i=1}^3 L_{bi} \\ \vdots & \vdots & \vdots & \ddots & \vdots \\ L_{b1} & L_{b1} + L_{b2} & \sum_{i=1}^3 L_{bi} & \cdots & \sum_{i=1}^{n-1} L_{bi} \\ L_{b1} & L_{b1} + L_{b2} & \sum_{i=1}^3 L_{bi} & \cdots & \sum_{i=1}^{n-1} L_{bi} \end{bmatrix}, \quad (2.64)$$

$$\mathbf{R}_n = \begin{bmatrix} R_{b1} & R_{b1} & R_{b1} & \cdots & R_{b1} \\ R_{b1} & R_{b1} + R_{b2} & R_{b1} + R_{b2} & \cdots & R_{b1} + R_{b2} \\ R_{b1} & R_{b1} + R_{b2} & \sum_{i=1}^3 R_{bi} & \cdots & \sum_{i=1}^3 R_{bi} \\ \vdots & \vdots & \vdots & \ddots & \vdots \\ R_{b1} & R_{b1} + R_{b2} & \sum_{i=1}^3 R_{bi} & \cdots & \sum_{i=1}^{n-1} R_{bi} \\ R_{b1} & R_{b1} + R_{b2} & \sum_{i=1}^3 R_{bi} & \cdots & \sum_{i=1}^{n-1} R_{bi} \end{bmatrix}, \quad (2.65)$$

and \mathbf{L}_b , \mathbf{R}_b , \mathbf{C} , and \mathbf{P} have been defined by (2.16) and (2.30), respectively.

It can be shown that \mathbf{R}_m and \mathbf{L}_m are positive-definite matrices. Therefore, one can employ the same approach as the one presented in Sections 2.3.1 and 2.3.2 to find a state-space model for the system.

2.6 Conclusion

A systematic method was presented for developing a model of a dc distribution system, based on the configuration of the system. The dc distribution system is assumed to host electric vehicles and photovoltaic (PV) modules, using dc-dc converters, and integrates them with an ac power grid. The developed model is of the matrix form and, therefore, can readily be expanded to represent a dc distribution system of any desired number of dc-dc converters. The model captures both the steady-state and dynamic characteristics of the system, and includes port capacitors of the converters, as well as the interconnection cables. Thus, it can be used for identifying the condition for existence of a steady state, as well as for stability analysis. Furthermore, an alternative set of characteristic equations was proposed that are less computationally intensive than the original matrix representation, for example, for on-line stability assessment tasks. The adequacy of the proposed model was demonstrated through a number of case studies conducted and compared in PSCAD/EMTDC and MATLAB software environments.

Chapter 3

Stability Enhancement of the DC Distribution System

3.1 Introduction

The dc distribution systems embedding dc-dc converters are prone to instability due to constant-power property of the dc-dc converters [28], [35]; the system becomes unstable if the powers absorbed by the battery chargers exceed certain values [20]. This phenomenon inflicts a limit on the maximum power that can be imported to charge the batteries and, consequently, precludes full utilization of the installed capacities and prolongs the charging times. Therefore, it is imperative to

1. systematically characterize the phenomenon and identify the prevailing constraints, and
2. devise a stability enhancement technique, in order to push the limits and expand the stable operating region of the dc system.

Expanding upon the idea proposed in [36], this chapter proposes a control technique for expanding the stable operating region of a dc distribution system integrating PHEVs via bidirectional dc-dc converters (battery chargers), such that the dc system and its PHEVs can import larger powers from the host ac grid. The proposed technique is simple, does not require information internal to the system or its embedded converters, and does not need hardware modifications. Rather, it only employs local measurements and individual power setpoints and, therefore, can be exercised in a decentralized fashion.

These, in turn, permit the use of commercially available dc-dc converters (battery chargers), expected to further reduce the overall cost of the system. The proposed technique is also applicable to other dc distribution systems, e.g., shipboard power systems, that have multiple power-electronic converters.

3.2 System Configuration

Fig. 3.1 illustrates a dc distribution system, for example, in a parking lot, that hosts PHEVs and photovoltaic (PV) modules. In this system, dc-dc converters are utilized as battery chargers for the PHEVs and also for interfacing the PV modules. Moreover, a central voltage-sourced converter (VSC) interfaces the dc distribution system to the host ac grid. A communication network [61] is used to enable the exchange of metering and control information for a management unit, to and from the dc-dc converters and the central VSC. The management unit calculates the limits of the power exchange setpoints and sends them to the dc-dc converters, to ensure that the dc system operates in its stable operation region. The PHEV owners, on the other hand, can set state-of charge (SOC) limits for their vehicles, to permit power exchanges only if the SOC resides within a certain range. For example, if the SOC is above 70%, then energy can be sold to the rest of the system, whereas if the SOC is below 40%, then the vehicle should buy energy from the rest of the system. The aforementioned limits (determined based on the trip plans, electricity price, and other factors) translate into power setpoints for the corresponding dc-dc converters. For example, for a PHEV with 20 kWh of battery capacity, if the SOC limit for energy export is 70% and the present SOC is 85%, then 3 kWh (that is, 15% of the battery capacity) can be sold by the PHEV to the rest of the system, meaning that the power setpoint of this particular PHEV can be set to export 9 kW of power in 20 minutes, or 3 kW of power in one hour, and so on [20].

Fig. 3.2 shows a simplified schematic diagram of the dc system. As the diagram indicates, the dc system consists of a central VSC, a network of RL branches representing the dc distribution network, and a multitude (3, here) of dc-dc power electronic converters that represent either the battery chargers of the PHEVs or the power-electronic interface of the PV system. The central VSC is interfaced with the host ac power grid via a three-phase tie reactor with a per-phase inductance of L_s ; the resistance R_s represents the aggregate effect of the ohmic power losses of the tie reactor and conduction power losses of the VSC. The central VSC regulates the dc voltage of the network. The PHEV

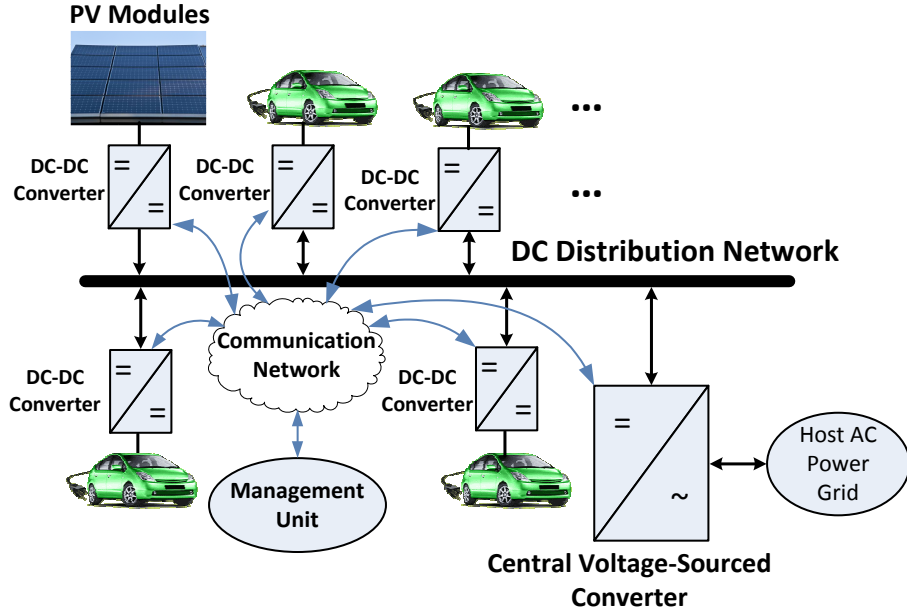


Figure 3.1: A dc bus for distribution of power in a parking lot for PHEVs.

battery chargers can draw or deliver power, the PV system delivers power, and the host ac grid compensates for any generation-consumption power mismatch, via the central VSC. A study system, whose parameters is reported in Appendix E, is used for stability analysis and performance evaluation in this chapter.

3.3 Mathematical Model

3.3.1 Central VSC

The central VSC and its control scheme act as a controlled dc-voltage power port, [53], and regulate the dc voltage of the network (Fig. 3.3 illustrates the concept). The VSC is current-controlled, such that its output real power, P_s , rapidly tracks the real-power setpoint, P_s^* , issued by a dc-voltage regulation loop (in this chapter, variables with superscript * signifies the setpoints). P_{dc} denotes the power that the rest of the dc system delivers to the VSC. As Fig. 3.3 indicates, a measure of P_{dc} is incorporated in the control loop, as a feed-forward signal, to mitigate the dynamic coupling between the dc-voltage regulation loop and the rest of the dc system.

As discussed in [53] and also in Chapter 2 of this thesis, the transfer function from

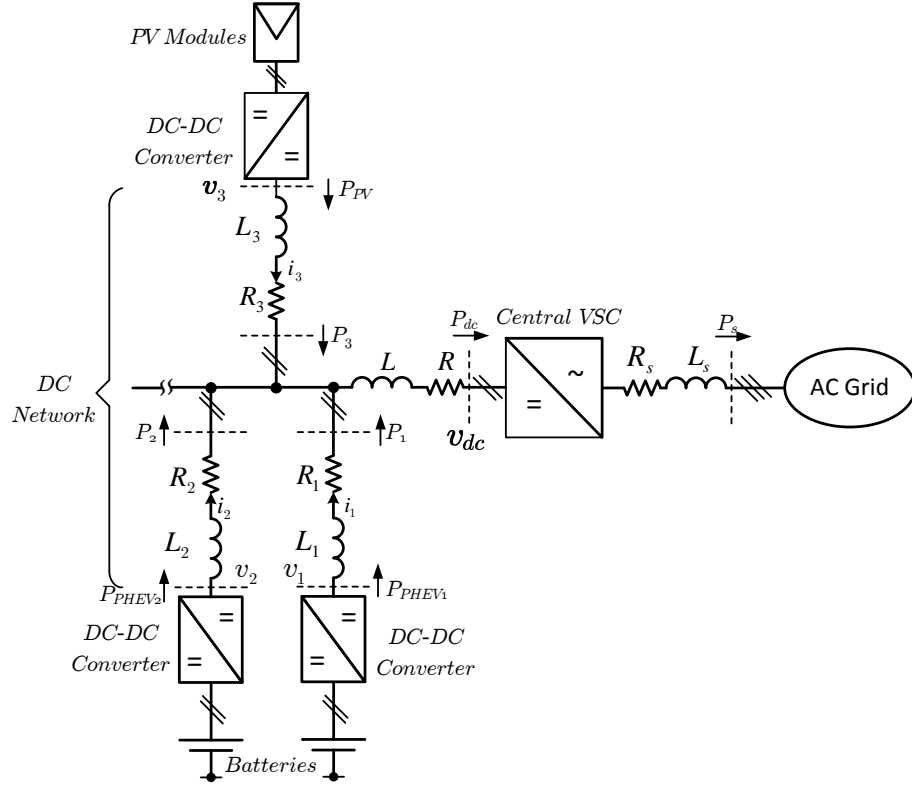


Figure 3.2: Schematic diagram of the dc system.

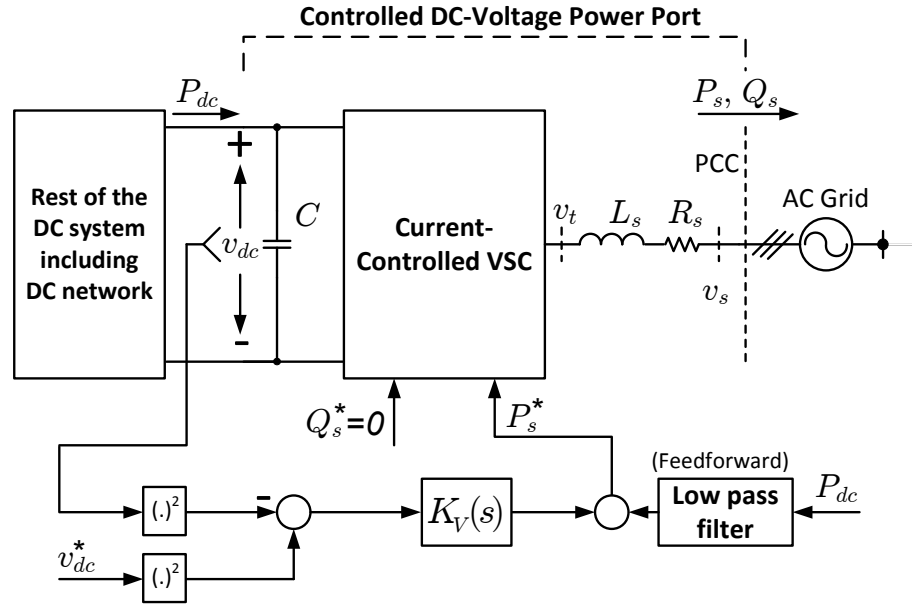


Figure 3.3: Simplified block diagram of the controlled dc-voltage power port.

\tilde{P}_s to \tilde{v}_{dc} is

$$G_v(s) = \frac{\tilde{v}_{dc}^2(s)}{\tilde{P}_s(s)} = - \left(\frac{2}{C} \right) \frac{\tau s + 1}{s}, \quad (3.1)$$

where the time constant τ is a function of the steady-state value of P_{dc} , i.e., P_{dc0} :

$$\tau = \frac{2L_s P_{dc0}}{3V_s^2}, \quad (3.2)$$

where V_s is the peak value of v_s , the line-to-neutral voltage of ac grid at the point of common coupling (PCC). As discussed in [53], τ is negative (corresponding to a non-minimum phase plant) if P_{dc0} is negative. Therefore, the dc-voltage regulation loop should be tuned for a case where the maximum amount of power flows from the ac grid towards the dc system to ensure stability also in other operating conditions.

In the remainder of this chapter, it is assumed that the controlled dc-voltage power port of Fig. 3 rapidly and tightly regulates v_{dc} at its setpoint v_{dc}^* , irrespective of the steady-state value or transient excursions of P_{dc} ; it is assumed that the dynamics of v_{dc} decay to zero rapidly.

3.3.2 dc-dc converters

The PHEV batteries exchange energy with the dc system through corresponding bidirectional dc-dc power-electronic converters which are referred, hereafter, to as the *battery chargers*. Fig. 3.4 shows a simplified schematic diagram of a full-bridge dc-dc converter which, with no loss of generality, is assumed to represent a battery charger (e.g., for the i^{th} PHEV of the dc system). The battery current, i_{Bi} , is regulated at its setpoint, i_{Bi}^* , by a feedback control loop in which a compensator, $K_i(s)$, processes the error ($i_{Bi}^* - i_{Bi}$) and generates the control signal u_i . A measure of the battery voltage, V_{bati} , is then added to u_i , and the resulting signal is divided by a measure of the network-side terminal voltage of the converter, v_i , to generate the pulse-width modulating (PWM) signal of the converter. In turn, i_{Bi}^* is calculated by dividing the battery power setpoint, P_{Bi}^* , by V_{bati} .

Assuming a fast and accurate current-control loop, the battery power P_{Bi} equals P_{Bi}^* . On the other hand, P_{Bi} is almost equal to the power that leaves the network-side port of the converter, P_{ti} ; the approximation is plausible in view of the typically small battery-side filter resistance R_{Bi} and inductance L_{Bi} (due to the typically large switching frequency of the converter), as well as negligible power losses of the converter. Therefore, $P_{ti} \simeq P_{Bi}^*$. Then, in a steady state, the terminal capacitance C_i is effectively open and the power that the battery charger delivers to the rest of the dc system, P_{PHEVi} , is equals P_{ti} and, therefore, P_{Bi}^* .

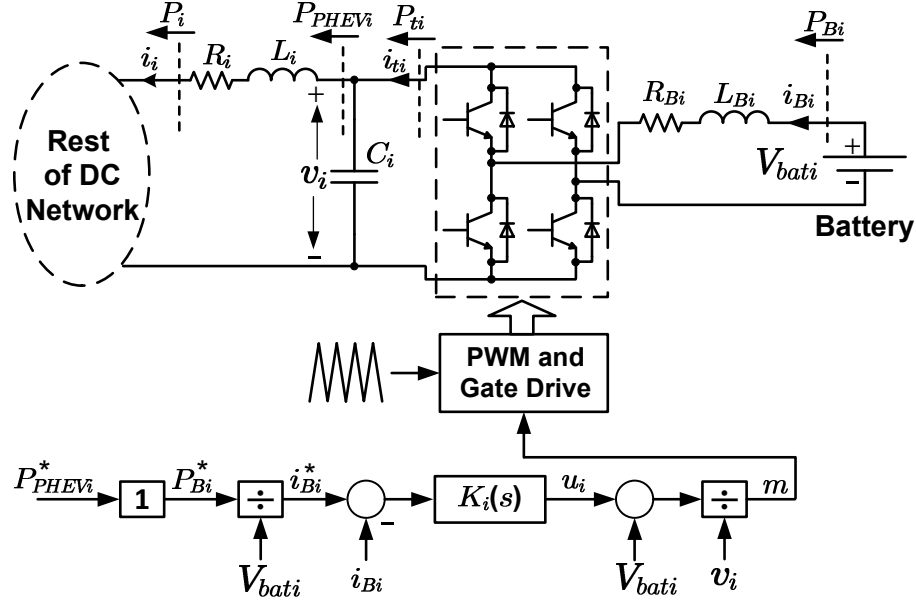


Figure 3.4: Schematic diagram of the bidirectional dc-dc converter as a battery charger for i^{th} PHEV.

Hence, P_{Bi}^* should be determined based on value of power one desires the battery charger to deliver to the rest of the dc system, i.e, the setpoint P_{PHEVi} , Fig. 3.4. The desirable fast current control can be ensured by proper design of $K_i(s)$. For example, as discussed in Chapter 2, if $K_i(s)$ is of the proportional-integral (PI) type, then its gains can be determined for a first-order closed-loop transfer function of the form

$$\frac{I_{Bi}(s)}{I_{Bi}^*(s)} = \frac{1}{\tau_{Bi}s + 1}, \quad (3.3)$$

for which the time constant τ_{Bi} is a design choice.

The current that leaves the positive network-side terminal of the converter is $i_{ti} = P_{ti}/v_i$, which based on the conclusion that $P_{ti} \simeq P_{Bi}^* = P_{PHEVi}^*$, can be written as

$$i_{ti} = \frac{1}{v_i} P_{PHEVi}^*. \quad (3.4)$$

Hence, from its network-side port, the converter can be represented by a dependent current source whose value is $i_{ti} = P_{PHEVi}^*/v_i$, as shown in Fig. 3.5. If P_{PHEVi}^* is an exogenous signal, i.e., if it does not depend on any other variable of the dc system, then P_{ti} is constant (from the viewpoint of dynamics) and, therefore, the converter presents itself as a constant-power element to the external world; any change in v_i is counteracted by a corresponding change in i_{ti} , such that P_{ti} remains constant at P_{PHEVi}^* . This constant-

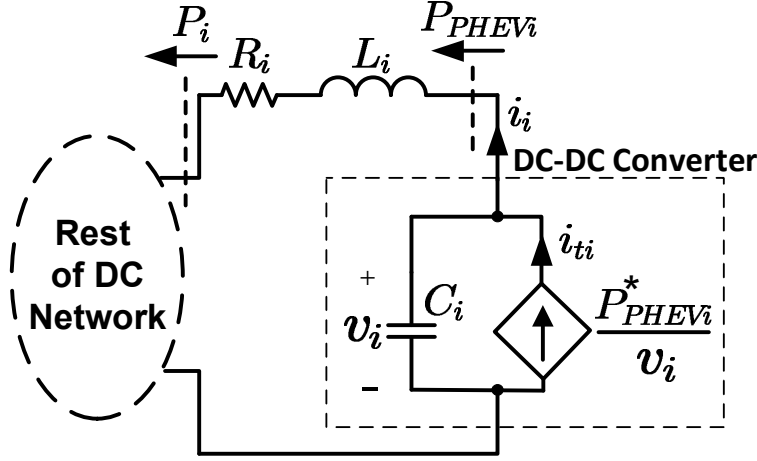


Figure 3.5: Simplified model of the dc-dc converter.

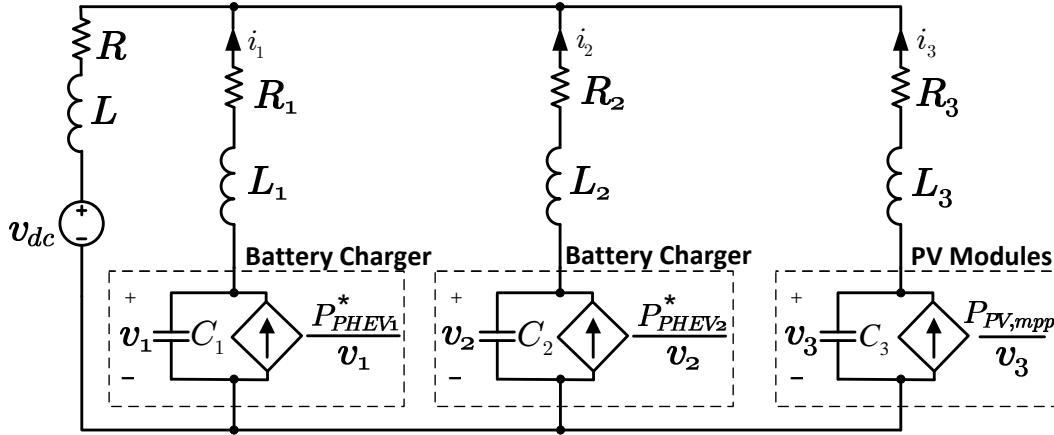


Figure 3.6: Equivalent circuit for the analysis of the dc system of Fig. 3.2.

power property of regulated power-electronic converters is known for giving rise to system instabilities, [29], as also demonstrated in Section 3.4.

In a PV system, the power-electronic interface is internally regulated so as to maintain the dc voltage of its host modules at a value that corresponds to the maximum-power point (MPP) under the prevailing sunlight and temperature conditions. Therefore, the model of Fig. 3.5 can be used also for a PV system, except that $P_{PHEV_i}^*$ is replaced with $P_{PV, mpp}$. Based on aforementioned discussions, Fig. 3.6 represents the equivalent circuit of the dc system of Fig. 3.2; $P_{PHEV_i}^*$ represents the power exchange setpoint of the i^{th} battery charger, and $P_{PV, mpp}$ signifies the maximum power of a PV array as imposed by the corresponding maximum powerpoint tracking (MPPT) scheme.

Based on Fig. 3.6, the following nonlinear differential equations describe the dynamic

behavior of the dc system of Fig. 3.2:

$$L \frac{d(i_1 + i_2 + i_3)}{dt} + L_1 \frac{di_1}{dt} = v_1 - v_{dc} - R(i_1 + i_2 + i_3) - R_1 i_1, \quad (3.5)$$

$$L_1 \frac{di_1}{dt} - L_2 \frac{di_2}{dt} = v_1 - v_2 - R_1 i_1 + R_2 i_2, \quad (3.6)$$

$$L_2 \frac{di_2}{dt} - L_3 \frac{di_3}{dt} = v_2 - v_3 - R_2 i_2 + R_3 i_3, \quad (3.7)$$

$$C_1 \frac{dv_1}{dt} = \frac{P_{PHEV1}^*}{v_1} - i_1, \quad (3.8)$$

$$C_2 \frac{dv_2}{dt} = \frac{P_{PHEV2}^*}{v_2} - i_2, \quad (3.9)$$

$$C_3 \frac{dv_3}{dt} = \frac{P_{PV,mppt}}{v_3} - i_3. \quad (3.10)$$

The steady-state values of the variables of the system can be calculated by setting the derivatives to zero in (3.5) through (3.10), and solving the nonlinear equations for every given set of power exchange setpoints P_{PHEV1}^* , P_{PHEV2}^* , and $P_{PV,mppt}$.

The linearized state-space representation of (3.5) through (3.10) can be expressed by

$$\dot{\mathbf{x}} = \mathbf{A}\mathbf{x}, \quad (3.11)$$

where $\mathbf{x} = [\tilde{i}_1 \ \tilde{i}_2 \ \tilde{i}_3 \ \tilde{v}_1 \ \tilde{v}_2 \ \tilde{v}_3]^T$ is the vector of state variables, and $\tilde{\cdot}$ denotes small-signal perturbation around steady-state operating points, and components of \mathbf{A} can be determined based on resistance and inductance of the cables, the capacitance of the converters, and steady-state operating point of the converters. The state-space model of (3.11) can be used for stability analysis of the dc system and in section 3.4, it will be shown that the dc system is prone to instability when the battery chargers are drawing energy from the ac power grid.

3.4 Stability Enhancement

Constant-power elements have been shown to have detrimental effects on the stability of their host dc distribution systems, if the direction of flow from the distribution system towards the constant-power elements [20], [28], [29]. Thus, to identify the boundary be-

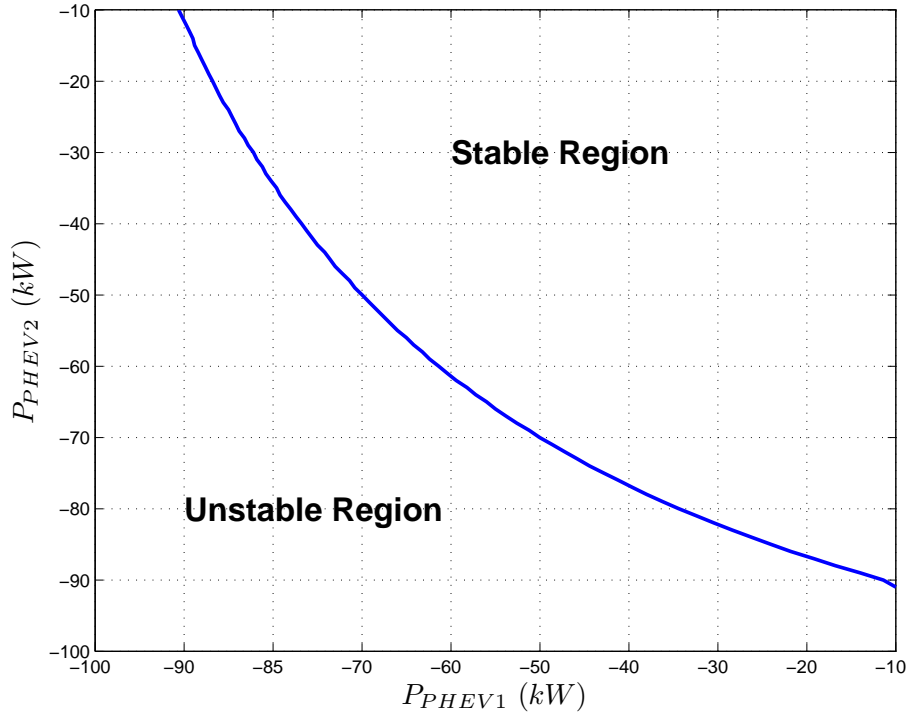


Figure 3.7: Stable and unstable regions in the charging mode.

tween the stable and unstable regions associated with the study system, an algorithm has been executed in Matlab software environment, such that for any given set of power exchange setpoints P_{PHEV1} and P_{PHEV2} , the linearized state-space model has been examined in terms of stability, and the boundary between the stable and unstable operating regions has been depicted in Fig. 7, when the PV system generates an aggregate power of 10 kW.

It is observed that the system becomes unstable if the power absorbed by the battery chargers exceed the levels marked by the boundary curve. The instability, in turn, prevents the battery chargers from operating at their full capacities and, consequently, results in under-utilization of the investment and prolongs the charging times.

To mitigate the aforementioned instability issue, a filtered version of the network-side voltage of each dc-dc converter is used to alter the power exchange setpoint of the converter, as illustrated in Fig. 3.8. Thus, the power exchange setpoint of the i^{th} dc-dc converter, P_{Bi}^* , is determined by the following nonlinear equations:

$$P_{Bi}^* = \left(\frac{v_i}{w_i} \right) P_{PHEVi}^* \quad (3.12)$$

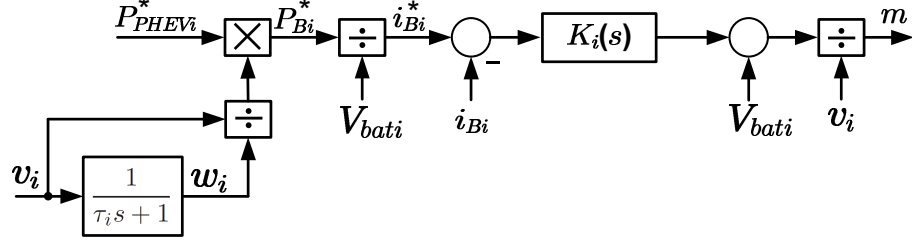


Figure 3.8: Modification of the power exchange setpoints of the dc-dc converters.

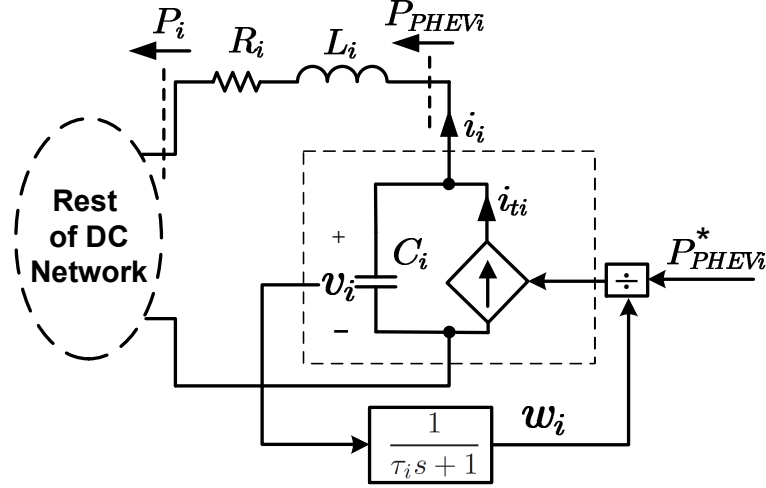


Figure 3.9: Simplified model of the modified dc-dc converter.

$$\frac{dw_i}{dt} = \frac{v_i - w_i}{\tau_i}, \quad (3.13)$$

where τ_i and w_i are the time constant and the filtered measure of the network-side dc voltage, v_i , respectively.

Fig. 3.9 shows a simplified model of the modified dc-dc converter.

The current that flows to the dc system, i_{ti} , can be found as

$$i_{ti} = \frac{1}{w_i} P_{PHEVi}^*. \quad (3.14)$$

As illustrated in Section 3.6, if τ_i is large compared to time scale of dynamics of interconnection cables in the dc network then the instability of the dc system can be avoided in all operating points of the system. The steady-state gain of the filter that converts v_i to w_i is unit, therefore, the modification of (3.12) will not change the steady-state operating point of the dc-dc converter. It should be pointed out that, as Fig. 3.10 shows, the proposed technique modifies the power exchange setpoints of the converters,

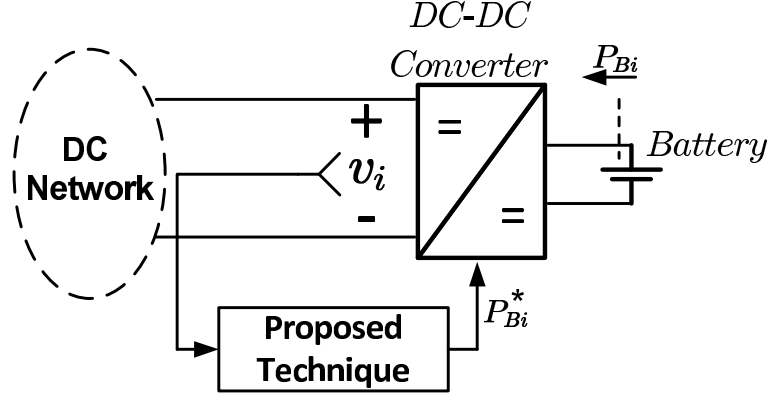


Figure 3.10: Connection block diagram for the proposed technique.

using local measurements. Thus, it does not require access to any variables internal to the converters, does not need hardware or software modifications, and can be exercised in a decentralized fashion. Therefore, it can be implemented using commercially available battery chargers.

By applying the proposed modification in Fig. 3.8 to the dc-dc converters of the system of Fig. 3.2, equations (3.8) through (3.10) are replaced by the following differential equations.

$$C_1 \frac{dv_1}{dt} = \frac{P_{PHEV1}^*}{w_1} - i_1, \quad (3.15)$$

$$\frac{dw_1}{dt} = \frac{v_1 - w_1}{\tau_1}, \quad (3.16)$$

$$C_2 \frac{dv_2}{dt} = \frac{P_{PHEV2}^*}{w_2} - i_2, \quad (3.17)$$

$$\frac{dw_2}{dt} = \frac{v_2 - w_2}{\tau_2}, \quad (3.18)$$

$$C_2 \frac{dv_3}{dt} = \frac{P_{PV,mppt}}{w_3} - i_3, \quad (3.19)$$

$$\frac{dw_3}{dt} = \frac{v_3 - w_3}{\tau_3}. \quad (3.20)$$

The linearized versions of (3.5) through (3.7), and (3.15) through (3.20) can be expressed in the state-space form as

$$\dot{\mathbf{x}}_{\text{mod}} = \mathbf{A}_{\text{mod}} \mathbf{x}_{\text{mod}}, \quad (3.21)$$

where $\mathbf{x}_{\text{mod}} = [\tilde{i}_1 \ \tilde{i}_2 \ \tilde{i}_3 \ \tilde{v}_1 \ \tilde{w}_1 \ \tilde{v}_2 \ \tilde{w}_2 \ \tilde{v}_3 \ \tilde{w}_3]^T$ is the new vector of state variables, and the

matrix \mathbf{A}_{mod} is introduced by (3.22) and (3.23); the uppercase letters denote the steady-state values of the state variables, which can be calculated by setting the derivatives to zero in equations (3.5) through (3.7), and (3.15) through (3.20).

$$\mathbf{A}_{\text{mod}} = \begin{bmatrix} \frac{RL_2L_3+R_1(LL_2+LL_3+L_2L_3)}{-den} & \frac{RL_2L_3-R_2LL_3}{-den} & \frac{RL_2L_3-R_3LL_2}{-den} \\ \frac{RL_1L_3-R_1LL_3}{-den} & \frac{RL_1L_3+R_2(LL_1+LL_3+L_1L_3)}{-den} & \frac{RL_1L_3-R_3LL_1}{-den} \\ \frac{RL_1L_2-R_1LL_2}{-den} & \frac{RL_1L_2-R_2LL_1}{-den} & \frac{RL_1L_2+R_3(LL_1+LL_2+L_1L_2)}{-den} \\ -\frac{1}{C_1} & 0 & 0 \\ 0 & 0 & 0 \\ 0 & -\frac{1}{C_2} & 0 \\ 0 & 0 & 0 \\ 0 & 0 & -\frac{1}{C_3} \\ 0 & 0 & 0 \end{bmatrix}$$

$$\begin{bmatrix} \frac{L(L_2+L_3)+L_2L_3}{den} & 0 & \frac{LL_3}{-den} & 0 & \frac{LL_2}{-den} & 0 \\ \frac{LL_3}{-den} & 0 & \frac{L(L_1+L_3)+L_1L_3}{den} & 0 & \frac{LL_1}{-den} & 0 \\ \frac{LL_2}{-den} & 0 & \frac{LL_1}{-den} & 0 & \frac{L(L_1+L_2)+L_1L_2}{den} & 0 \\ 0 & -\frac{P_{PHEV1}^*}{V_1^2C_1} & 0 & 0 & 0 & 0 \\ \frac{1}{\tau_1} & -\frac{1}{\tau_1} & 0 & 0 & 0 & 0 \\ 0 & 0 & 0 & -\frac{P_{PHEV2}^*}{V_2^2C_2} & 0 & 0 \\ 0 & 0 & \frac{1}{\tau_2} & -\frac{1}{\tau_2} & 0 & 0 \\ 0 & 0 & 0 & 0 & 0 & -\frac{P_{PV,mppt}}{V_3^2C_3} \\ 0 & 0 & 0 & 0 & \frac{1}{\tau_3} & -\frac{1}{\tau_3} \end{bmatrix} \quad (3.22)$$

$$den = LL_1L_2 + LL_1L_3 + LL_2L_3 + L_1L_2L_3. \quad (3.23)$$

Stability of the modified system has been checked for the study system in Matlab software environment. Fig. 3.11 shows the boundaries between the stable and unstable operating regions for different values of τ_i . In this case, the PV system is generating a power of 10 kW and power consumption of PHEVs are variable. Fig. 3.11 depicts that if the values of τ_i increase then the stable operating region of the dc system expands. This agrees with the analysis presented in Section 3.6.

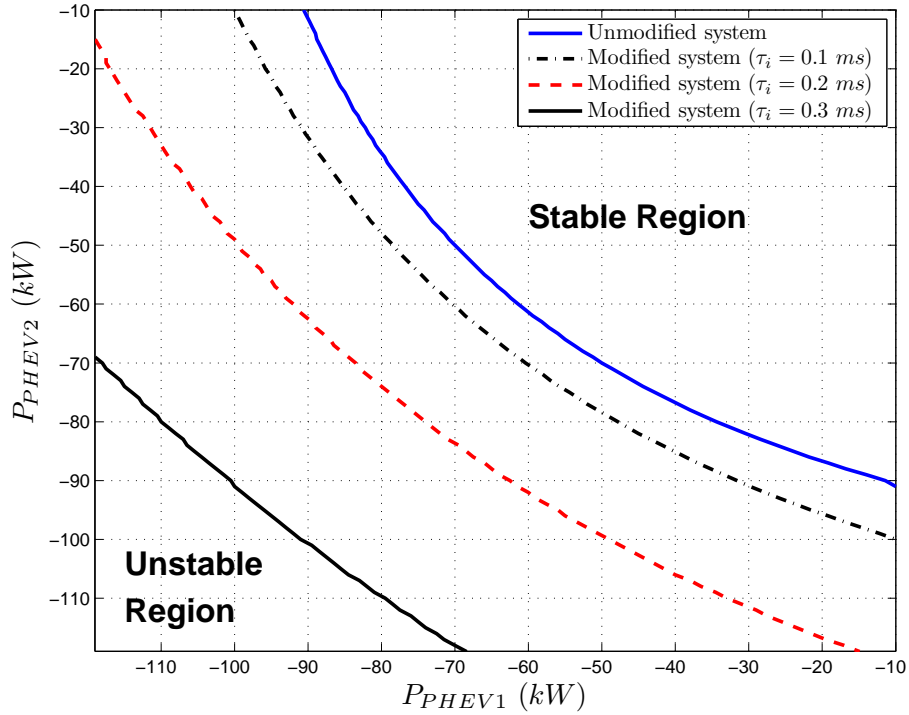


Figure 3.11: Boundaries between stable and unstable regions for unmodified and modified systems with different values of τ_i .

It should be noted that an increase in the PV power generation slightly expands the stable region, as Fig. 3.12 indicates. However, the improving effect of an increased PV power generation is insignificant compared to the effect of the time constant in the proposed modification. Moreover, PV power generation is not deterministic and, therefore, one cannot rely on it to enhance the stability.

3.5 Simulation Results

The study system was simulated in the PSCAD/EMTDC software environment. Fig. 3.13 and Fig. 3.14 demonstrate the performance of the dc system in the normal conditions when the steady-state operating point lies inside the stable region.

Initially, the system is in a steady state and, as Fig. 3.13 shows, the controlled dc-voltage power port regulates v_{dc} at 480 V. At $t = 0.5$ s, the PV system starts to generate a power of 20 kW. At $t = 0.6$ s, the batteries in PHEV2 start to absorb a power of 20 kW, as indicated by P_{PHEV2}^* , and at $t = 0.7$ s, the batteries in PHEV1 start to charge with a power of 30 kW, as indicated by P_{PHEV1}^* . Therefore, in a steady state, a power of

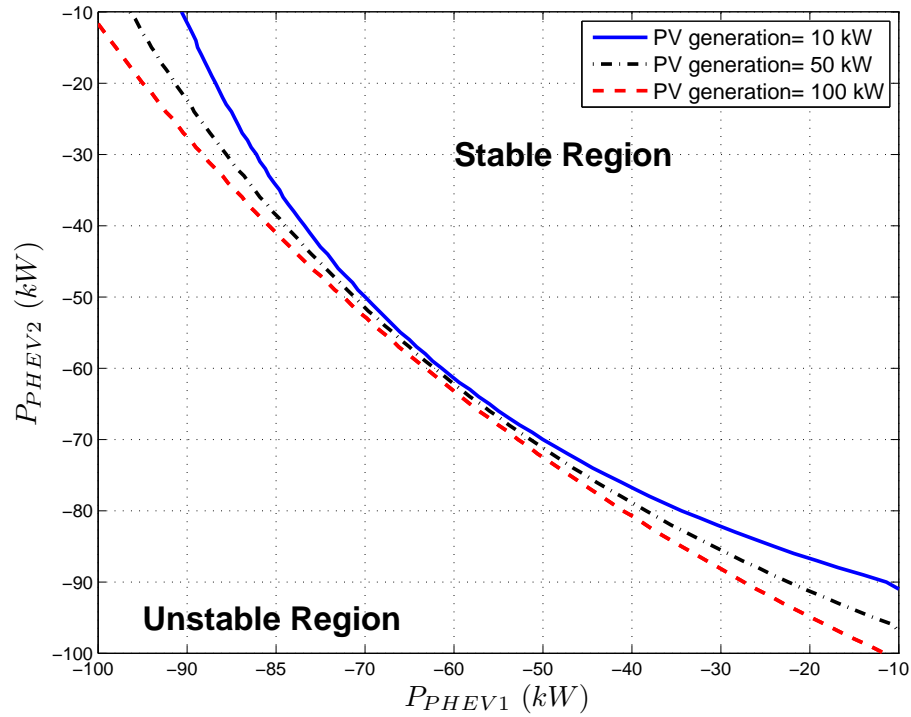


Figure 3.12: Boundaries between stable and unstable regions for different values of power generation of PV modules.

about 30 kW flows from the ac power grid to the dc system. As Fig. 3.13 illustrates, the dc system remains stable under the aforementioned sequence of events and the central VSC regulates the v_{dc} at 480 V.

Fig. 3.14 shows the system performance for a case where the power flow is from the dc system towards the ac power grid. The PV system starts to generate a power of 20 kW at $t = 0.5$ s, as Fig. 3.14 shows. At $t = 0.6$ s, the batteries in PHEV2 start to consume a power of 20 kW that compensates the PV system generation so no power flows to the ac power grid. At $t = 0.7$ s, the batteries in PHEV1 start to generate 30 kW, as indicated by P_{PHEV1}^* in Fig. 3.14. Consequently, in a steady state, a power of around 30 kW flows from the dc system to the ac power grid. The dc system remains stable and v_{dc} is regulated at 480 V for all of the aforementioned disturbances.

Fig. 3.15 and Fig. 3.16 demonstrate the effectiveness of the proposed modification to enhance the stability of the dc distribution system. Performance of the system has been analyzed in two working scenarios. In the first scenario, as Fig. 3.15 shows, the system is working at an operating point where the power consumptions of PHEV1 and PHEV2 are 60 kW and 50 kW, respectively, and the PV system generates a power

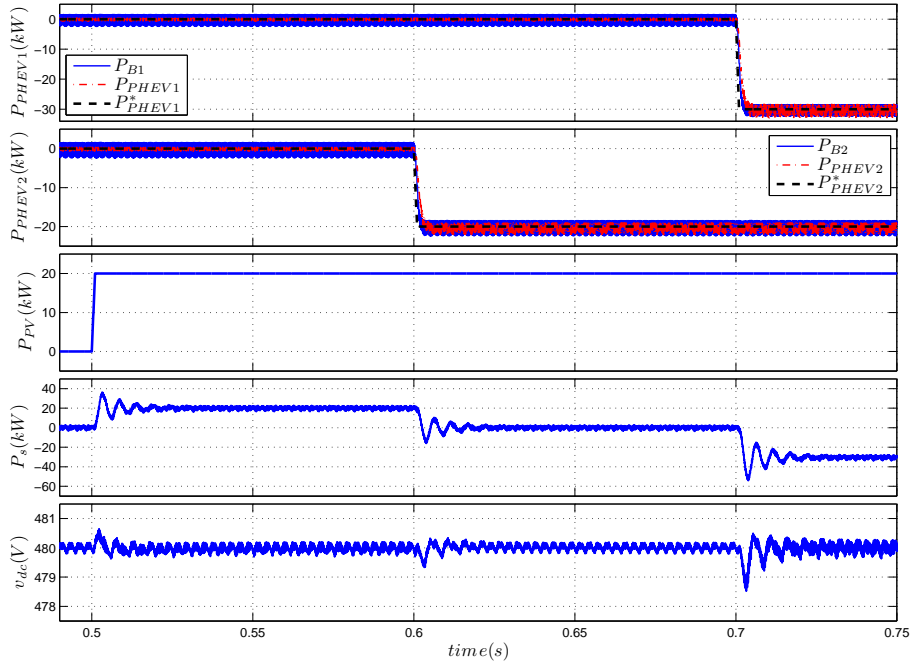


Figure 3.13: The dc system response when the power flows from the ac power grid to the dc system.

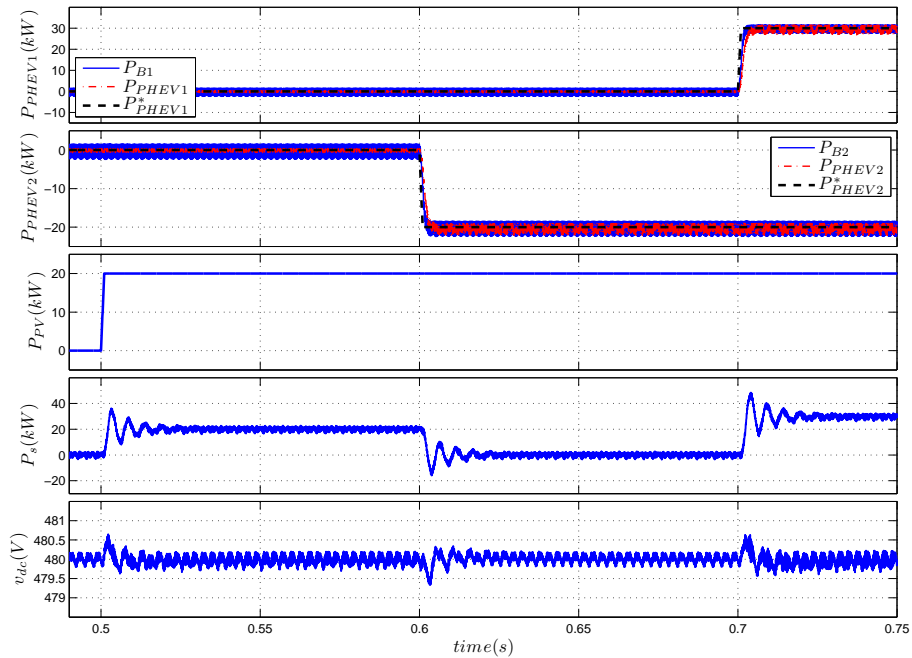


Figure 3.14: The dc system response when the power flows from the dc system to the ac power grid.

of 10 kW. Based on Fig. 3.11, this operating point situates at the verge of instability for the unmodified dc system. Thus, a change in the power consumption of PHEV1, at

$t = 1.3$ s, from 60 kW to 77 kW, leads to instability for the unmodified dc system while for the modified dc systems with both $\tau_i = 0.1$ ms, $\tau_i = 0.2$ ms, and $\tau_i = 2$ ms, the systems remain stable and converge to the new setpoints. The instability first occurs to P_1 , P_2 , and P_3 , while the dc-dc converters try to keep the power levels of PHEV1 and PHEV2 constant at their setpoints. The central VSC keeps the dc voltage, v_{dc} , constant.

In the second scenario, as Fig. 3.16 shows, the system works at another operating point where the power consumptions of PHEV1 and PHEV2 are 60 kW and 50 kW, respectively, and the PV system generates 10 kW. A change in the power consumption of PHEV1, at $t = 1.3$ s, from 60 kW to 85 kW, moves the operating point outside of the stable region for the unmodified dc system and the modified dc system with $\tau_i = 0.3$ ms, as predicted in Fig 3.11. Fig. 3.16 shows that this transition destabilizes both the unmodified dc system and the modified dc system with $\tau_i = 0.1$ ms, whereas the modified dc-dc converters with $\tau_i = 0.2$ ms and $\tau_i = 2$ ms remains stable and converge to the new setpoints. The instabilities in this case also first occur to P_1 , P_2 , and P_3 . Figs. 3.15 and 3.16 show that, the response settles more rapidly at its post-disturbance value as the the time constant τ_i is increased.

Fig. 3.15(a) and Fig. 3.16(a)(b) might give the impression that the instability does not have any impact on the dc voltage. However, this is not the reality and is due to the fact that the simulation results in Fig. 3.15 and Fig. 3.16 have been shown for a relatively short period of time, for the sake of clarity of the waveforms; the growth of oscillations becomes more obvious if one shows the waveforms over a longer time slot. Fig. 3.17 presents long-run simulations for both scenarios. As depicted in the figure, in both scenarios the dc voltage starts to oscillate and eventually crashes due to the instability of the dc system. However, in the first scenario, the oscillations start after a longer time, compared to the second scenario, due to the larger distance of its operating point relative to the borderline between the stable and unstable regions.

3.6 Stability Enhancement for a dc System with Single dc-dc Converter

Fig. 3.18 illustrates the application of the proposed modification to a circuit consisting of a dc voltage source, an interconnection line, and a constant-power element. In the circuit of Fig. 3.18, E represents the source voltage, L and R respectively signify the line inductance and resistance, and C denotes the line-side terminal capacitance of the

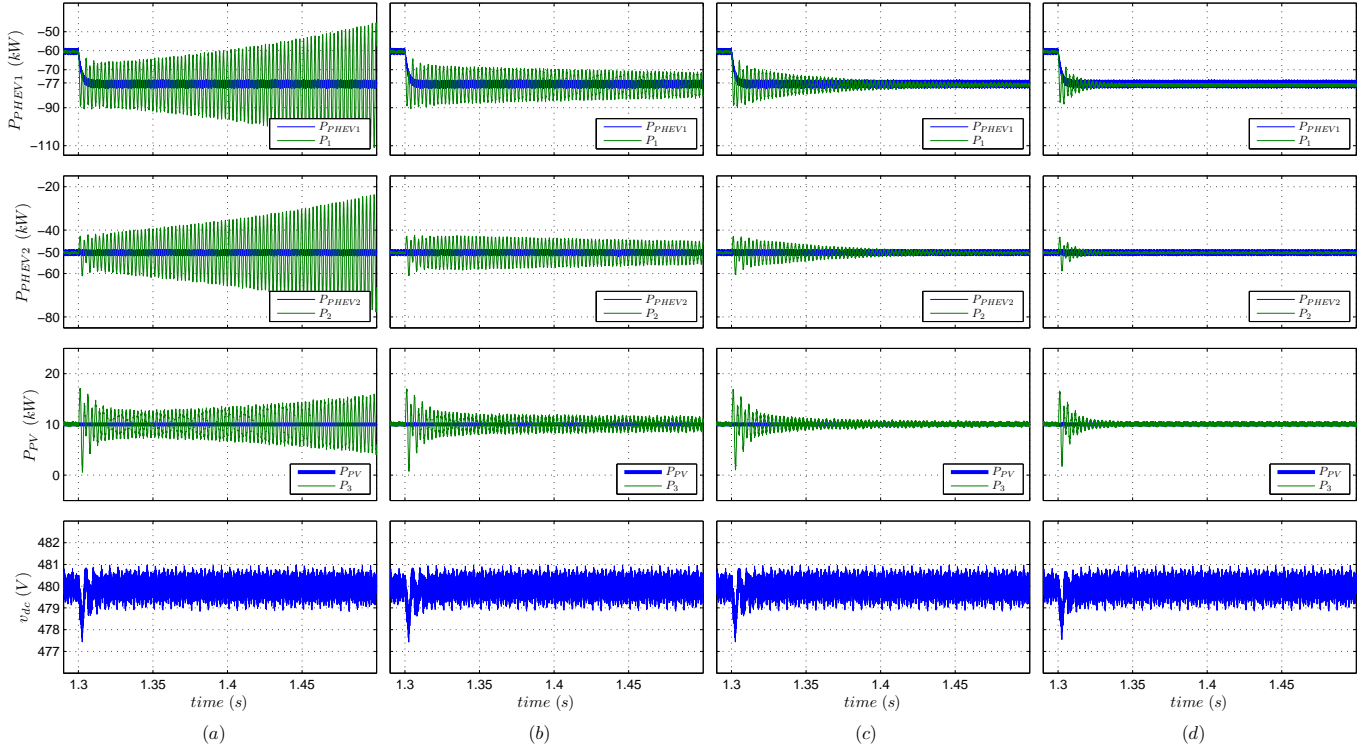


Figure 3.15: Responses of the dc system in the first scenario; (a) the unmodified dc system (b) the modified dc system with $\tau_i = 0.1 \text{ ms}$, (c) the modified dc system with $\tau_i = 0.2 \text{ ms}$, (d) the modified dc system with $\tau_i = 2 \text{ ms}$.

constant-power element.

The dynamics of the circuit of Fig. 3.18 are governed by the following differential equations

$$L \frac{di}{dt} = -Ri + v - E, \quad (3.24)$$

$$\tau \frac{dw}{dt} = v - w, \quad (3.25)$$

$$C \frac{dv}{dt} = -i + \frac{P^*}{w}. \quad (3.26)$$

It can be shown that the existence condition for steady-state operating point of the system is

$$P^* \geq -\frac{E^2}{4R}. \quad (3.27)$$

It also can be shown that the steady-state voltage of the constant-power element, V , is

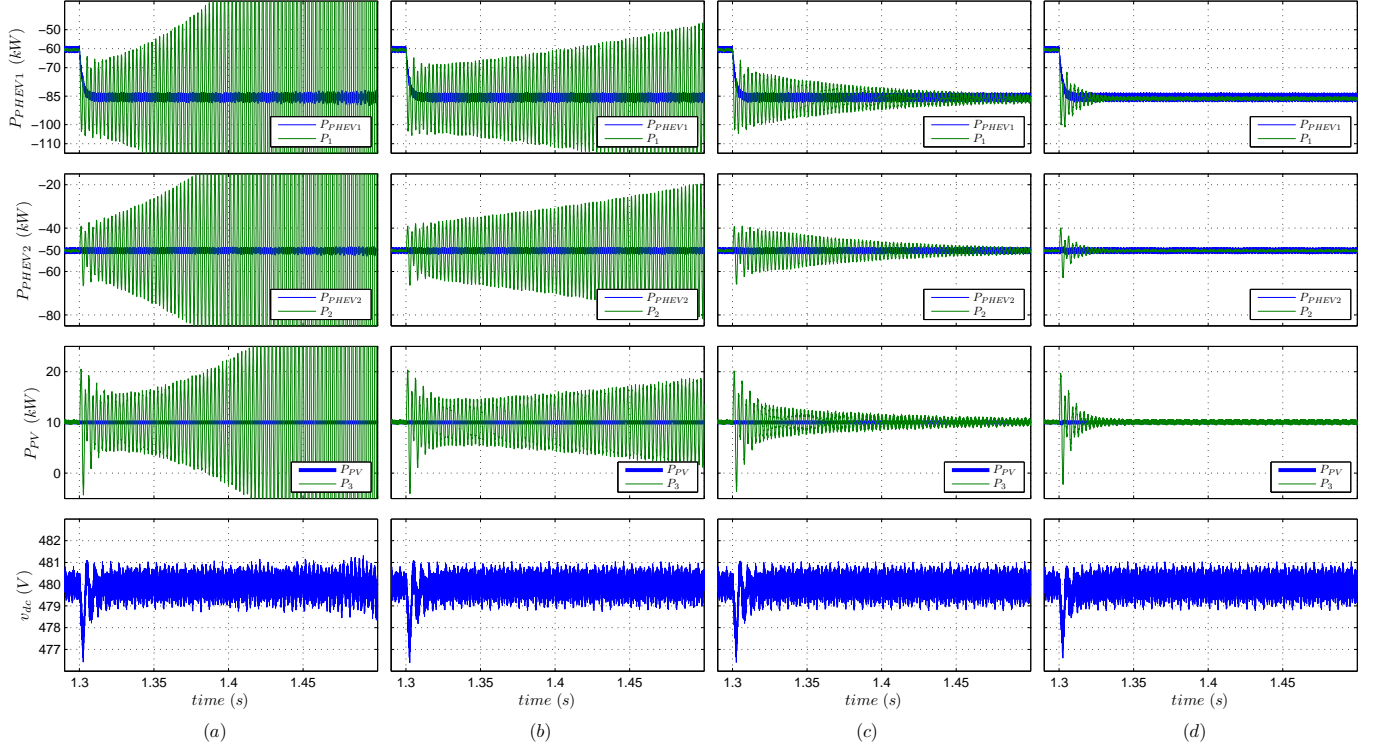


Figure 3.16: Responses of the dc system in the second scenario; (a) the unmodified dc system (b) the modified dc system with $\tau_i = 0.1 \text{ ms}$, (c) the modified dc system with $\tau_i = 0.2 \text{ ms}$, (d) the modified dc system with $\tau_i = 2 \text{ ms}$.

always greater than half of dc voltage source, E , for all operating points

$$V \geq \frac{E}{2}. \quad (3.28)$$

The linearized form of (3.26) is

$$C \frac{d\tilde{v}}{dt} = -\tilde{i} - \frac{P^*}{V^2} \tilde{w}. \quad (3.29)$$

The eigenvalues of the linearized system can be found by solving the following characteristic equation

$$LC\tau\lambda^3 + (LC + RC\tau)\lambda^2 + \left(\frac{P^*}{V^2}L + RC + \tau\right)\lambda + \frac{P^*}{V^2}R + 1 = 0. \quad (3.30)$$

Based on Routh-Horwitz stability test, the system is stable if and only if

$$P^* > -\frac{V^2}{R}, \quad (3.31)$$

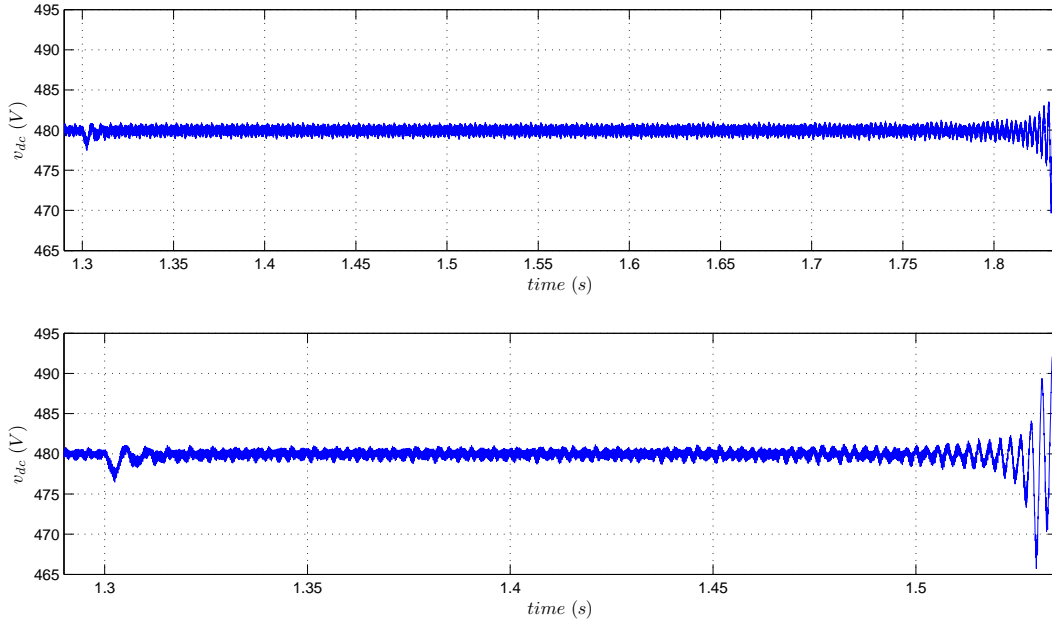


Figure 3.17: Long-run simulations for v_{dc} ; the first unstable scenario for instability (top), the second unstable scenario for instability (bottom).

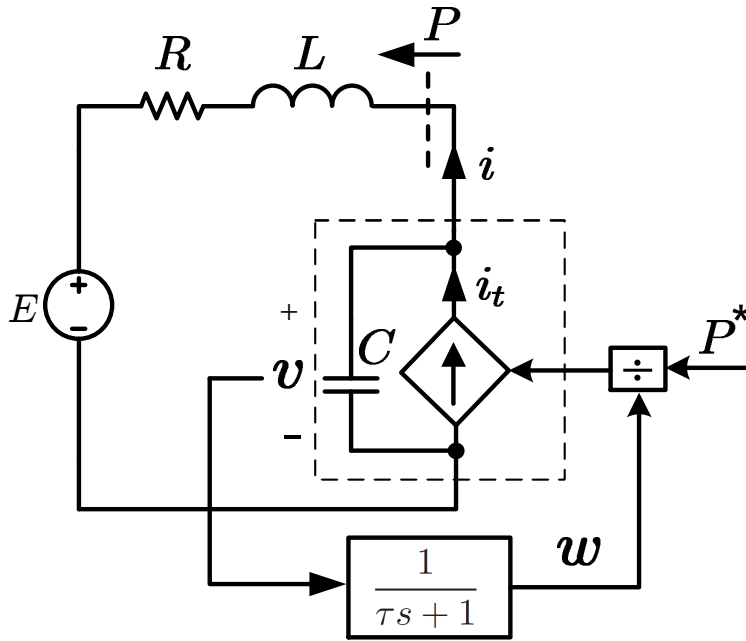


Figure 3.18: Proposed modification on a single constant-power element.

and

$$P^* > -\frac{RCV^2}{L} - \frac{\tau V^2}{L}, \tag{3.32}$$

and

$$(LC + RC\tau) \left(\frac{P^*}{V^2}L + RC + \tau \right) > LC\tau \left(1 + \frac{P^*}{V^2}R \right). \quad (3.33)$$

Considering (3.27) and (3.28), inequality (3.31) is always true for all operating points of the system. If τ is chosen as

$$\tau > \frac{L}{R} - RC, \quad (3.34)$$

then one can write

$$-\frac{1}{R} > -\frac{RC}{L} - \frac{\tau}{L}. \quad (3.35)$$

Multiplying both sides of (3.35) by V^2 , one obtains

$$-\frac{V^2}{R} > -\frac{RCV^2}{L} - \frac{\tau V^2}{L}. \quad (3.36)$$

Comparing (3.31) and (3.36), one can conclude that by choosing τ as (3.34), the inequality (3.32) is true for all operating points of the system.

Inequality (3.33) can be rewritten as

$$LC \left(\frac{P^*}{V^2}L + RC + \tau \right) + RC\tau \left(\frac{P^*}{V^2}L + RC + \tau \right) > LC\tau \left(1 + \frac{P^*}{V^2}R \right). \quad (3.37)$$

First, let focus on the second term of the left hand side of (3.37) and its relation to the right hand side of (3.37). Choosing τ as (3.34) one can write

$$RC + \tau > \frac{L}{R}. \quad (3.38)$$

Adding $\frac{P^*}{V^2}L$ to both side of (3.38), one obtains

$$RC + \tau + \frac{P^*}{V^2}L > \frac{L}{R} + \frac{P^*}{V^2}L. \quad (3.39)$$

Inequality (3.39) can be rewritten as

$$R \left(RC + \tau + \frac{P^*}{V^2}L \right) > L \left(1 + \frac{P^*}{V^2}R \right) \quad (3.40)$$

or

$$RC\tau \left(RC + \tau + \frac{P^*}{V^2}L \right) > LC\tau \left(1 + \frac{P^*}{V^2}R \right). \quad (3.41)$$

Inequality (3.41) indicates that if τ is chosen as (3.34) then the second term of left hand

side of (3.37) is always greater than the left hand side of (3.37).

On the other hand, we already know that if τ is chosen as (3.34) then (3.32) is true. Therefore, one can write

$$LC \left(\frac{P^*}{V^2} L + RC + \tau \right) > 0. \quad (3.42)$$

Combining (3.41) and (3.42), one can conclude that (3.37) always holds, and therefore, the system is always stable in its operating point range. This means that by choosing a proper value for τ , based on parameters of the dc line, the proposed modification stabilizes the dc system with the constant-power element.

As inequality (3.34) indicates, a dc system with larger network-side dc-dc converter capacitances and/or smaller interconnection cable L/R ratios requires smaller values for the time constant τ_i to ensure stability. In the other words, larger network-side capacitances and smaller cable L/R ratios have stabilizing effects on the dc system.

3.7 Stability Enhancement for a dc System with n dc-dc Converters

Fig. 3.19 illustrates the application of the proposed modification to a dc system with n dc-dc converters for n PHEVs. Applying the same approach as of Section 2.3.2, one can develop a state-space model for the modified system of Fig. 3.19 as the following:

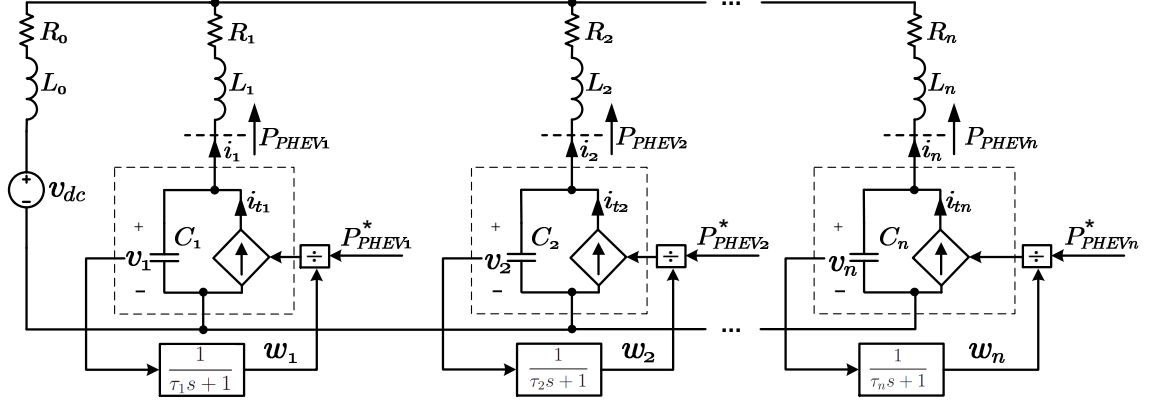
$$\dot{\mathbf{x}}_{\text{new}} = \mathbf{A}_{\text{new}} \mathbf{x}_{\text{new}}, \quad (3.43)$$

where

$$\mathbf{x}_{\text{new}} = \begin{bmatrix} \tilde{\mathbf{i}} \\ \tilde{\mathbf{v}} \\ \tilde{\mathbf{w}} \end{bmatrix}_{3n \times 1}, \quad \tilde{\mathbf{i}} = \begin{bmatrix} \tilde{i}_1 \\ \vdots \\ \tilde{i}_n \end{bmatrix}, \quad \tilde{\mathbf{v}} = \begin{bmatrix} \tilde{v}_1 \\ \vdots \\ \tilde{v}_n \end{bmatrix}, \quad \tilde{\mathbf{w}} = \begin{bmatrix} \tilde{w}_1 \\ \vdots \\ \tilde{w}_n \end{bmatrix}. \quad (3.44)$$

Matrix \mathbf{A} can be expressed as

$$\mathbf{A}_{\text{new}} = \begin{bmatrix} -\mathbf{L}^{-1}\mathbf{R} & \mathbf{L}^{-1} & \mathbf{0}_{n \times n} \\ -\mathbf{C}^{-1} & \mathbf{0}_{n \times n} & -\mathbf{C}^{-1}\mathbf{P} \\ \mathbf{0}_{n \times n} & \boldsymbol{\tau}^{-1} & -\boldsymbol{\tau}^{-1} \end{bmatrix}_{3n \times 3n} \quad (3.45)$$

Figure 3.19: Proposed modification on a dc system with n dc-dc converters.

where

$$\boldsymbol{\tau} = \begin{bmatrix} \tau_1 & 0 & \cdots & 0 \\ 0 & \tau_2 & \cdots & 0 \\ \vdots & \vdots & \ddots & \vdots \\ 0 & 0 & \cdots & \tau_n \end{bmatrix}, \quad (3.46)$$

and

$$\mathbf{L} = \begin{bmatrix} L_0 + L_1 & L_0 & \cdots & L_0 \\ L_0 & L_0 + L_2 & \cdots & L_0 \\ \vdots & \vdots & \ddots & \vdots \\ L_0 & L_0 & \cdots & L_0 + L_n \end{bmatrix}, \quad \mathbf{R} = \begin{bmatrix} R_0 + R_1 & R_0 & \cdots & R_0 \\ R_0 & R_0 + R_2 & \cdots & R_0 \\ \vdots & \vdots & \ddots & \vdots \\ R_0 & R_0 & \cdots & R_0 + R_n \end{bmatrix} \quad (3.47)$$

$$\mathbf{C} = \begin{bmatrix} C_1 & 0 & \cdots & 0 \\ 0 & C_2 & \cdots & 0 \\ \vdots & \vdots & \ddots & \vdots \\ 0 & 0 & \cdots & C_n \end{bmatrix}, \quad \mathbf{P} = \begin{bmatrix} \frac{P_{PHEV1}^*}{V_1^2} & 0 & \cdots & 0 \\ 0 & \frac{P_{PHEV2}^*}{V_2^2} & \cdots & 0 \\ \vdots & \vdots & \ddots & \vdots \\ 0 & 0 & \cdots & \frac{P_{PHEVn}^*}{V_n^2} \end{bmatrix}. \quad (3.48)$$

Similar to (2.33), \mathbf{A}_{new} can be rewritten as

$$\mathbf{A}_{\text{new}} = \begin{bmatrix} -\mathbf{L}^{-1} & \mathbf{0}_{n \times n} & \mathbf{0}_{n \times n} \\ \mathbf{0}_{n \times n} & -\mathbf{C}^{-1} & \mathbf{0}_{n \times n} \\ \mathbf{0}_{n \times n} & \mathbf{0}_{n \times n} & -\boldsymbol{\tau}^{-1} \end{bmatrix} \begin{bmatrix} \mathbf{R} & -\mathbf{I}_{n \times n} & \mathbf{0}_{n \times n} \\ \mathbf{I}_{n \times n} & \mathbf{0}_{n \times n} & \mathbf{P} \\ \mathbf{0}_{n \times n} & -\mathbf{I}_{n \times n} & \mathbf{I}_{n \times n} \end{bmatrix} = \mathbf{N}_{\text{new}}^{-1} \mathbf{M}_{\text{new}} \quad (3.49)$$

where

$$\mathbf{N}_{\text{new}} = \begin{bmatrix} -\mathbf{L} & \mathbf{0}_{n \times n} & \mathbf{0}_{n \times n} \\ \mathbf{0}_{n \times n} & -\mathbf{C} & \mathbf{0}_{n \times n} \\ \mathbf{0}_{n \times n} & \mathbf{0}_{n \times n} & -\tau \end{bmatrix}, \quad \mathbf{M}_{\text{new}} = \begin{bmatrix} \mathbf{R} & -\mathbf{I}_{n \times n} & \mathbf{0}_{n \times n} \\ \mathbf{I}_{n \times n} & \mathbf{0}_{n \times n} & \mathbf{P} \\ \mathbf{0}_{n \times n} & -\mathbf{I}_{n \times n} & \mathbf{I}_{n \times n} \end{bmatrix}. \quad (3.50)$$

Assuming $\{\tau_i > 0, i = 1, 2, \dots, n\}$, \mathbf{N}_{new} is a symmetric, negative-definite (and, therefore, non-singular) matrix.

For stability analysis, one must evaluate the eigenvalues of \mathbf{A}_{new} in (3.43). Let λ be an eigenvalue of \mathbf{A}_{new} . Then one can write

$$\mathbf{A}\mathbf{u} = \lambda\mathbf{u}, \quad \mathbf{u} \neq \mathbf{0}, \quad (3.51)$$

where \mathbf{u} is an eigenvector of \mathbf{A}_{new} , associated with λ . Substituting for \mathbf{A}_{new} in (3.51) from (3.49), one finds

$$\mathbf{N}_{\text{new}}^{-1}\mathbf{M}_{\text{new}}\mathbf{u} = \lambda\mathbf{u}. \quad (3.52)$$

Pre-multiplying (3.52) by \mathbf{N}_{new} , one obtains

$$\mathbf{M}_{\text{new}}\mathbf{u} = \lambda\mathbf{N}_{\text{new}}\mathbf{u}, \quad (3.53)$$

Equation (3.53) can be rewritten as

$$(\mathbf{M}_{\text{new}} - \lambda\mathbf{N}_{\text{new}})\mathbf{u} = \mathbf{0}, \quad \mathbf{u} \neq \mathbf{0}. \quad (3.54)$$

Substituting for \mathbf{M}_{new} and \mathbf{N}_{new} from (3.50) in (3.54), one can arrive at the following expression for the determinant of $\mathbf{M}_{\text{new}} - \lambda\mathbf{N}_{\text{new}}$, which, in turn, is the characteristic equation associated with (3.43):

$$\begin{vmatrix} \mathbf{R} + \lambda\mathbf{L} & -\mathbf{I}_{n \times n} & \mathbf{0}_{n \times n} \\ \mathbf{I}_{n \times n} & \lambda\mathbf{C} & \mathbf{P} \\ \mathbf{0}_{n \times n} & -\mathbf{I}_{n \times n} & \mathbf{I}_{n \times n} + \lambda\tau \end{vmatrix} = 0, \quad (3.55)$$

which can be rewritten as

$$|\mathbf{I}_{n \times n} + \lambda\tau| \det \left(\begin{bmatrix} \mathbf{R} + \lambda\mathbf{L} & -\mathbf{I}_{n \times n} \\ \mathbf{I}_{n \times n} & \lambda\mathbf{C} \end{bmatrix} - \begin{bmatrix} \mathbf{0}_{n \times n} \\ \mathbf{P} \end{bmatrix} \Gamma_{n \times n} \begin{bmatrix} \mathbf{0}_{n \times n} & -\mathbf{I}_{n \times n} \end{bmatrix} \right) = 0 \quad (3.56)$$

or

$$\left| \mathbf{I}_{n \times n} + \lambda \boldsymbol{\tau} \right| \begin{vmatrix} \mathbf{R} + \lambda \mathbf{L} & -\mathbf{I}_{n \times n} \\ \mathbf{I}_{n \times n} & \lambda \mathbf{C} + \mathbf{P}\boldsymbol{\Gamma} \end{vmatrix} = 0 \quad (3.57)$$

where

$$\begin{aligned} \boldsymbol{\Gamma}_{n \times n} &= (\mathbf{I}_{n \times n} + \lambda \boldsymbol{\tau})^{-1} \\ &= \begin{bmatrix} \frac{1}{1+\lambda\tau_1} & 0 & \cdots & 0 \\ 0 & \frac{1}{1+\lambda\tau_2} & \cdots & 0 \\ \vdots & \vdots & \ddots & \vdots \\ 0 & 0 & \cdots & \frac{1}{1+\lambda\tau_n} \end{bmatrix}. \end{aligned} \quad (3.58)$$

It can be shown that (3.57) is equivalent to

$$\left| \mathbf{I}_{n \times n} + \lambda \boldsymbol{\tau} \right| \begin{vmatrix} \alpha_{new_1} + \beta_{new_1} & \alpha_{new_2} & \cdots & \alpha_{new_n} \\ \alpha_{new_1} & \alpha_{new_2} + \beta_{new_2} & \cdots & \alpha_{new_n} \\ \vdots & \vdots & \ddots & \vdots \\ \alpha_{new_1} & \alpha_{new_2} & \cdots & \alpha_{new_n} + \beta_{new_n} \end{vmatrix} \begin{vmatrix} \frac{1}{1+\lambda\tau_1} & 0 & \cdots & 0 \\ 0 & \frac{1}{1+\lambda\tau_2} & \cdots & 0 \\ \vdots & \vdots & \ddots & \vdots \\ 0 & 0 & \cdots & \frac{1}{1+\lambda\tau_n} \end{vmatrix} = 0 \quad (3.59)$$

where

$$\alpha_{new_i} = L_0 C_i \tau_i \lambda^3 + (L_0 C_i + R_0 C_i \tau_i) \lambda^2 + \left(R_0 C_i + L_0 \frac{P_{PHEV_i}}{V_i^2} \right) \lambda + R_0 \frac{P_{PHEV_i}}{V_i^2} \quad (3.60)$$

and

$$\beta_{new_i} = L_i C_i \tau_i \lambda^3 + (L_i C_i + R_i C_i \tau_i) \lambda^2 + \left(R_i C_i + L_i \frac{P_{PHEV_i}}{V_i^2} + \tau_i \right) \lambda + R_i \frac{P_{PHEV_i}}{V_i^2} + 1. \quad (3.61)$$

Equation (3.59) can be rewritten as

$$\begin{vmatrix} \alpha_{new_1} + \beta_{new_1} & \alpha_{new_2} & \cdots & \alpha_{new_n} \\ \alpha_{new_1} & \alpha_{new_2} + \beta_{new_2} & \cdots & \alpha_{new_n} \\ \vdots & \vdots & \ddots & \vdots \\ \alpha_{new_1} & \alpha_{new_2} & \cdots & \alpha_{new_n} + \beta_{new_n} \end{vmatrix} = 0. \quad (3.62)$$

It can then be shown (see Appendix C) that (3.62) is equivalent to the 3nth-order poly-

nomial equation

$$\prod_{i=1}^n \beta_{new_i} + \sum_{i=1}^n (\alpha_{new_i} \prod_{\substack{k=1 \\ k \neq i}}^n \beta_{new_k}) = 0, \quad (3.63)$$

which is remarkably easier to solve, from a computational burden standpoint, relative to a direct calculation of the eigenvalues of \mathbf{A}_{new} (i.e., using matrix operations); this facilitates physical implementation of the method on an embedded signal-processing platform.

In a special case, let R_0 and L_0 be zero. Then α_{new_i} , ($i = 1, 2, \dots, n$) are zero and, therefore, (3.63) takes the form

$$\prod_{i=1}^n \beta_{new_i} = 0 \quad (3.64)$$

or

$$\prod_{i=1}^n \left[L_i C_i \tau_i \lambda^3 + (L_i C_i + R_i C_i \tau_i) \lambda^2 + \left(R_i C_i + L_i \frac{P_{PHEV_i}}{V_i^2} + \tau_i \right) \lambda + R_i \frac{P_{PHEV_i}}{V_i^2} + 1 \right] = 0. \quad (3.65)$$

Equation (3.65) implies that the special case corresponds to a dc system that consists of n independently energized dc-dc converters and the characteristic equation of the system is similar to (3.30), and, therefore, with a similar analysis that is presented in Section 3.6, one can conclude that the system is stable, in its operating range, if

$$\tau_i > \frac{L_i}{R_i} - R_i C_i \quad (i = 1, 2, \dots, n). \quad (3.66)$$

3.8 Conclusion

A method was proposed for enhancing the stability of a dc distribution system intended to integrate PHEVs with an ac power grid. The dc distribution system is interfaced with the host ac grid via a VSC and can also embed PV modules. Thus, bidirectional dc-dc power-electronic converters act as battery chargers and interface the PHEVs with the dc distribution system, while PV modules are interfaced with the dc distribution system via unidirectional dc-dc converters. It was demonstrated the proposed stability enhancement method mitigates the issue of instability by altering the power setpoints of the battery chargers, without a need for changing system parameters or hardware. The chapter presented mathematical models for the original and modified systems and demonstrated that the proposed technique expands the stable operating region of the dc distribution sys-

tem. Simulation studies were conducted to demonstrate the effectiveness of the proposed method for a study system in the PSCAD/EMTDC software environment.

Chapter 4

Energy Management Strategy

4.1 Introduction

Charging strategies of the plug-in electric vehicles (PEVs) have attracted much research recently [7,24,43,46–49]. The increasing number of PEVs is expected to adversely impact the power system and, therefore, suitable infrastructure and smart charging strategies are required to circumvent or mitigate those impacts [6]. The dc distribution systems have recently been perceived as the potential infrastructure for power system integration of PEVs [17–20,26,62], and they are expected to be beneficial both economically and technically [20]. A management unit in the dc distribution system dictates a battery charging (and discharging) strategy via a dedicated communications network.

Several recent reported studies have proposed charging strategies for PEVs. Reference [24] proposes algorithms for optimizing the PEV charging schedule from the owner’s perspective. A real-time smart load management control strategy is proposed in [7] to coordinate the charging of PEV, to minimize the power loss and the charging cost, and to mitigate the voltage fluctuations at the host ac grid. A strategy is proposed in [43] to mitigate the adverse impacts that uncontrolled charging of the PEVs impose on the host power system. Reference [46] proposes charging control strategies for a battery swapping station, where the PEV owners can quickly swap their depleted batteries with previously charged batteries. In [47], optimal scheduling has been proposed for both charging and discharging of the PEVs. The references cited above do not necessarily concern dc systems. However, they all assume an integral entity, an aggregator, that negotiates with the PEVs, in one hand, and with the host power system in the other hand. Hence, the host ac grid, deals with only one entity, the aggregator, rather than a

large number of PEVs.

In the majority of the reported studies, the proposed strategies aim to only optimize the charging costs for the PEV owners, or minimize the power loss within the system, but do not offer to the owners an option for fast battery charging (by which the charging time is minimized rather than the charging cost). Further, the reported studies commonly assume that the PEV owners fully comply with the (proposed) charging strategies, i.e., they connect their vehicles to the chargers, for the entire specified period, and do not depart early. In practice, however, an owner may decide to leave before the planned period has elapsed. Most of the reported studies also assume a unidirectional power flow, that is, into the PEVs, whereas there is a possibility for bidirectional power exchange among the PEVs and the host ac grid.

To address the aforementioned shortcomings, this chapter proposes an energy management strategy (EMS) that

- offers both fast and optimal energy exchange options to the PEV owners;
- operates seamlessly for both charging and discharging modes of operation;
- takes into account the likelihood of early departure of the PEVs;
- runs online and, therefore, can be readily implemented in an embedded processing platform;
- allows for variable-length energy exchange intervals to enhance the flexibility of the energy exchange transactions;
- and regulates both power consumption and generation of the PEVs within the dc system to circumvent adverse impacts on the host ac grid.

The proposed EMS is implemented in the management unit of a dc distribution system for power system integration of PEVs. The dc distribution system is assumed to be used in the parking lots to integrate electric vehicles with a host ac grid.

4.2 DC distribution System

Fig. 4.1 illustrates a conceptual diagram of a dc distribution system for integration of plug-in electric vehicles with an ac grid. The dc distribution system, referred hereafter

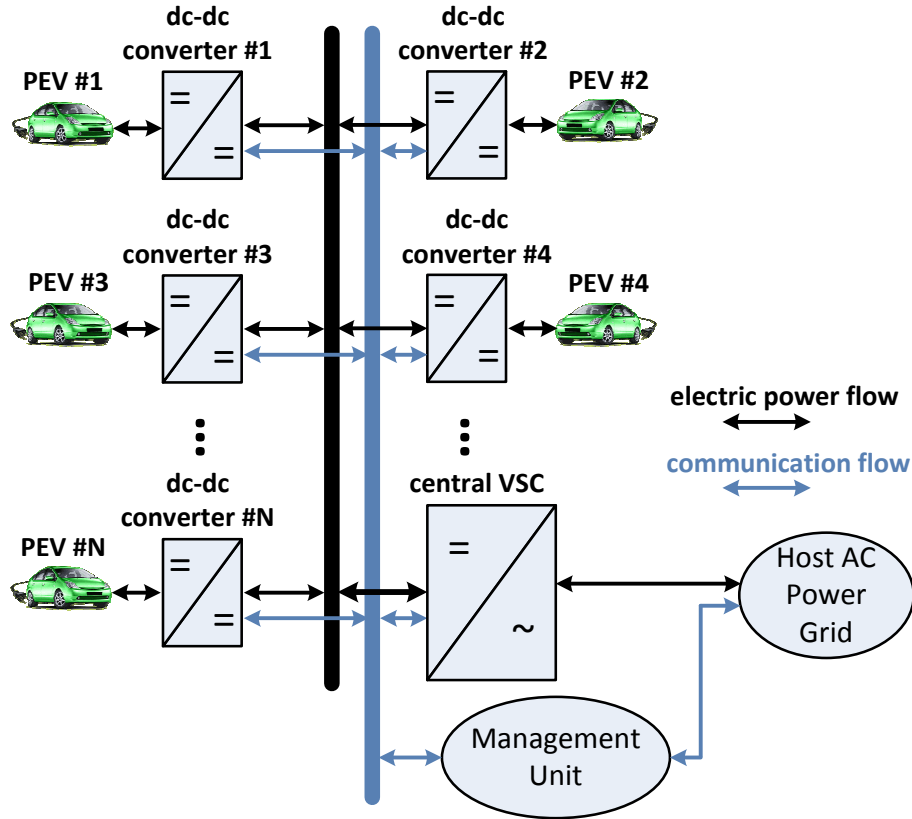


Figure 4.1: A dc distribution system (the dc system) for power system integration of electric vehicles.

to as the dc system, consists of a network of interconnection cables, a central voltage-sourced converter (VSC), a management unit, and a multitude of bidirectional dc-dc converters that interface the PEVs with the dc system and act as bidirectional battery chargers; hence, hereafter, a dc-dc converter is referred to as a *battery charger*.

From its ac side, the central VSC is interfaced with the host ac grid, is operated as a controlled dc-voltage power port [53], and regulates the dc voltage of the network. Thus, the central VSC enables a bidirectional exchange of energy between the dc system and the ac grid. The management unit supervises the operation of the dc system. Thus, it is assumed that a communication network [54] receives the power setpoints from the management unit and delivers them to the battery chargers. The communication network also collects metering information, for the management unit, from the central VSC and the battery chargers.

Upon his/her arrival, a PEV owner enters the following information, via a user interface, to the corresponding battery charger:

1. The energy exchange option (fast or optimal);

2. The charging mode (buying energy or selling energy);
3. The desired final value of SOC; and
4. The intended parking duration.

It is also assumed that the battery charger communicates with an onboard battery management system [63]. Thus, the value of the SOC at the arrival instant of the PEV is communicated to the battery charger and, from there, to the management unit. The power setpoints for the battery chargers are calculated by an *energy management strategy* (EMS), embedded in the management unit, through a constrained optimization process and based on the information received from the PEV owners and the ac grid.

Fig. 4.2 shows a schematic diagram of the dc system of Fig. 4.1. As the diagram indicates, the central VSC is interfaced with the host ac grid via a three-phase tie reactor, L_s ; the resistance R_s represents the aggregate effect of the on-state power loss of the semiconductor switches of the VSC and ohmic power loss of the tie reactor. Each distribution cable is represented by a corresponding series R-L branch. The convention in this chapter is that the first vehicle, PEV_1 , has arrived first, the second vehicle, PEV_2 , has arrived next, and so on. Also, in this chapter the battery chargers are not identified by fixed indices. Rather, a battery charger is *associated with* the vehicle to which it is connected. Thus, the power that enters the network-side port of the battery charger associated with the i^{th} PEV, in the k^{th} *energy exchange interval* (to be detailed in Section 4.5) of the parking period, is denoted by $P_{i,k}$. Since the battery chargers are bidirectional, $P_{i,k}$ can assume both positive and negative values. A positive value for $P_{i,k}$ corresponds to the charging of batteries of the i^{th} PEV, whereas a negative $P_{i,k}$ indicates the discharging of the batteries.

Due to the constant-power property of the battery chargers (dc-dc converters), [20, 28, 40, 59, 60, 64], the dc system is nonlinear in nature. Consequently, for a set of power setpoints, $\{P_{1,k}, P_{2,k}, \dots, P_{i,k}, \dots, P_{N,k}\}$, the dc system does not reach a steady state if the following inequality is not satisfied [65]:

$$\sum_{i=1}^N P_{i,k} \leq P_{dc_{max}}, \quad \forall k \quad (4.1)$$

where

$$P_{dc_{max}} = \frac{1}{4} \mathbf{v}_{dc}^T \mathbf{R}^{-1} \mathbf{v}_{dc}, \quad (4.2)$$

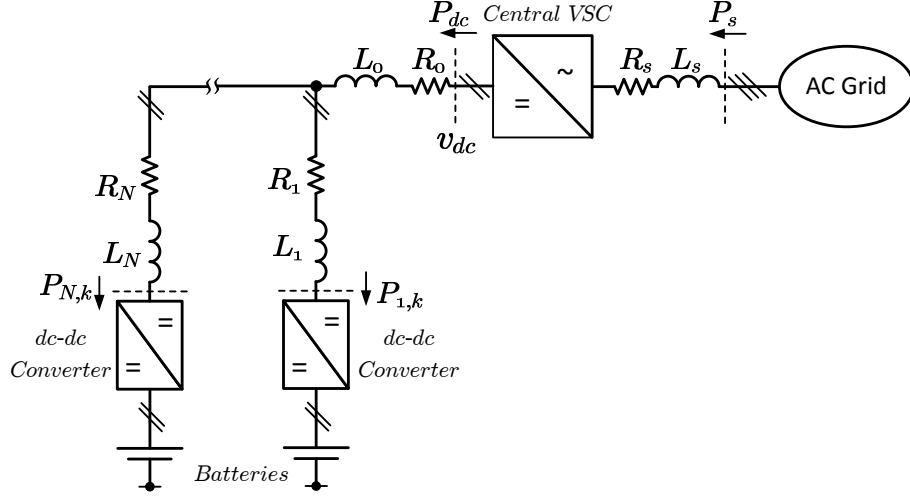


Figure 4.2: Schematic diagram of the dc system.

$$\mathbf{R} = \begin{bmatrix} R_0 + R_1 & R_0 & \cdots & R_0 \\ R_0 & R_0 + R_2 & \cdots & R_0 \\ \vdots & \vdots & \ddots & \vdots \\ R_0 & R_0 & \cdots & R_0 + R_N \end{bmatrix}_{N \times N}, \quad (4.3)$$

and

$$\mathbf{v}_{\text{dc}}^T = v_{dc}[1, 1, \cdots, 1]_{1 \times N}, \quad (4.4)$$

where N is the number of PEVs.

The EMS must issue the battery charger power setpoints in such a way that inequality (4.1) is not violated. It should be noted that P_{dcmax} is a positive value (since the matrix \mathbf{R} is positive-definite, assuming $R_i \neq 0$, for $i = 1, 2, \cdots, N$) and, therefore, as inequality (4.1) implies, the dc system does not arrive at a steady state if the aggregate power absorbed by the dc-dc converters exceeds a certain value, P_{dcmax} .

4.3 Constrained Optimization Problem

As mentioned in Section 4.2, to issue the power setpoints for the battery chargers, the EMS solves a constrained optimization problem. The optimization problem is formulated as:

$$\min_{P_{i,k}} \left(\sum_{k=1}^{M_i} P_{i,k} r_k \mu_{i,k} \right) \quad (4.5)$$

subject to

$$|P_{i,k}| \leq P_{rat_i} \quad \forall i, k \quad (4.6)$$

$$P_{i,k} \leq D_{L_k} - \sum_{j=1}^{i-1} P_{j,k} \quad \forall i, k \quad (4.7)$$

$$-P_{i,k} \geq G_{L_k} + \sum_{j=1}^{i-1} P_{j,k} \quad \forall i, k \quad (4.8)$$

$$\sum_{j=1}^i P_{j,k} \leq P_{dcmax} \quad \forall k \quad (4.9)$$

$$\sum_{k=1}^{M_i} P_{i,k} \mu_{i,k} = E_i \quad \forall i \quad (4.10)$$

where

$$\sum_{k=1}^{M_i} \mu_{i,k} = T_{P_i} \quad \forall i \quad (4.11)$$

$$0 < \mu_{i,k} \leq T_s \quad \forall i, k \quad (4.12)$$

$$E_i = \begin{cases} \frac{(SOC_{i,f} - SOC_{i,i}) E_{cap_i}}{\eta_i} & \text{if } (SOC_{i,f} - SOC_{i,i}) \geq 0 \\ (SOC_{i,f} - SOC_{i,i}) \eta_i E_{cap_i} & \text{if } (SOC_{i,f} - SOC_{i,i}) < 0 \end{cases} \quad (4.13)$$

In the forgoing formulation, subscript i ($= 1, 2, \dots, N$) corresponds to the order of the vehicle's arrival, as also indicated in Section 4.2. Variables r_k and $\mu_{i,k}$ denote, respectively, the wholesale energy price and the duration of the k^{th} energy exchange interval. Variable M_i signifies the number of energy exchange intervals for the i^{th} PEV, i.e., $k = 1, 2, \dots, M_i$. Parameter P_{rat_i} denotes the rated power of the (bidirectional) battery charger associated with the i^{th} PEV and is assumed to apply to both the charging and discharging modes. Variable D_{L_k} denotes the difference between the base load and the maximum permissible power demand in the ac distribution network with which the dc system has been integrated, in the k^{th} energy exchange interval. In other words, D_{L_k} is the maximum of the power that the battery chargers are collectively permitted to draw to charge the batteries. On the other hand, G_{L_k} is the difference between the base load and the maximum permissible power generation in the area; it is defined to preclude reverse power flow and over-voltage within the ac grid. Thus, G_{L_k} is the maximum

of the power that the battery chargers are permitted to generate collectively. Variable E_i denotes the total energy exchanged with the batteries of the i^{th} PEV. Thus, E_i is positive if the batteries are charged, and it is negative if the batteries are discharged. Variable T_{P_i} denotes the intended parking duration of the i^{th} PEV, and T_s is the largest duration of an energy exchange interval, which is assumed to be one hour in this study. Variables SOC_{i_i} and SOC_{i_f} are the initial and final values of SOC for the i^{th} PEV, respectively. Parameter E_{cap_i} denotes the energy storage capacity of the i^{th} PEV, and η_i is the efficiency of the battery charger associated with the i^{th} PEV, which is assumed to be the same for both charging and discharging modes.

4.4 Operation of EMS

Whenever a new PEV arrives the EMS first determines the energy exchange intervals for the PEV, through a process which will be detailed in Section 4.5. It then calculates and stores the values that the power setpoint of the associated battery charger must assume in the energy exchange intervals for the vehicle. Then, based on the calculated power setpoint values, the EMS updates the constraints (4.7) through (4.9) for the next upcoming vehicle.

A PEV owner has two options when he/she arrives at a charging station in the dc system: 1) the *optimal energy exchange option* and 2) the *fast energy exchange option*. In the optimal energy exchange option, the owner intends to minimize the charging cost or to maximize the discharging revenue. Thus, the EMS exercises the constrained optimization process of Section 4.3 to find the power setpoints for the associated battery charger. The EMS uses the overall intended parking duration of the PEV for the optimization process. In the fast energy exchange option, however, the owner intends to charge (or discharge) the batteries in the shortest possible time. The EMS, therefore, does not perform the optimization process, but it only applies the constraints (4.6) through (4.10). Thus, the associated battery charger is operated at its rated power, subject to the constraints associated with the existence of a steady-state operating point for the dc system and the limitations of the ac grid. In this option, the EMS does not reduce (the absolute value of) the power setpoint of the battery charger when it runs the optimization process for a vehicle that arrives subsequently. However, an extra service fee can be levied as a penalty on the owners who choose the fast energy exchange option, to encourage them to opt for the optimal option.

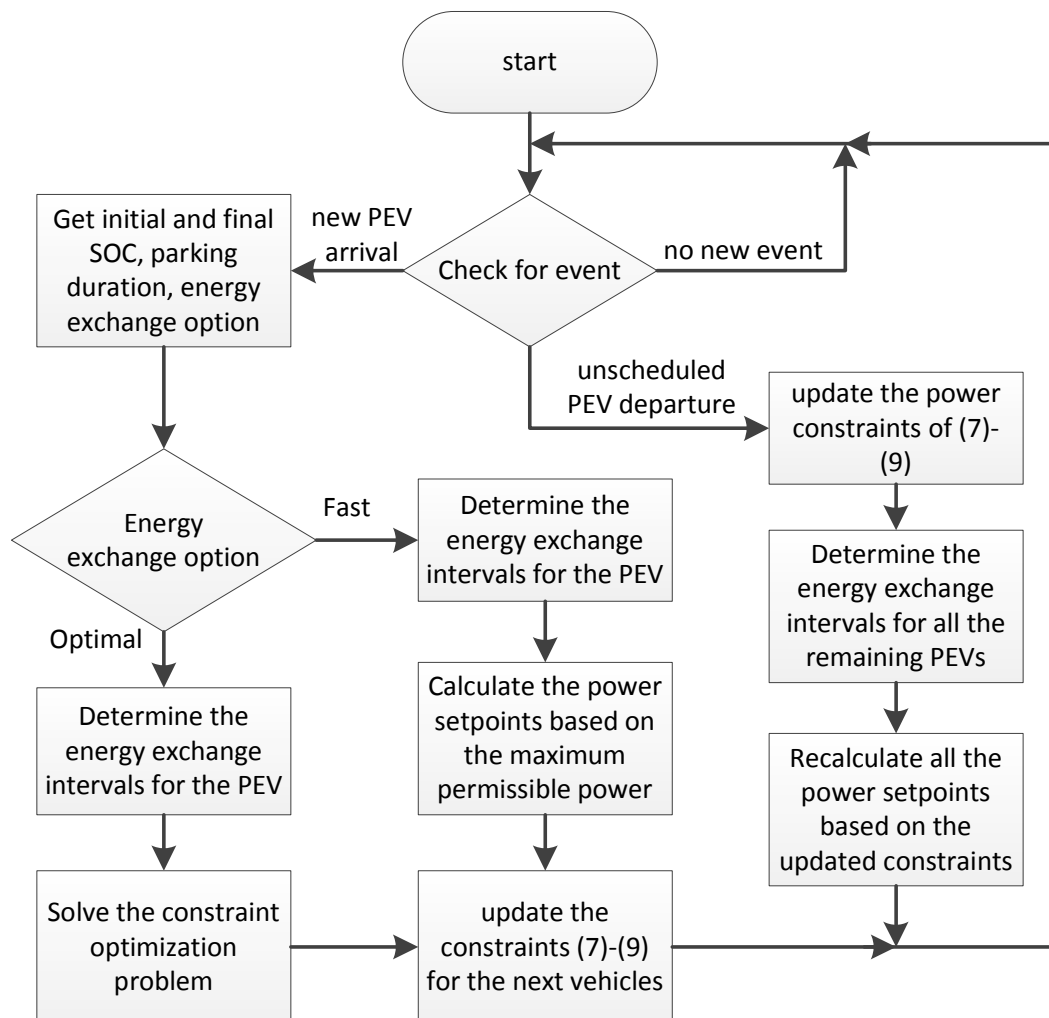


Figure 4.3: Flowchart of the proposed energy management strategy.

Fig. 4.3 shows the flowchart of the EMS. As Fig. 4.3 illustrates, the EMS constantly checks for a new event, which is either the arrival of a PEV or unscheduled departure of a PEV (scheduled departure of a PEV is not considered as an event, since the EMS already knows about the scheduled departure times). On the arrival of a new PEV, the EMS receives the initial SOC of the batteries, from the vehicle's battery management system. It also receives the desired final SOC, the intended parking duration, and the energy exchange option from the PEV. Based on this information, the EMS determines the energy exchange intervals for the PEV and, then, based on the selected energy exchange option, it calculates and issues the power setpoints for the associated battery charger.

In the event of an unscheduled departure of a PEV, the power capacity that was assigned to that PEV is released and can be used by the other PEVs (which are still connected to their associated battery chargers). Therefore, the EMS updates the energy

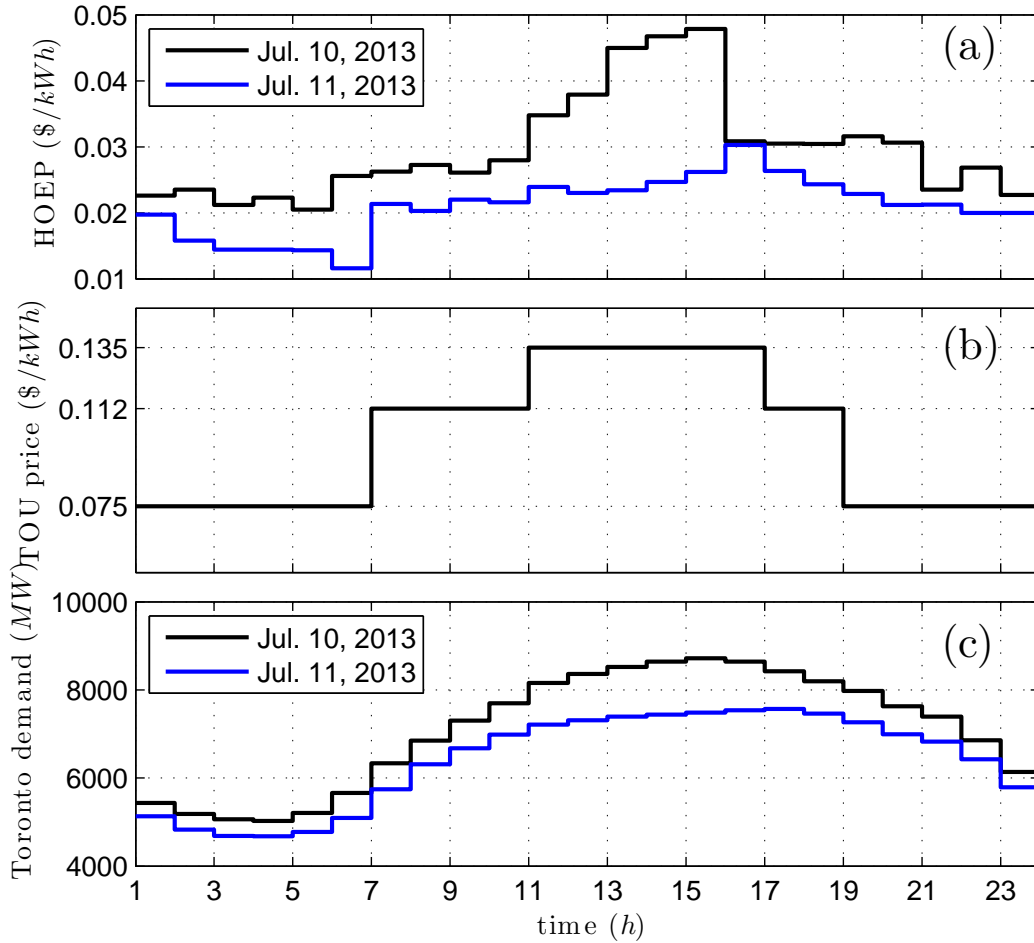


Figure 4.4: Energy price and power demand in Toronto, on July 10, 2013 and July 11, 2013.

exchange intervals and the constraints (4.7) through (4.9), and, based on the updated constraints, it recalculates the power setpoints of all remaining PEVs.

To run the optimization algorithm, the EMS needs to know the electricity price, the base load profile, and the generation and consumption limitations of the ac grid. For example, Fig. 4.4 depicts the hourly Ontario energy price (HOEP), the time-of-use (TOU) energy price, and the power demand, in the Toronto region, on July 10, 2013 and July 11, 2013 [66]. The HOEP is a wholesale energy price, which applies to any business that consumes more than 250,000 kWh of electricity per year [66]. Thus, a dc system with a large number of battery chargers is potentially subject to the HOEP for buying electricity from the ac grid, whereas ordinary homeowners have to pay the TOU energy price (which is normally higher than the HOEP). In a smart grid environment, the EMS can receive the base load profile for the next 24 hours, from the ac grid. Alternatively,

the EMS can forecast the base load profile based on the power demand information of the previous days [47].

4.5 Determination of Energy Exchange Intervals

As mentioned in Section 4.4, subsequent to the arrival of a vehicle, say the i^{th} PEV, the EMS determines the energy exchange intervals, i.e., the set $\{\mu_{i,1}, \mu_{i,2}, \dots, \mu_{i,M_i}\}$, for that PEV, based on the following set of rules and assumptions:

1. The first energy exchange interval starts with the arrival of the PEV.
2. If the PEV owner chooses the optimal energy exchange option, the end of the last energy exchange interval coincides with the intended departure time of the PEV. However, if the PEV owner chooses the fast energy exchange option, the EMS calculates the completion time for the energy exchange of the PEV, based on the power capacity available, and considers the completion time as the end of the last energy exchange interval for the vehicle.
3. The energy exchange intervals are continuous, i.e., the start of an energy exchange interval marks the end of the previous energy exchange interval (except for the first energy exchange interval).
4. Since the energy price and power demand information are changed hourly, the exact hours (for example, 8:00am, 9:00am, etc.) within the period between the first and last energy exchange intervals mark the starts of the energy exchange intervals. Thus, a charging period can last a maximum of one hour.
5. If the departure time, or the completion time, of a previously arrived PEV is earlier than the departure time, or the completion time, of a subsequently arrived PEV, then the departure time, or completion time, of the previously arrived PEV is considered as the start of an energy exchange interval for the subsequently arrived PEV.

Fig. 4.5 illustrates the implementation of the aforementioned set of rules for a four-vehicle case where the vehicles have all chosen the optimal energy exchange option. As Fig. 4.5 shows, for PEV_1 , the start of the first energy exchange interval, and the end of the last energy exchange interval, are determined only by the arrival and departure times

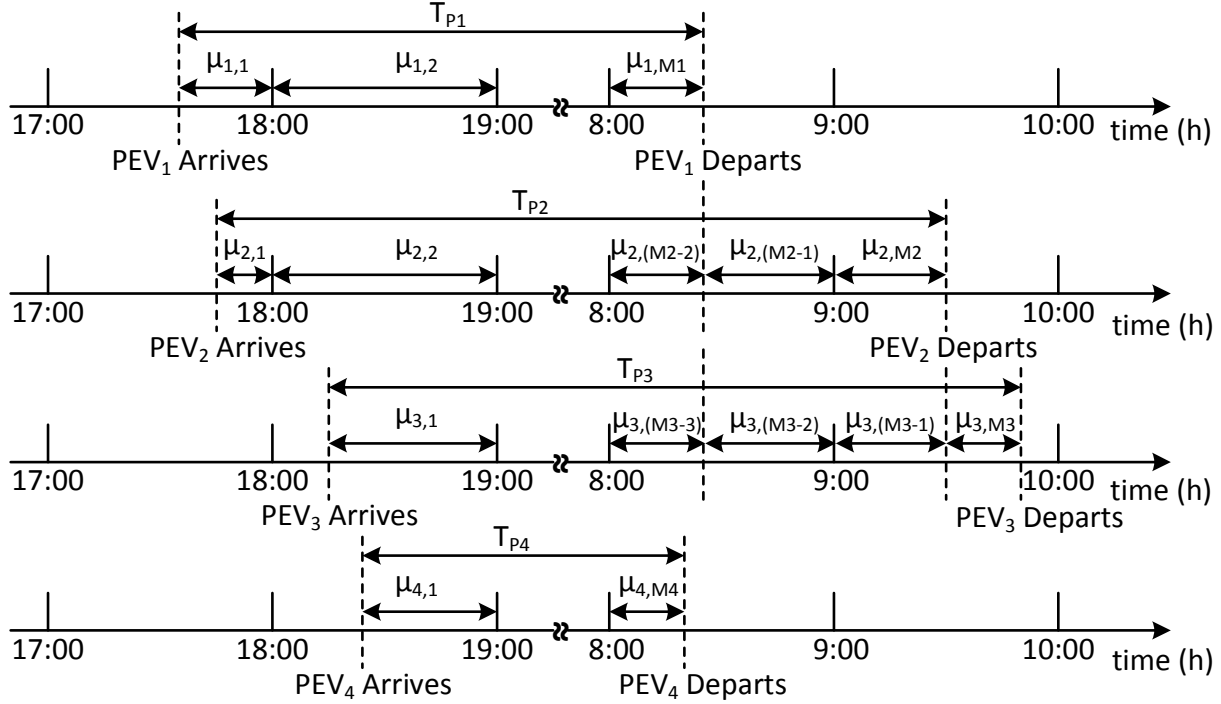


Figure 4.5: An example of determination of the energy exchange intervals for four PEVs with optimal energy exchange option.

of the vehicle itself. However, for vehicles PEV_2 and PEV_3 , the departure of PEV_1 ends energy exchange intervals, and starts new energy exchange intervals. The reason is that the departure of PEV_1 releases some power capacity in the dc system and, therefore, the constraints (4.7) through (4.9) change. Hence, the EMS can modify the power setpoints of PEV_2 and PEV_3 , for higher optimality. Similarly, as the figure shows, the departure of PEV_2 ends an energy exchange interval and starts a new energy exchange interval, for PEV_3 . The arrival and departure of PEV_4 , however, do not affect those of any other vehicle, since PEV_4 has arrived the latest. More importantly, the departure times of the other vehicles do not affect the energy exchange intervals of PEV_4 since the vehicle is supposed to leave earlier than all the previously arrived vehicles.

Fig. 4.6 shows another example of determination of the energy exchange intervals. In this example, PEV_1 has opted for the fast energy exchange option, whereas the other two vehicles have elected the optimal energy exchange option. Thus, it is the completion time, rather than the departure time, of PEV_1 that results in the start of new energy exchange intervals for PEV_2 and PEV_3 . Similar to the previous example, the departure of PEV_2 only affect the energy exchange intervals of the vehicles that have arrived later, that is, PEV_3 in this example.

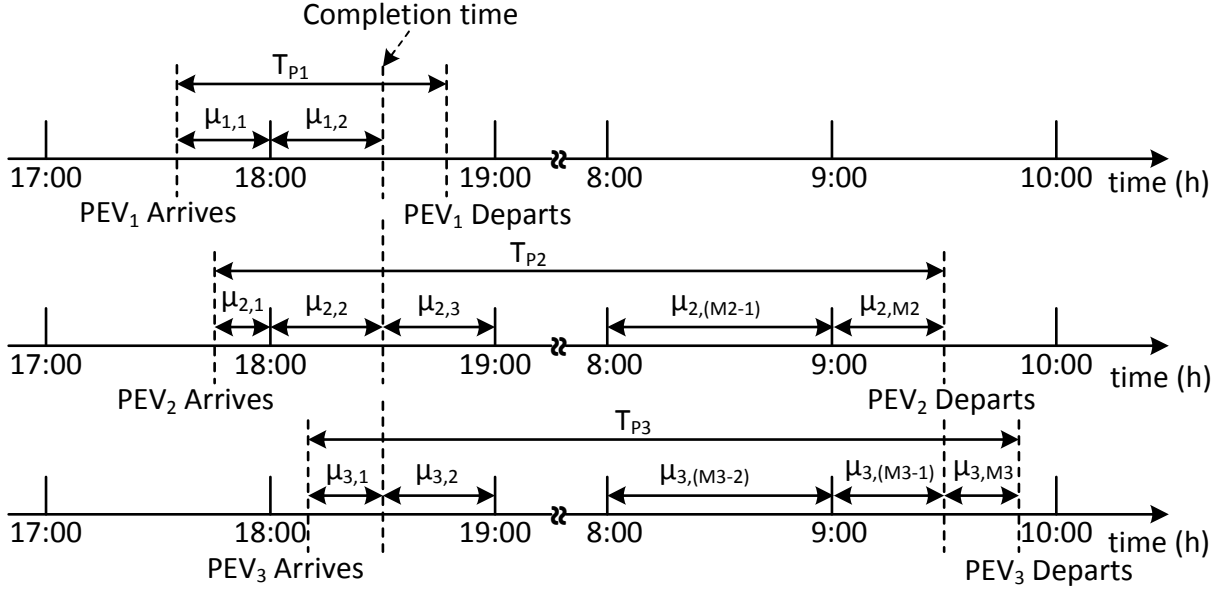


Figure 4.6: An example of determination of the energy exchange intervals for three PEVs; The first PEV with the fast energy exchange option and the other two PEVs with the optimal energy exchange option.

The two above examples indicate how the proposed EMS can seamlessly handle both the fast and the optimal energy exchange requests.

4.6 Simulation Results

Two study cases have been considered with respect to the location of the dc system. The first case investigates the operation of the dc system and proposed EMS, for a residential parking lot where the owners park overnight and charge their vehicles for the morning commute. The second case, however, assumes a commercial parking lot where the vehicles are parked during the day and exchange energy (in either direction) with the dc system. For the simulations, the power consumption of 200 households has been assumed as the base load profile. To that end, the base load profile of Fig. 4.4 has been scaled down to feature a peak value of 400 kW, based on the assumption that the peak load of a typical household is about 2 kW [7] [48]. Also, it is assumed that 50 vehicles are involved in energy exchange activities in the residential area, representing a penetration rate of 25% in view of the existence of 200 households. It is supposed that a parking lot operator controls the operation of the dc distribution system. The operator, therefore, can charge the PEV owners and the ac grid for the services that are providing to them through the dc distribution system. The simulations have been conducted in MATLAB

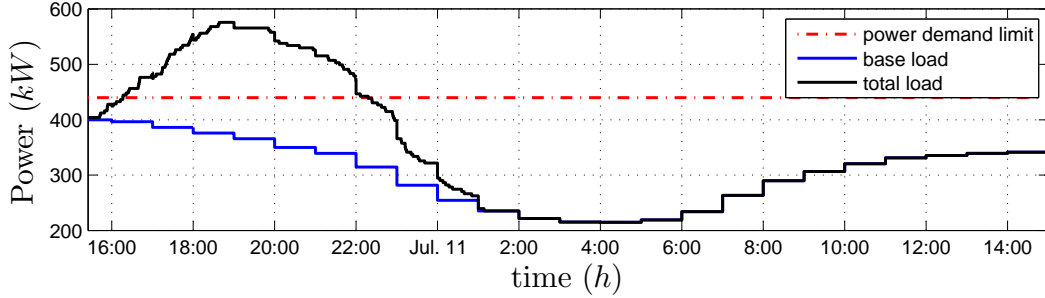


Figure 4.7: Case I, Scenario 1: total load under uncoordinated charging of PEVs using 4-kW ac-dc battery chargers.

software environment, and Appendix F reports the parameters assumed, unless otherwise is mentioned.

4.6.1 Case I: residential parking lot; evening and night time

In the first case, the arrival times of the PEVs are assumed to be normally distributed, with a mean value of 5:00pm and a variance of one hour. The departure times also are assumed to be normally distributed with a mean value of 8:00am (i.e., on the next day when the owners typically leave for work) and a variance of one hour. The initial and final SOC values of the batteries are assumed to be uniformly distributed between 20% to 50%, and between 80% to 90%, respectively.

Scenario I-1

This scenario assumes that there is no dc system and that the owners all start to charge their vehicles once they arrive home, using 4-kW conventional ac-dc battery chargers. Fig. 4.7 shows the power demand limit for the ac grid, the base load profile of the residential area, and the profile of the *total load* which is referred to as the base load plus the aggregate power absorbed by the PEVs. Thus, the total load becomes smaller if the PEVs predominantly discharge their batteries. As Fig. 4.7 indicates, the total load exceeds the power demand limit of the grid and may, therefore, result in prohibitive voltage drops throughout the network.

Scenario I-2

It is assumed in this scenario that the PEVs are interfaced with the dc system, through 40-kW dc-dc battery charges, but their energy exchange activities are not supervised by

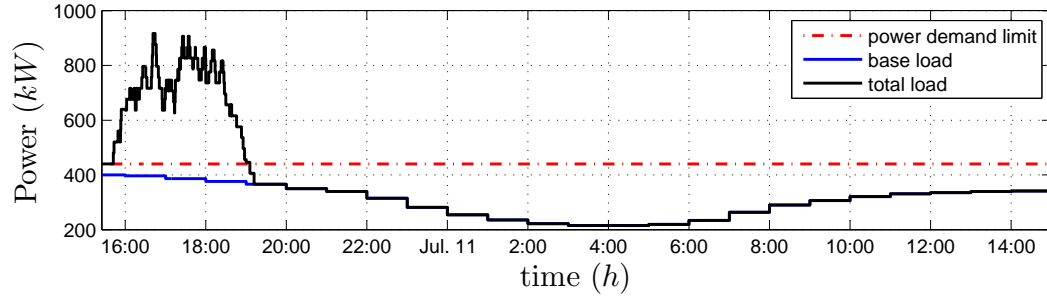


Figure 4.8: Case I, Scenario 2: total load if the PEVs are charged through the dc system without the supervision of the EMS.

the proposed EMS, i.e., the owners start to charge their PEVs at the rated power, as soon as they arrive. Fig. 4.8 illustrates the outcome and indicates that, as compared with Scenario 1, the PEVs in this scenario are charged faster, due to the higher power rating of the battery chargers. However, the total is considerably larger than the power demand limit for the grid and may, consequently, adversely affect the voltage profile in the network. It should be noted that a dc system can host 40-kW battery chargers, whereas a household cannot.

Scenario I-3

This scenario assumes that the vehicles are interfaced with a dc system and their energy exchange activities are supervised by the proposed EMS. It also assumes that the owners have all chosen the optimal energy exchange option. Fig. 4.9 illustrates the outcome and indicates that the EMS in this scenario attempts to charge the vehicles in the hours when the wholesale energy price is low, e.g., from 3:00am to 7:00am of the next day, July 11. The EMS also manages to keep the total load below the power demand limit, by imposing the constraints in its optimization exercise.

Scenario I-4

This scenario is the same as Scenario 3 except that the owners have all chosen the fast energy exchange option in this scenario. Thus, the EMS permits the largest possible power import for each PEV, while it minds the power demand limit of the grid. Therefore, as Fig. 4.10 indicates, the total load remains below the power demand limit for the grid.

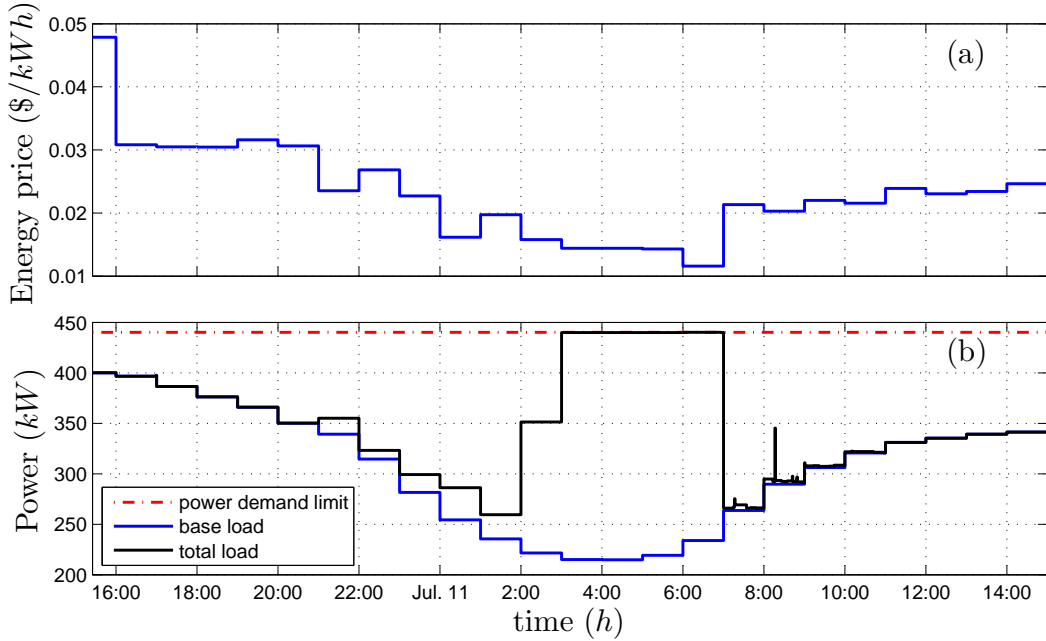


Figure 4.9: Case I, Scenario 3: total load if the PEVs are charged through the dc system, under the supervision of the EMS, based on the optimal energy exchange option.

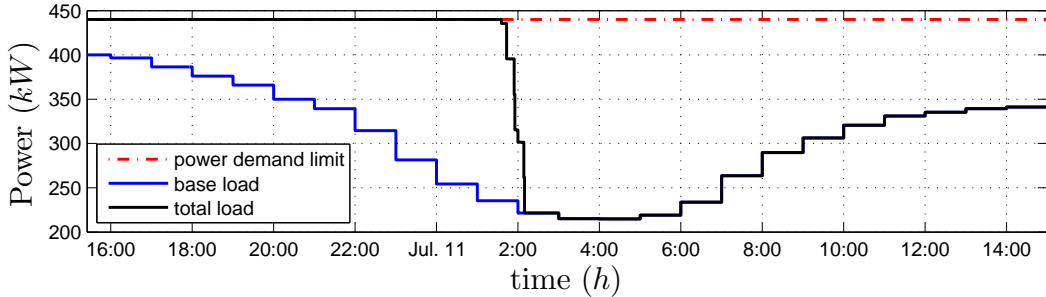


Figure 4.10: Case I, Scenario 4: total load if the PEVs are charged through the dc system, under the supervision of the EMS, based on the fast energy exchange option.

Scenario I-5

In this scenario, it is assumed that the charging activities of the PEVs are supervised by the proposed EMS in the dc system, and five PEVs, i.e., 10% of the owners, have chosen the fast energy exchange option, whereas the remainder of owners have opted for the optimal energy exchange option. Fig. 4.11 indicates that the EMS seamlessly responds to the requests for both energy exchange options.

As Fig. 4.11 illustrates, the EMS assigns the largest possible power setpoints to the vehicles that have opted for the fast energy exchange option, while maintains the total load below the power demand limit of the grid. At the same time, the EMS optimally

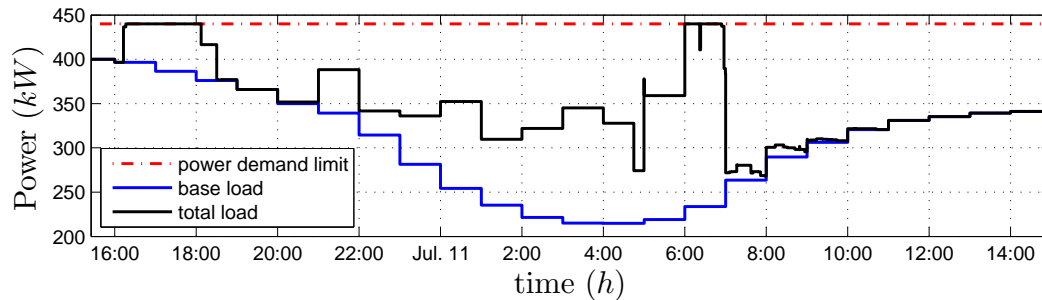


Figure 4.11: Case I, Scenario 5: total load if the PEVs are charged through the dc system, under the supervision of the EMS, based on a combination of both fast and optimal energy exchange options.

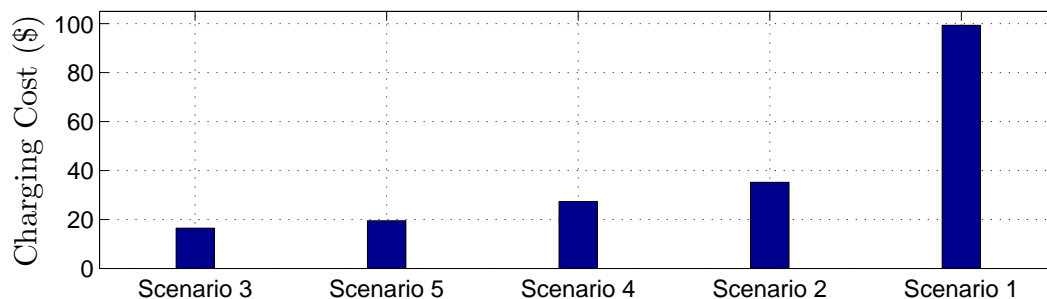


Figure 4.12: Case I: charging cost in different scenarios.

assigns the power setpoints to the vehicles that have elected the optimal energy exchange option, to minimize their charging costs.

Fig. 4.12 plots the charging cost for each of the aforementioned scenarios. As Fig. 4.12 shows, the charging cost in Scenario 1, about \$99, is remarkably higher than the charging cost in the other scenarios, since in Scenario 1 the owners purchase energy based on the TOU price, which, typically, is higher than the HOEP wholesale price. A comparison between the charging costs of Scenario 2 (unsupervised charging) and Scenario 3 (optimal charging) indicates that the unsupervised charging costs about 100% more than the optimal charging. Fig. 4.12 also indicates that the charging cost in the scenario where the owners all choose the optimal energy exchange option (Scenario 3) is about 66% of the charging cost in the scenario where the vehicles all opt for the fast energy exchange option (Scenario 4). In the scenario where both fast and optimal energy exchange options have been elected (Scenario 5), the charging cost is proportional to the number of vehicles charged through the fast energy exchange option.

The parking lot operator can charge the PEV owners by an administration fee to compensate the operation costs and to make the revenue. This administration fee can

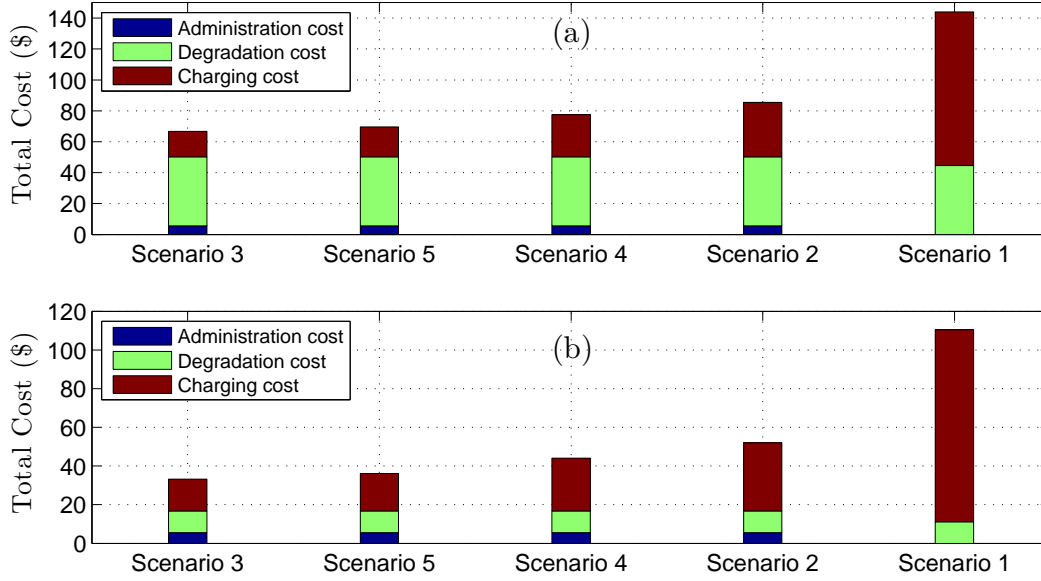


Figure 4.13: Total charging cost for different scenarios in Case I; (a) with degradation costs of 0.04\$/kWh (b) with degradation costs of 0.01\$/kWh.

be as much as 10% of the average wholesale electricity price [23]. In this thesis, the administration fee of \$0.005/kWh has been considered for the PEV owners who use the dc distribution system to charge or discharge their vehicles. Battery depreciation or degradation cost is another factor that contributes in the overall charging cost of the PEVs. In [67], based on the lowest price of the batteries for an electric vehicle, and a typical life time of 2200 cycles for charging and discharging of the batteries, the degradation cost of around 0.04\$/kWh has been calculated. This means that for every 1 kWh of energy exchange, charging or discharging, the value of the batteries decreases by 0.04\$ in average. However, with current research efforts to improve the battery technologies, it is expected to have the batteries with much longer life time, 10000 cycles for example, in the future [68]. Therefore, in this thesis, two degradation costs of 0.04\$/kWh and 0.01\$/kWh have been considered for the depreciation of the batteries.

Fig. 4.13 plots the total charging cost for all the scenarios in Case I, considering the administration and the degradation costs. Two degradation rate of 0.04\$/kWh and 0.01\$/kWh have been considered to calculate the total costs. It should be noted that for Scenario 1, there is no administration fee as the PEV owners don't use the dc distribution system to charge their vehicles. Table 4.1 summarizes the charging costs for Case I.

Table 4.1: Total charging cost for different scenarios in Case I

Cost		Scenario				
		1	2	3	4	5
Degradation cost cost of 0.04 \$	Charging cost (\$)	99.27	35.18	16.41	27.30	19.42
	Degradation cost (\$)	44.62	44.62	44.62	44.62	44.62
	Administration cost (\$)	0	5.57	5.57	5.57	5.57
	Total cost (\$)	143.90	85.39	66.62	77.51	69.62
Degradation cost of 0.01 \$	Charging cost (\$)	99.27	35.18	16.41	27.30	19.42
	Degradation cost (\$)	11.15	11.15	11.15	11.15	11.15
	Administration cost(\$)	0	5.57	5.57	5.57	5.57
	Total cost (\$)	110.43	51.91	33.15	44.04	36.15

4.6.2 Case II: business area parking lot; day time

In the second case, the arrival time of PEVs are considered to be normally distributed, with a mean value of 9:00am and a variance of one hour. As a typical working day lasts 8 hours, the departure times are also assumed to be normally distributed, with a mean value of 5:00pm and a variance of one hour. Further, the initial and final SOC values of the PEV batteries are assumed to be uniformly distributed from 70% to 80%, and from 30% to 40%, respectively. It is assumed that the PEV owners intend to discharge their batteries (or sell energy), unless otherwise is mentioned.

Scenario II-1

This scenario assumes that the PEV owners have all chosen the optimal energy exchange option, in order to discharge their batteries to their desired final SOC values. Fig. 4.14 illustrates the outcome and that the EMS schedules the discharging activities mostly when the energy price is high, e.g., between 2:00pm and 4:00pm. It should be noted that, the sign of the power setpoint is negative for a charger working in the discharging mode. Therefore, a higher energy price results in a lower value for the cost function (4.5) and, thus, a higher revenue for the PEV owner. The EMS also limits the power generation of the PEVs, to preclude reverse power flow and over-voltages in the ac grid. As Fig. 4.14 shows, the total load never becomes negative, i.e., the ac grid does not experience a reverse power flow.

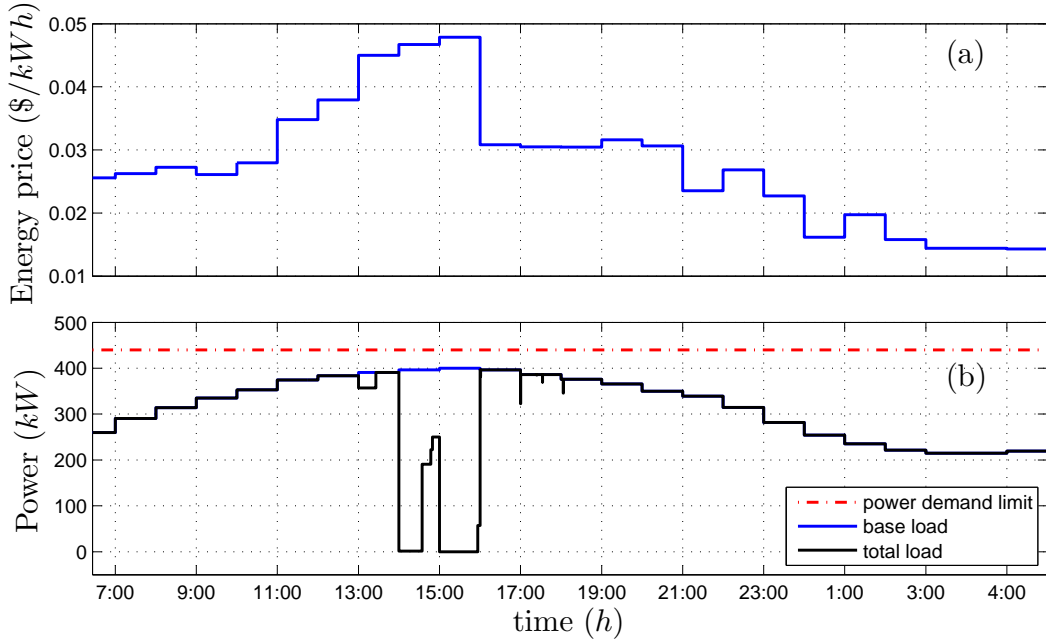


Figure 4.14: Case II, Scenario 1: total load with batteries discharging if the owners all choose the optimal energy exchange option.

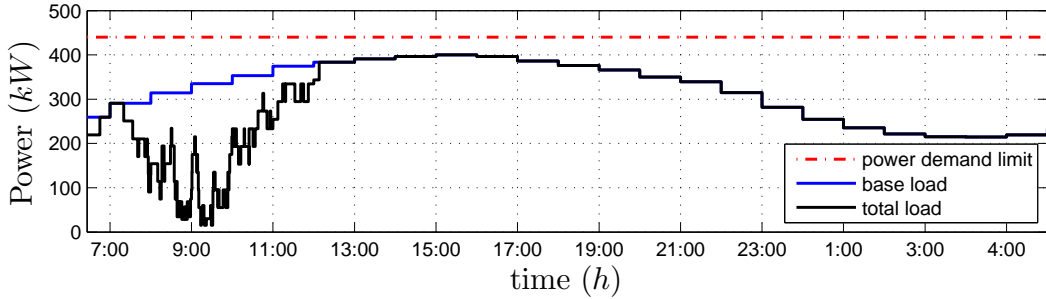


Figure 4.15: Case II, Scenario 2: total load with batteries discharging if the owners all choose the fast energy exchange option.

Scenario II-2

In this scenario, it is assumed that the PEV owners have all chosen the fast energy exchange option for discharging their batteries. Thus, the EMS commands the maximum permissible power export to the battery chargers, while it minds the power generation limit of the ac grid, to preclude reverse power flow and over-voltages. Fig. 4.15 illustrates the outcome and indicates that, as compared with Scenario 1, the energy export is completed considerably faster, at about 12:00pm. Fig. 4.15 also shows that the total load does not become negative, i.e., the ac grid does not experience a reverse power flow.

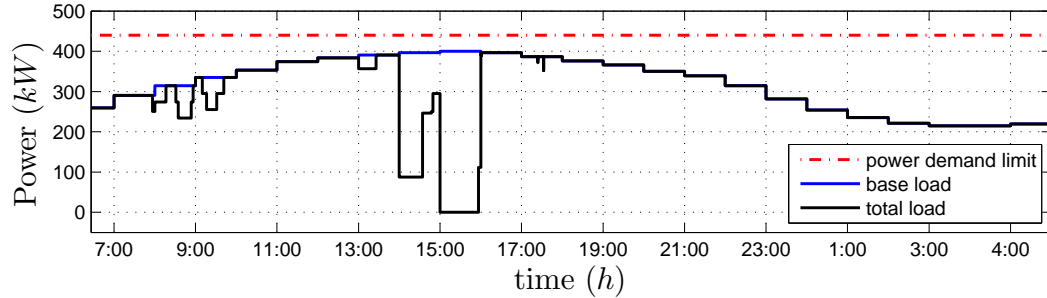


Figure 4.16: Case II, Scenario 3: total load with batteries discharging if 10% of the owners choose the fast energy exchange option.

Scenario II-3

This scenario assumes that 10% of the owners have chosen the fast energy exchange option, whereas the remainder of the owners have opted for the optimal energy exchange option, for selling power, and Fig. 4.16 illustrates the outcome. Thus, for the owners who have elected the fast energy exchange option, the export of energy starts immediately after their arrivals, from about 7:00am to 10:00am, as Fig. 4.16 indicates. For this group of owners, the EMS commands the largest (in absolute value) permissible values for the power setpoints. For the owners who have opted for the optimal energy exchange option, on the other hand, the EMS exercises the optimization algorithm, to maximize their discharging revenues. Therefore, as Fig. 4.16 shows, for this group of owners the discharging process takes place during the hours in which the energy price is high, i.e., from 2:00pm to 4:00pm. The EMS also ensures that the power generation limit of the ac grid is not violated, in order to circumvent reverse power flow and over-voltages.

Scenario II-4

This scenario assumes that 20% of the owners (i.e., 10 vehicles) have elected to charge their batteries from a SOC level of 40% to a SOC level of 80%, while the remainder of the owners intend to discharge their batteries (sell energy). Thus, the EMS exercises its optimization algorithm to minimize the charging costs, and to maximize the discharging revenues. Fig. 4.17 illustrates the base load profile, the total load profile, and the power demand limit for the ac grid. It is observed that the total load does not exceed the limit, nor does it become negative (corresponding to a reverse power flow).

Fig. 4.18 plots the discharging revenue for each aforementioned scenario in Case II. It should be noted that for Scenario 4, the total revenue is calculated only for the owners

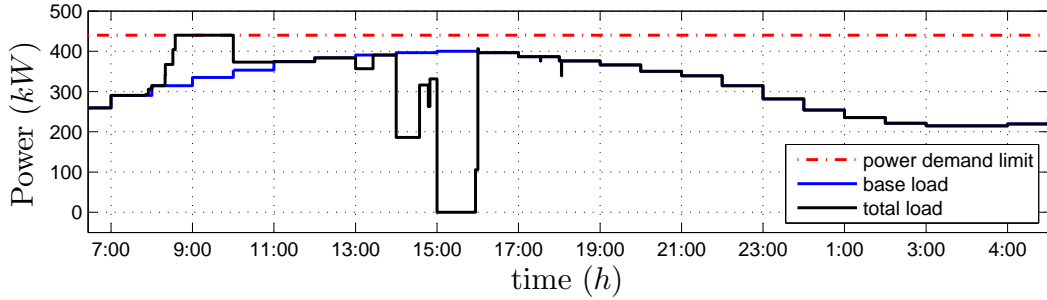


Figure 4.17: Case II, Scenario 4: total load if 20% of the owners intend to charge their batteries, while the rest plan to discharge their batteries.

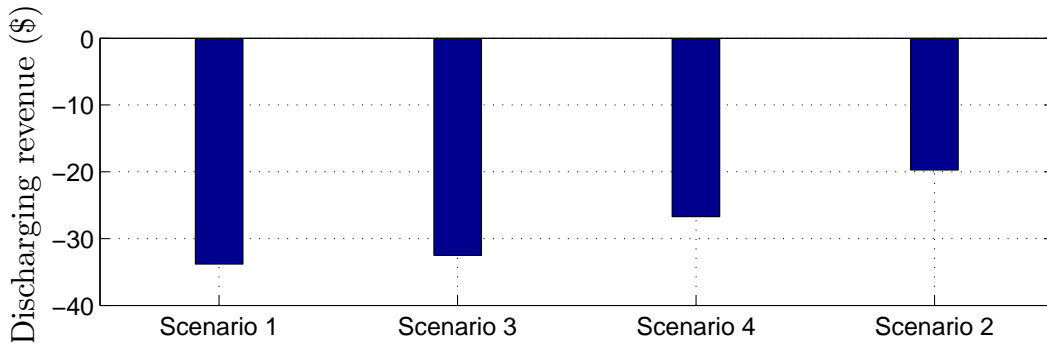


Figure 4.18: Case II: total discharging revenue in different scenarios.

who sell the energy, i.e., 80% of the total owners. As Fig. 4.18 shows, if the owners all elect the optimal energy exchange option, i.e., Scenario 1, the discharging revenue is about 75% higher as compared to the scenario in which the owners all opt for the fast energy exchange option, i.e., Scenario 2. In scenarios with a combination of both fast and optimal energy exchange options, the revenue decreases with the number of owners who have elected the fast energy exchange option.

Fig. 4.19 and Table 4.2 summarize the net revenue/cost for all the scenarios in Case II, considering the administration and the degradation costs. Two degradation rates of 0.04\$/kWh and 0.01\$/kWh have been considered to calculate the net revenue/cost. Table 4.2 shows that for degradation rate of 0.04\$/kWh, the fast energy exchange option for the discharging operation is not financially feasible for the PEV owners. However, it should be noted that the revenue calculation in Case II is done solely based on selling the energy with the wholesale price, while for V2G operation, the parking lot operator can charge the ac power grid for providing the ancillary services with higher price rate than the wholesale energy price. Therefore, the total revenue will be increased and the PEV owners can receive a portion of the increased revenue [25, 44].

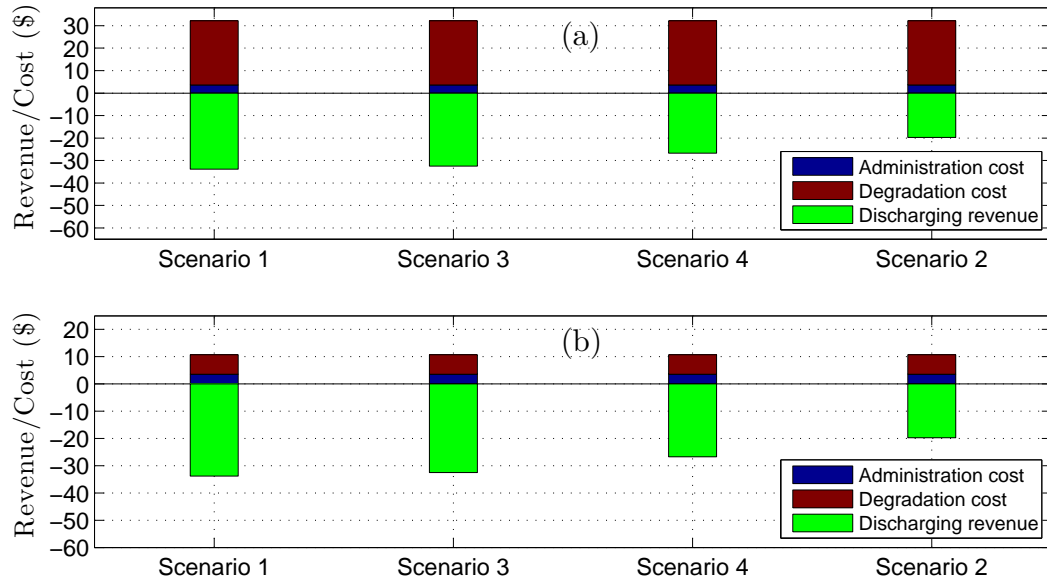


Figure 4.19: Revenue and cost for different scenarios in Case II; (a) with degradation costs of 0.04\$/kWh (b) with degradation costs of 0.01\$/kWh.

4.7 Conclusion

An energy management strategy (EMS) was proposed for power system integration of plug-in electric vehicles (PEVs). The proposed EMS is embedded in the intelligence of a dc distribution system intended for integrating PEVs in a parking lot through bidirectional dc-dc electronic power converters (battery chargers). In turn, the dc distribution system is interfaced, and exchanges energy, with a host ac grid through a central three-phase voltage-sourced converter (VSC). The proposed EMS exercises an on-line constrained optimization algorithm, to manage the power flow within the dc system and the power exchange with the host grid. The proposed EMS offers two energy exchange options to the PEV owners: (1) The fast energy exchange option for the owners who desire to minimize their energy exchange time and (2) The optimal energy exchange option for the owners who intend either to minimize their cost of charging batteries or to maximize their revenue of selling the stored energy. The proposed EMS takes into account the constraints of the ac grid, in terms of power demand and power generation, to circumvent under-voltage, over-voltage, and reverse power flow issues. Various operational scenarios were simulated in the chapter to demonstrate the effectiveness of the proposed EMS.

Table 4.2: Net cost/revenue for different scenarios in Case II

Cost/Revenue		Scenario			
		1	2	3	4
Degradation cost cost of 0.04 \$	Discharging revenue (\$)	-33.81	-19.75	-32.50	-26.73
	Degradation cost (\$)	28.59	28.59	28.59	28.59
	Administration cost (\$)	3.57	3.57	3.57	3.57
	Net cost/revenue (\$)	-1.64	12.41	-0.34	5.43
Degradation cost of 0.01 \$	Discharging revenue (\$)	-33.81	-19.75	-32.50	-26.73
	Degradation cost (\$)	7.14	7.14	7.14	7.14
	Administration cost(\$)	3.57	3.57	3.57	3.57
	Net cost/revenue (\$)	-23.09	-9.03	-21.78	-16.01

Chapter 5

Summary, Conclusions, and Future Work

5.1 Summary

The outlook of growing number of electric vehicles and their impacts on the power grid have motivated extensive research efforts toward resolving the technical challenges of the power system integration of the large number of electric vehicles. The main objective of this research is to address some concerns related to power system integration of electric vehicles.

In Chapter 1 of this thesis, the research objectives and the contributions of the thesis are presented. Chapter 1 also includes background information on electric vehicles and an introduction to the charging strategies of electric vehicles and their advantages and challenges.

Chapter 2 investigates a dc distribution system for power system integration of the electric vehicles. In this chapter, basic control strategies for the main components of the dc distribution system, i.e., central voltage-sourced converter (VSC) and bidirectional dc-dc converters, have been discussed. Chapter 2 also focuses on the modeling of the dc distribution system for a large number of electric vehicles; a mathematical model has been proposed to analyze the behavior of the dc system. The proposed model captures both the steady-state and dynamic characteristics of the system, and therefore it can be used for identifying the condition for existence of a steady state, as well as for stability analysis. The possibility of instability of the dc distribution system, due to the constant-power property of the dc-dc converters, is discussed in Chapter 3. A simple and effective

method is proposed in the chapter to enhance the stability of the system.

Finally, Chapter 4 of the thesis presents an energy management strategy to control the power flow between the dc distribution system and the power grid. The proposed strategy offers both fast and optimized charging options to the owners of the electric vehicles to charge or discharge their vehicles. Several energy exchange scenarios also have been simulated in this chapter to show the benefits of implementation of the proposed strategy.

5.2 Conclusions

The conclusions of this thesis are as follows:

- It was discussed that for power system integration of plug-in electric vehicles, a dc distribution system has more benefits as compared with a system of ac-dc battery chargers; the dc distribution system offers a higher efficiency and enables an easier integration of renewable energy sources such as photovoltaic (PV) and fuel-cell systems. Furthermore, by using a dc distribution system, the power grid needs to communicate only with one entity, i.e., the intelligence of the management unit of the dc system, rather than with multiple ac-dc battery chargers. Thus, the thesis presented an accurate mathematical model to analyze the dynamic and steady-state behavior of a dc distribution system. Using the presented model, the thesis further explained that the dc distribution system is prone to instabilities due to the constant-power property of the dc-dc converters.
- It is essential to protect a dc distribution system against instability. The thesis demonstrated that a stability enhancement method based on local measurement for dc-voltage of the dc-dc converters can be devised to increase the stability margin of the dc distribution system. The salient feature of the developed stability enhancement method is that it is simple and does not require information internal to the system or its embedded dc-dc converters, and does not need hardware modifications. Rather, it only employs local measurements and individual power setpoints and, therefore, can be exercised in a decentralized fashion. These, in turn, permit the use of commercially available dc-dc converters (battery chargers), which is expected to further reduce the overall cost of the system. The mathematical model of the dc system, after applying the proposed method, is also presented in the thesis to demonstrate the effectiveness of the proposed method.

- Finally, the thesis proposed an energy management strategy (EMS) to control the power flow in the dc distribution system. The proposed EMS is embedded in the intelligence of the management unit of the dc distribution system and exercises an on-line constrained optimization algorithm, to manage the power flow within the dc system and the power exchange with the host grid. The proposed EMS offers two energy exchange options to the PEV owners: (1) The fast energy exchange option for the owners who desire to minimize their energy exchange time and (2) The optimal energy exchange option for the owners who intend either to minimize their cost of charging batteries or to maximize their revenue of selling the stored energy. The proposed EMS takes into account the constraints of the ac grid, in terms of power demand and power generation, to circumvent under-voltage, over-voltage, and reverse power flow issues. Various operational scenarios were simulated in the thesis to demonstrate the effectiveness of the proposed EMS.

5.3 Future Work

The following topics are suggested for a future work:

- An investigation into the impacts of the communication network parameters on the performance of the dc distribution system: The communication network parameters, such as network delay and error rate may influence the performance of the dc distribution system [69]. Therefore, this can be a potential area for further research.
- Extending the modeling process of the dc system to include linear loads: The systematic method for developing a model for the dc distribution system in Chapter 2 can be used to find mathematical models for dc distribution systems with different applications that involve linear loads. Fig. 5.1 shows the equivalent circuit of a dc system with mixed dc-dc converters and linear loads; the linear loads are represented by a parallel connection of a resistor, an inductor, and a capacitor.
- Extending the modeling process for dc systems with different topologies and configurations: In this thesis a method has been proposed for developing a model for the dc systems with widely used bus configuration. Based on the presented method a new approach can be used for developing mathematical models for dc systems with topologies. The mesh topology, for example, is used in the multi-terminal

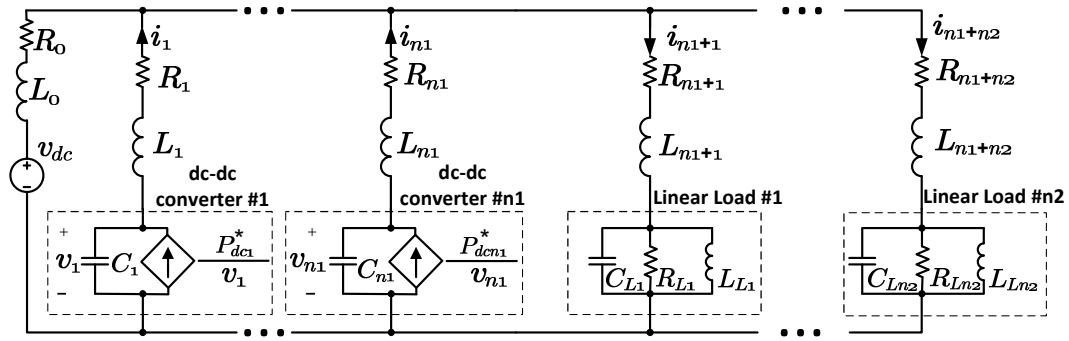


Figure 5.1: Equivalent circuit of a dc system with mixed dc-dc converter and linear loads.

dc (MTDC) systems [70]. In this case, an interconnection matrix can be used to develop a general model for the dc system.

Appendix A

Modeling of a droop-based dc-dc converter in a dc system

Fig. A.1 shows the block diagram of a full-bridge dc-dc converter with a voltage-droop mechanism in a dc system. The voltage-droop mechanism has been used to determine the power exchange setpoint between a dc power source and the rest of the dc system. In this figure, P_{nomi}^* and v_{nomi}^* represent the nominal values for the power setpoint and dc voltage, respectively. The amount of power, P_{dci} , that is exchanging between the dc power source $\#i$ and the rest of the dc system has a proportional relation with the dc voltage value, v_i [71]. Fig. A.2 shows the relation between the dc voltage and the power setpoint of the dc-dc converter. The slope of the droop in Fig. A.2 is determined based on the value of the droop gain, D_i . Fig. A.3 shows a simplified model of the dc-dc converter of Fig. A.1. Thus, the following family of equations describes the dynamics of the droop-based dc-dc converter of Fig. A.3:

$$P_{si}^* = P_{nomi}^* - D_i(v_i - v_{nomi}) \quad (\text{A.1})$$

$$C_i \frac{dv_i}{dt} = \frac{P_{si}^*}{v_i} - i_i. \quad (\text{A.2})$$

Substituting (A.1) in (A.2), one obtains

$$C_i \frac{dv_i}{dt} = \frac{P_{nomi}^*}{v_i} - D_i + \frac{D_i v_{nomi}}{v_i} - i_i. \quad (\text{A.3})$$

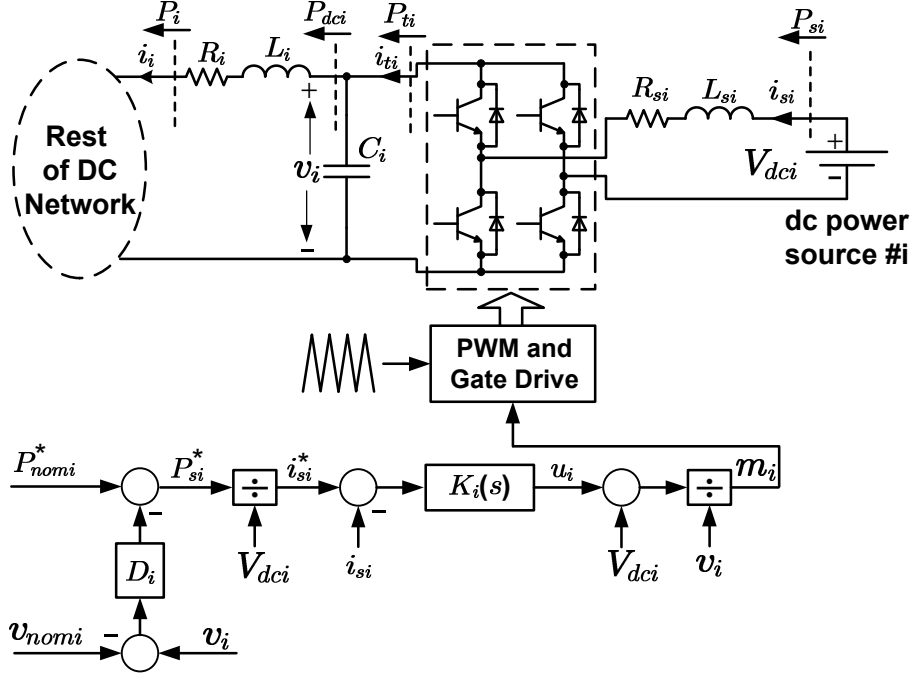


Figure A.1: The schematic diagram of a full bridge bidirectional dc-dc converter with a voltage-droop mechanism.

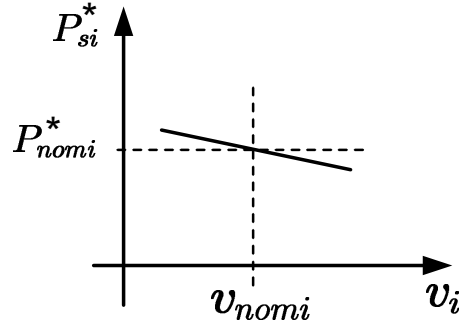


Figure A.2: Relation between P_{si}^* and v_i in a droop-based dc-dc converter.

Linearizing (A.3), one finds

$$C_i \frac{d\tilde{v}_i}{dt} = -\frac{P_{xi}^*}{V_i^2} \tilde{v}_i - \tilde{i}_i \quad (\text{A.4})$$

where

$$P_{xi}^* = D_i v_{nomi} + P_{nomi}^* \quad (\text{A.5})$$

Comparing (A.4) to (2.26), one can follow the same approach of Section 2.3.2 to develop a state-space model for the dc system that includes droop-based dc-dc converters.

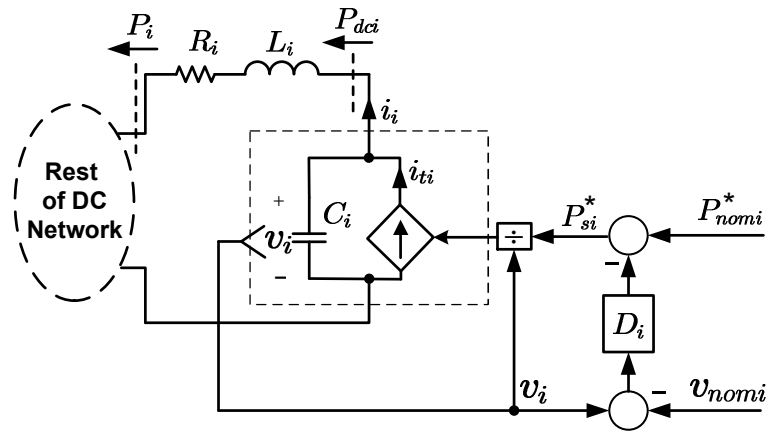


Figure A.3: The simplified model of the droop-based dc-dc converter of Fig. A.1.

Appendix B

Positive-Definiteness of \mathbf{R} and \mathbf{L} matrices

Lemma B.0.1 *If $R_i \neq 0$ ($i = 1, 2, \dots, n$), then \mathbf{R} in equation (2.19) is a positive-definite matrix.*

Proof Based on (2.19), \mathbf{R} is given by

$$\mathbf{R} = \mathbf{R}_0 + \mathbf{R}_b \quad (\text{B.1})$$

where \mathbf{R}_0 and \mathbf{R}_b have been defined in (2.16) and (2.17).

Let consider $\mathbf{w} = [w_1 \ w_2 \ \dots \ w_n]^T$ as a nonzero vector. Multiplying \mathbf{R}_0 by \mathbf{w}^T from left and by \mathbf{w} from right, gives

$$\mathbf{w}^T \mathbf{R}_0 \mathbf{w} = [w_1 \ w_2 \ \dots \ w_n] \begin{bmatrix} R_0 & R_0 & \dots & R_0 \\ R_0 & R_0 & \dots & R_0 \\ \vdots & \vdots & \ddots & \vdots \\ R_0 & R_0 & \dots & R_0 \end{bmatrix}_{n \times n} \begin{bmatrix} w_1 \\ w_2 \\ \vdots \\ w_n \end{bmatrix} \quad (\text{B.2})$$

$$= R_0 \begin{bmatrix} \sum_{i=1}^n w_i & \sum_{i=1}^n w_i & \dots & \sum_{i=1}^n w_i \\ \sum_{i=1}^n w_i & \sum_{i=1}^n w_i & \dots & \sum_{i=1}^n w_i \\ \vdots & \vdots & \ddots & \vdots \\ \sum_{i=1}^n w_i & \sum_{i=1}^n w_i & \dots & \sum_{i=1}^n w_i \end{bmatrix} \begin{bmatrix} w_1 \\ w_2 \\ \vdots \\ w_n \end{bmatrix} \quad (\text{B.3})$$

$$= R_0 \left(w_1 \sum_{i=1}^n w_i + w_2 \sum_{i=1}^n w_i \ \dots \ + w_n \sum_{i=1}^n w_i \right), \quad (\text{B.4})$$

$$\mathbf{w}^T \mathbf{R}_0 \mathbf{w} = R_0 \left(\sum_{i=1}^n w_i \right) \left(\sum_{i=1}^n w_i \right) \geq 0. \quad (\text{B.5})$$

Equation (B.5) shows that \mathbf{R}_0 is a positive-semi-definite matrix. On the other hand, \mathbf{R}_b is a diagonal matrix with positive elements, and therefore is a positive definite matrix. Thus, one can write

$$\begin{aligned} \mathbf{w}^T \mathbf{R} \mathbf{w} &= \mathbf{w}^T (\mathbf{R}_0 + \mathbf{R}_b) \mathbf{w} \\ &= \mathbf{w}^T \mathbf{R}_0 \mathbf{w} + \mathbf{w}^T \mathbf{R}_b \mathbf{w} > 0. \quad \square \end{aligned} \quad (\text{B.6})$$

Lemma B.0.2 *If $L_i \neq 0$ ($i = 1, 2, \dots, n$), then \mathbf{L} in equation (2.29) is a positive-definite matrix.*

Proof The proof is the same as the proof of Lemma B.0.1. \square

Appendix C

Proof of Equation (2.52)

Lemma C.0.3 *The equation (2.49) is equivalent to*

$$\prod_{i=1}^n \beta_i + \sum_{i=1}^n (\alpha_i \prod_{\substack{k=1 \\ k \neq i}}^n \beta_k) = 0. \quad (\text{C.1})$$

Proof Rewriting the equation (2.49) gives

$$\begin{vmatrix} \alpha_1 + \beta_1 & \alpha_2 & \alpha_3 & \cdots & \alpha_n \\ \alpha_1 & \alpha_2 + \beta_2 & \alpha_3 & \cdots & \alpha_n \\ \alpha_1 & \alpha_2 & \alpha_3 + \beta_3 & \cdots & \alpha_n \\ \vdots & \vdots & \vdots & \ddots & \vdots \\ \alpha_1 & \alpha_2 & \alpha_3 & \cdots & \alpha_n + \beta_n \end{vmatrix} = 0. \quad (\text{C.2})$$

Subtracting all the rows of the left-side of (C.2) (except for the last row) from their below rows, one obtains

$$\begin{vmatrix} \alpha_1 + \beta_1 & \alpha_2 & \alpha_3 & \alpha_4 & \alpha_5 & \cdots & \alpha_n \\ -\beta_1 & \beta_2 & 0 & 0 & 0 & \cdots & 0 \\ 0 & -\beta_2 & \beta_3 & 0 & 0 & \cdots & 0 \\ 0 & 0 & -\beta_3 & \beta_4 & 0 & \cdots & 0 \\ 0 & 0 & 0 & -\beta_4 & \beta_5 & \cdots & 0 \\ \vdots & \vdots & \vdots & \vdots & \vdots & \ddots & \vdots \\ 0 & 0 & 0 & 0 & 0 & \cdots & \beta_n \end{vmatrix} = 0. \quad (\text{C.3})$$

Expanding the determinant of (C.3), one can writes

$$\begin{aligned}
& (\alpha_1 + \beta_1) \begin{vmatrix} \beta_2 & 0 & 0 & 0 & \cdots & 0 \\ -\beta_2 & \beta_3 & 0 & 0 & \cdots & 0 \\ 0 & -\beta_3 & \beta_4 & 0 & \cdots & 0 \\ 0 & 0 & -\beta_4 & \beta_5 & \cdots & 0 \\ \vdots & \vdots & \vdots & \vdots & \ddots & \vdots \\ 0 & 0 & 0 & 0 & \cdots & \beta_n \end{vmatrix} - \alpha_2 \begin{vmatrix} -\beta_1 & 0 & 0 & 0 & \cdots & 0 \\ 0 & \beta_3 & 0 & 0 & \cdots & 0 \\ 0 & -\beta_3 & \beta_4 & 0 & \cdots & 0 \\ 0 & 0 & -\beta_4 & \beta_5 & \cdots & 0 \\ \vdots & \vdots & \vdots & \vdots & \ddots & \vdots \\ 0 & 0 & 0 & 0 & \cdots & \beta_n \end{vmatrix} \\
& + \alpha_3 \begin{vmatrix} -\beta_1 & \beta_2 & 0 & 0 & \cdots & 0 \\ 0 & -\beta_2 & 0 & 0 & \cdots & 0 \\ 0 & 0 & \beta_4 & 0 & \cdots & 0 \\ 0 & 0 & -\beta_4 & \beta_5 & \cdots & 0 \\ \vdots & \vdots & \vdots & \vdots & \ddots & \vdots \\ 0 & 0 & 0 & 0 & \cdots & \beta_n \end{vmatrix} - \alpha_4 \begin{vmatrix} -\beta_1 & \beta_2 & 0 & 0 & \cdots & 0 \\ 0 & -\beta_2 & \beta_3 & 0 & \cdots & 0 \\ 0 & 0 & -\beta_3 & 0 & \cdots & 0 \\ 0 & 0 & 0 & \beta_5 & \cdots & 0 \\ \vdots & \vdots & \vdots & \vdots & \ddots & \vdots \\ 0 & 0 & 0 & 0 & \cdots & \beta_n \end{vmatrix} \\
& + \cdots + (-1)^{(n-1)} \alpha_n \begin{vmatrix} -\beta_1 & \beta_2 & 0 & 0 & \cdots & 0 \\ 0 & -\beta_2 & \beta_3 & 0 & \cdots & 0 \\ 0 & 0 & -\beta_3 & \beta_5 & \cdots & 0 \\ 0 & 0 & 0 & -\beta_5 & \cdots & 0 \\ \vdots & \vdots & \vdots & \vdots & \ddots & \vdots \\ 0 & 0 & 0 & 0 & \cdots & -\beta_{(n-1)} \end{vmatrix} = 0.
\end{aligned} \tag{C.4}$$

Calculating the determinants of (C.4), one obtains

$$(\alpha_1 + \beta_1) \prod_{i=2}^n \beta_i + \alpha_2 \prod_{\substack{k=1 \\ k \neq 2}}^n \beta_k + \alpha_3 \prod_{\substack{k=1 \\ k \neq 3}}^n \beta_k + \cdots + \alpha_n \prod_{k=1}^{n-1} \beta_k = 0. \tag{C.5}$$

Rewriting (C.5), one concludes

$$\prod_{i=1}^n \beta_i + \sum_{i=1}^n (\alpha_i \prod_{\substack{k=1 \\ k \neq i}}^n \beta_k) = 0. \quad \square \tag{C.6}$$

Appendix D

Study System Parameters for Chapter 2

Table D.1 reports the parameters of the dc system for simulation studies and model validation in Chapter 2. The parameters of the battery chargers for the simulations are given in Table D.2.

Table D.1: Study dc System Parameters

Quantity	Value	Comment
Cable resistance	99.1 $m\Omega/km$ [72]	Conductor area: 185 mm^2
Cable inductance	547.5 $\mu H/km$ [72]	Conductor area: 185 mm^2
R_i ($i = 0, 1, \dots, 6$)	19.8 $m\Omega$	200-m cable segments
L_i ($i = 0, 1, \dots, 6$)	109.5 μH	200-m cable segments
C_i ($i = 1, 2, \dots, 6$)	2000 μF	
R_s	2.38 $m\Omega$	per-phase tie reactor resistance
L_s	57 μH	per-phase tie reactor inductance
C	9625 μF	dc-side capacitor of the central VSC
Switching frequency	3420 Hz	
Nominal dc-bus voltage	480 V	
$K_d(s), K_q(s)$	$\frac{0.5725s+32.6}{s}$	Current controllers
$K_V(s)$	$\frac{-32139.6(s+70)(s+657)}{s(s+9144)(s+974.1)}$ Ω^{-1}	dc voltage compensator

Table D.2: Battery Chargers Parameters

Quantity	Value	Comment
Nominal power rating of the battery chargers	90 kW	
R_{Bi} ($i = 1, 2, \dots, 5$)	5 $m\Omega$	
L_{Bi} ($i = 1, 2, \dots, 5$)	690 μH	
V_{bati} ($i = 1, 2, \dots, 5$)	320 V	Battery voltage
$K_i(s)$ ($i = 1, 2, \dots, 5$)	$\frac{1.38s+11.76}{s}$	battery charger compensator
τ_{Bi} ($i = 1, 2, \dots, 5$)	0.5 ms	battery charger time constant

Appendix E

Study System Parameters for Chapter 3

Table E.1 reports the parameters of the dc system for simulation studies and model validation in Chapter 3. The parameters of the battery chargers for the simulations are given in Table E.2.

Table E.1: Study dc System Parameters

Quantity	Value	Comment
Cable resistance	99.1 $m\Omega/km$	Conductor area: 185 mm^2
Cable inductance	547.5 $\mu H/km$	Conductor area: 185 mm^2
R, R_1, R_2, R_3	19.8 $m\Omega$	200-m cable segments
L, L_1, L_2, L_3	109.5 μH	200-m cable segments
C_1, C_2, C_3	1500 μF	
R_s	2.38 $m\Omega$	per-phase tie reactor resistance
L_s	86 μH	per-phase tie reactor inductance
C	9625 μF	
ac grid voltage	227 V	line-to-line, rms
V_s	185 V	
ac grid frequency	60 Hz	
Switching frequency	3420 Hz	
Nominal dc-bus voltage	480 V	
$G_p(s)$	$\frac{10000}{s+10000}$	
$K_V(s)$	$\frac{-32139.6(s+70)(s+657)}{s(s+9144)(s+974.1)}$ Ω^{-1}	dc voltage compensator

Table E.2: Battery Chargers Parameters

Quantity	Value	Comment
Nominal battery charger power rating	90 kW	
R_{B1}, R_{B2}	5 m Ω	
L_{B1}, L_{B2}	690 μH	
V_{bat1}, V_{bat2}	320 V	Battery voltage
$K_1(s), K_2(s)$	$\frac{1.38s+11.76}{s} \Omega$	battery charger compensator
τ_{B1}, τ_{B2}	0.5 ms	battery charger time constant

Appendix F

Study System Parameters for Chapter 4

Table F.1 reports the parameters of the dc system for simulation studies in Chapter 4.

Table F.1: Parameters of the Study System in Chapter 4

Quantity	Value	Comment
N	50	The maximum number of PEVs
Base load peak	400 kW	equivalent to power consumption of 200 household
Power demand limit	440 kW	10% more than the base load peak
Power generation limit	0 kW	
P_{rat_i} ($i = 1, \dots, N$)	40 kW	Battery chargers' power rating
E_{cap_i} ($i = 1, \dots, N$)	40 kWh	PEVs' battery capacity
η_i ($i=1, \dots, N$)	0.9	Battery chargers' efficiency
v_{dc}	480 V	dc bus nominal voltage
Cable resistance	99.1 $m\Omega/km$	Conductor area: 185 mm^2
R_i ($i = 0, 1, \dots, N$)	19.8 $m\Omega$	200m cable section
$P_{dc_{max}}$	2.85 MW	

Bibliography

- [1] D. P. Tuttle and R. Baldick, “The evolution of plug-in electric vehicle-grid interactions,” *Smart Grid, IEEE Transactions on*, vol. 3, no. 1, pp. 500–505, 2012.
- [2] K. Clement-Nyns, E. Haesen, and J. Driesen, “The impact of charging plug-in hybrid electric vehicles on a residential distribution grid,” *Power Systems, IEEE Transactions on*, vol. 25, no. 1, pp. 371–380, 2010.
- [3] M. C. Kisacikoglu, B. Ozpineci, and L. M. Tolbert, “Examination of a phev bidirectional charger system for v2g reactive power compensation,” in *Applied Power Electronics Conference and Exposition (APEC), 2010 Twenty-Fifth Annual IEEE*. IEEE, 2010, pp. 458–465.
- [4] D. C. Erb, O. C. Onar, and A. Khaligh, “Bi-directional charging topologies for plug-in hybrid electric vehicles,” in *Applied Power Electronics Conference and Exposition (APEC), 2010 Twenty-Fifth Annual IEEE*. IEEE, 2010, pp. 2066–2072.
- [5] Z. Amjadi and S. S. Williamson, “Modeling, simulation, and control of an advanced Luo converter for plug-in hybrid electric vehicle energy-storage system,” *Vehicular Technology, IEEE Transactions on*, vol. 60, no. 1, pp. 64–75, 2011.
- [6] C. Canizares, J. Nathwani, K. Bhattacharya, M. Fowler, M. Kazerani, R. Fraser, I. Rowlands, and H. Gabbar, “Towards an ontario action plan for plug-in-electric vehicles (pevs),” *Waterloo Institute for Sustainable Energy, University of Waterloo*, 2010.
- [7] S. Deilami, A. S. Masoum, P. S. Moses, and M. A. Masoum, “Real-time coordination of plug-in electric vehicle charging in smart grids to minimize power losses and improve voltage profile,” *Smart Grid, IEEE Transactions on*, vol. 2, no. 3, pp. 456–467, 2011.

- [8] The Chevrolet Volt website. [Online]. Available: <http://www.chevrolet.com/volt-electric-car.html>
- [9] The Mitsubishi Motor Sales of Canada website. [Online]. Available: <http://www.mitsubishi-motors.ca/en/vehicles/i-miev/2014/specs/>
- [10] The Ford Motor Company website. [Online]. Available: <http://www.ford.com/cars/fusion/specifications/engine/>
- [11] The Nissan Canada website. [Online]. Available: <http://www.nissan.ca/en/electric-cars/leaf/>
- [12] The Toyota Canada website. [Online]. Available: <http://www.toyota.ca/toyota/en/vehicles/prius-plugin/overview>
- [13] The Tesla Motor website. [Online]. Available: http://www.teslamotors.com/en_CA/models/features#/battery
- [14] *SAE Electric Vehicle and Plug-in Hybrid Electric Vehicle Conductive Charge Coupler*, SAE Standard J1772, Jan. 2010.
- [15] M. Yilmaz and P. T. Krein, “Review of battery charger topologies, charging power levels, and infrastructure for plug-in electric and hybrid vehicles,” *Power Electronics, IEEE Transactions on*, vol. 28, no. 5, pp. 2151–2169, 2013.
- [16] A. Khaligh and S. Dusmez, “Comprehensive topological analysis of conductive and inductive charging solutions for plug-in electric vehicles,” *Vehicular Technology, IEEE Transactions on*, vol. 61, no. 8, pp. 3475–3489, 2012.
- [17] Y. Du, X. Zhou, S. Bai, S. Lukic, and A. Huang, “Review of non-isolated bi-directional dc-dc converters for plug-in hybrid electric vehicle charge station application at municipal parking decks,” in *Applied Power Electronics Conference and Exposition (APEC), 2010 Twenty-Fifth Annual IEEE*. IEEE, 2010, pp. 1145–1151.
- [18] S. Bai, D. Yu, and S. Lukic, “Optimum design of an ev/phev charging station with dc bus and storage system,” in *Energy Conversion Congress and Exposition (ECCE), 2010 IEEE*. IEEE, 2010, pp. 1178–1184.
- [19] S. Bai and S. M. Lukic, “Unified active filter and energy storage system for an mw electric vehicle charging station,” *Power Electronics, IEEE Transactions on*, vol. 28, no. 12, pp. 5793–5803, 2013.

- [20] M. Tabari and A. Yazdani, "A dc distribution system for power system integration of plug-in hybrid electric vehicles," in *Power and Energy Society General Meeting (PES), 2013 IEEE*. IEEE, 2013, pp. 1–5.
- [21] Y. Gurkaynak and A. Khaligh, "Control and power management of a grid connected residential photovoltaic system with plug-in hybrid electric vehicle (phev) load," in *Applied Power Electronics Conference and Exposition, 2009. APEC 2009. Twenty-Fourth Annual IEEE*. IEEE, 2009, pp. 2086–2091.
- [22] A. Mohamed, V. Salehi, T. Ma, and O. Mohammed, "Real-time energy management algorithm for plug-in hybrid electric vehicle charging parks involving sustainable energy," *Sustainable Energy, IEEE Transactions on*, vol. 5, no. 2, pp. 577–586, April 2014.
- [23] E. Sortomme and M. A. El-Sharkawi, "Optimal charging strategies for unidirectional vehicle-to-grid," *Smart Grid, IEEE Transactions on*, vol. 2, no. 1, pp. 131–138, 2011.
- [24] C. Jin, J. Tang, and P. Ghosh, "Optimizing electric vehicle charging: a customer's perspective," *Vehicular Technology, IEEE Transactions on*, vol. 62, no. 7, pp. 2919–2927, 2013.
- [25] E. Sortomme and M. A. El-Sharkawi, "Optimal scheduling of vehicle-to-grid energy and ancillary services," *Smart Grid, IEEE Transactions on*, vol. 3, no. 1, pp. 351–359, 2012.
- [26] G. Byeon, T. Yoon, S. Oh, and G. Jang, "Energy management strategy of the dc distribution system in buildings using the ev service model," *Power Electronics, IEEE Transactions on*, vol. 28, no. 4, pp. 1544–1554, 2013.
- [27] P. Tulpule, S. Yurkovich, J. Wang, and G. Rizzoni, "Hybrid large scale system model for a dc microgrid," in *American Control Conference (ACC), 2011*. IEEE, 2011, pp. 3899–3904.
- [28] A. Emadi, A. Khaligh, C. H. Rivetta, and G. A. Williamson, "Constant power loads and negative impedance instability in automotive systems: definition, modeling, stability, and control of power electronic converters and motor drives," *Vehicular Technology, IEEE Transactions on*, vol. 55, no. 4, pp. 1112–1125, 2006.

- [29] A. Kwasinski and C. N. Onwuchekwa, “Dynamic behavior and stabilization of dc microgrids with instantaneous constant-power loads,” *Power Electronics, IEEE Transactions on*, vol. 26, no. 3, pp. 822–834, 2011.
- [30] G.-S. Seo, J. Baek, K. Choi, H. Bae, and B. Cho, “Modeling and analysis of dc distribution systems,” in *Power Electronics and ECCE Asia (ICPE & ECCE), 2011 IEEE 8th International Conference on*. IEEE, 2011, pp. 223–227.
- [31] P. Magne, B. Nahid-Mobarakeh, and S. Pierfederici, “General active global stabilization of multiloads dc-power networks,” *Power Electronics, IEEE Transactions on*, vol. 27, no. 4, pp. 1788–1798, 2012.
- [32] A. Riccobono, J. Siegers, and E. Santi, “Stabilizing positive feed-forward control design for a dc power distribution system using a passivity-based stability criterion and system bus impedance identification,” in *Applied Power Electronics Conference and Exposition (APEC), 2014 Twenty-Ninth Annual IEEE*. IEEE, 2014, pp. 1139–1146.
- [33] W. Zhu, S. Pekarek, J. Jatskevich, O. Wasynczuk, and D. Delisle, “A model-in-the-loop interface to emulate source dynamics in a zonal dc distribution system,” *Power Electronics, IEEE Transactions on*, vol. 20, no. 2, pp. 438–445, 2005.
- [34] S. Anand and B. Fernandes, “Reduced-order model and stability analysis of low-voltage dc microgrid,” *Industrial Electronics, IEEE Transactions on*, vol. 60, no. 11, pp. 5040–5049, 2013.
- [35] D. Marx, P. Magne, B. Nahid-Mobarakeh, S. Pierfederici, and B. Davat, “Large signal stability analysis tools in dc power systems with constant power loads and variable power loads a review,” *Power Electronics, IEEE Transactions on*, vol. 27, no. 4, pp. 1773–1787, 2012.
- [36] S. Sudhoff, K. Corzine, S. Glover, H. Hegner, and H. Robey Jr, “Dc link stabilized field oriented control of electric propulsion systems,” *Energy Conversion, IEEE Transactions on*, vol. 13, no. 1, pp. 27–33, 1998.
- [37] E. Jamshidpour, B. Nahid-Mobarakeh, P. Poure, S. Pierfederici, F. Meibody-Tabar, and S. Saadate, “Distributed active resonance suppression in hybrid dc power systems under unbalanced load conditions,” *Power Electronics, IEEE Transactions on*, vol. 28, no. 4, pp. 1833–1842, 2013.

- [38] P. Liutanakul, A.-B. Awan, S. Pierfederici, B. Nahid-Mobarakeh, and F. Meibody-Tabar, "Linear stabilization of a dc bus supplying a constant power load: A general design approach," *Power Electronics, IEEE Transactions on*, vol. 25, no. 2, pp. 475–488, 2010.
- [39] D. Leblanc, B. Nahid-Mobarakeh, B. Pham, S. Pierfederici, and B. Davat, "Stability analysis and active stabilization by a centralized stabilizer of voltage-source-rectifier loads in ac microgrids," in *Industry Applications Society Annual Meeting, 2013 IEEE*. IEEE, 2013, pp. 1–8.
- [40] A. M. Rahimi and A. Emadi, "Active damping in dc/dc power electronic converters: A novel method to overcome the problems of constant power loads," *Industrial Electronics, IEEE Transactions on*, vol. 56, no. 5, pp. 1428–1439, 2009.
- [41] A. Emadi and M. Ehsani, "Negative impedance stabilizing controls for pwm dc-dc converters using feedback linearization techniques," in *Energy Conversion Engineering Conference and Exhibit, 2000.(IECEC) 35th Intersociety*, vol. 1. IEEE, 2000, pp. 613–620.
- [42] N. Leemput, F. Geth, J. Van Roy, A. Delnooz, J. Buscher, and J. Driesen, "Impact of electric vehicle on-board single-phase charging strategies on a flemish residential grid," *Smart Grid, IEEE Transactions on*, vol. 5, no. 4, pp. 1815–1822, July 2014.
- [43] I. Sharma, C. Canizares, and K. Bhattacharya, "Smart charging of pevs penetrating into residential distribution systems," *Smart Grid, IEEE Transactions on*, vol. 5, no. 3, pp. 1196–1209, 2014.
- [44] A. Schuller, B. Dietz, C. Flath, and C. Weinhardt, "Charging strategies for battery electric vehicles: Economic benchmark and v2g potential," *Power Systems, IEEE Transactions on*, vol. 29, no. 5, pp. 2014–2022, Sept 2014.
- [45] J. Van Roy, N. Leemput, F. Geth, J. Buscher, R. Salenbien, and J. Driesen, "Electric vehicle charging in an office building microgrid with distributed energy resources," *Sustainable Energy, IEEE Transactions on*, vol. 5, no. 4, pp. 1389–1396, Oct 2014.
- [46] Y. Zheng, Z. Y. Dong, Y. Xu, K. Meng, J. H. Zhao, and J. Qiu, "Electric vehicle battery charging/swap stations in distribution systems: Comparison study and optimal planning," *Power Systems, IEEE Transactions on*, vol. 29, no. 1, pp. 221–229, Jan 2014.

- [47] Y. He, B. Venkatesh, and L. Guan, "Optimal scheduling for charging and discharging of electric vehicles," *Smart Grid, IEEE Transactions on*, vol. 3, no. 3, pp. 1095–1105, 2012.
- [48] E. Sortomme, M. M. Hindi, S. J. MacPherson, and S. Venkata, "Coordinated charging of plug-in hybrid electric vehicles to minimize distribution system losses," *Smart Grid, IEEE Transactions on*, vol. 2, no. 1, pp. 198–205, 2011.
- [49] M. Zhang and J. Chen, "The energy management and optimized operation of electric vehicles based on microgrid," *Power Delivery, IEEE Transactions on*, vol. 29, no. 3, pp. 1427–1435, June 2014.
- [50] *PSCAD/EMTDC ver. 4.2*, Manitoba HVDC Research Centre, Winnipeg, MB, Canada.
- [51] T.-F. Wu, C.-H. Chang, L.-C. Lin, G.-R. Yu, and Y.-R. Chang, "Dc-bus voltage control with a three-phase bidirectional inverter for dc distribution systems," *Power Electronics, IEEE Transactions on*, vol. 28, no. 4, pp. 1890–1899, 2013.
- [52] D. Salomonsson, L. Soder, and A. Sannino, "An adaptive control system for a dc microgrid for data centers," *Industry Applications, IEEE Transactions on*, vol. 44, no. 6, pp. 1910–1917, Nov 2008.
- [53] A. Yazdani and R. Iravani, *Voltage-sourced converters in power systems: modeling, control, and applications*. John Wiley & Sons, 2010.
- [54] P. Kulshrestha, K. Swaminathan, M.-Y. Chow, and S. Lukic, "Evaluation of zigbee communication platform for controlling the charging of phev's at a municipal parking deck," in *Vehicle Power and Propulsion Conference, 2009. VPPC'09. IEEE*. IEEE, 2009, pp. 1211–1214.
- [55] S. Skogestad and I. Postlethwaite, *Multivariable feedback control: analysis and design*. Wiley New York, 2007, vol. 2.
- [56] C.-T. Chen, *Linear system theory and design*. Oxford University Press, Inc., 1999.
- [57] M. Chen and G. A. Rincon-Mora, "Accurate electrical battery model capable of predicting runtime and iv performance," *Energy conversion, iee transactions on*, vol. 21, no. 2, pp. 504–511, 2006.

- [58] Z. Miao, L. Xu, V. Disfani, and L. Fan, "An soc-based battery management system for microgrids," *Smart Grid, IEEE Transactions on*, vol. 5, no. 2, pp. 966–973, March 2014.
- [59] W. Du, J. Zhang, Y. Zhang, and Z. Qian, "Stability criterion for cascaded system with constant power load," *Power Electronics, IEEE Transactions on*, vol. 28, no. 4, pp. 1843–1851, 2013.
- [60] X. Zhang, D. M. Vilathgamuwa, K.-J. Tseng, B. S. Bhangu, and C. J. Gajanayake, "Power buffer with model predictive control for stability of vehicular power systems with constant power loads," *Power Electronics, IEEE Transactions on*, vol. 28, no. 12, pp. 5804–5812, 2013.
- [61] P. Kulshrestha, L. Wang, M.-Y. Chow, and S. Lukic, "Intelligent energy management system simulator for phev at municipal parking deck in a smart grid environment," in *Power & Energy Society General Meeting, 2009. PES'09. IEEE*. IEEE, 2009, pp. 1–6.
- [62] Y. Du, S. Lukic, B. Jacobson, and A. Huang, "Review of high power isolated bi-directional dc-dc converters for phev/ev dc charging infrastructure," in *Energy Conversion Congress and Exposition (ECCE), 2011 IEEE*. IEEE, 2011, pp. 553–560.
- [63] W. Su, H. Eichi, W. Zeng, and M.-Y. Chow, "A survey on the electrification of transportation in a smart grid environment," *Industrial Informatics, IEEE Transactions on*, vol. 8, no. 1, pp. 1–10, 2012.
- [64] N. Bottrell, M. Prodanovic, and T. Green, "Dynamic stability of a microgrid with an active load," *Power Electronics, IEEE Transactions on*, vol. 28, no. 11, pp. 5107–5119, Nov 2013.
- [65] M. Tabari and A. Yazdani, "A mathematical model for stability analysis of a dc distribution system for power system integration of plug-in electric vehicles," *Vehicular Technology, IEEE Transactions on*, Early Access, 2014.
- [66] The Independent Electricity System Operator (IESO) website. [Online]. Available: <http://www.ieso.ca/>
- [67] A. Schuller, B. Dietz, C. Flath, and C. Weinhardt, "Charging strategies for battery electric vehicles: Economic benchmark and v2g potential," *Power Systems, IEEE Transactions on*, vol. 29, no. 5, pp. 2014–2022, Sept 2014.

- [68] Y. Tang, Y. Zhang, J. Deng, J. Wei, H. L. Tam, B. K. Chandran, Z. Dong, Z. Chen, and X. Chen, “Mechanical force-driven growth of elongated bending tio₂-based nanotubular materials for ultrafast rechargeable lithium ion batteries,” *Wiley, Advanced Materials Journal*, vol. 26, no. 35, pp. 6111–6118, 2014.
- [69] L. Herrera, E. Inoa, F. Guo, J. Wang, and H. Tang, “Small-signal modeling and networked control of a phev charging facility,” *Industry Applications, IEEE Transactions on*, vol. 50, no. 2, pp. 1121–1130, March 2014.
- [70] J. Beerten, S. Cole, and R. Belmans, “Generalized steady-state vsc mt dc model for sequential ac/dc power flow algorithms,” *Power Systems, IEEE Transactions on*, vol. 27, no. 2, pp. 821–829, 2012.
- [71] T. L. Vandoorn, B. Meersman, J. D. De Kooning, and L. Vandeveldel, “Analogy between conventional grid control and islanded microgrid control based on a global dc-link voltage droop,” *Power Delivery, IEEE Transactions on*, vol. 27, no. 3, pp. 1405–1414, 2012.
- [72] Nexans Olex Cable Handbook. [Online]. Available: <http://www.olex.com.au/>

Curriculum Vitae

Name: Mansour Tabari

Post-Secondary Education and Degree: Western University
London, ON, Canada

2010 - present, Ph.D. in Electrical Engineering

K.N.T. University of Technology
Tehran, Iran

1995 - 1998, M.E.Sc. in Electrical Engineering

K.N.T. University of Technology
Tehran, Iran

1989 - 1994, B.Sc. in Electrical Engineering

Honours and Awards:

- Western Graduate Research Scholarship, Sep. 2010 - present.
- First Award for the best presentation in the Western Graduate Symposium, 2013.

Related Work

Experience:

- Research and Teaching Assistant, Western University, 2010 - present.
- Director and Senior Design Engineer, Depelmaan Pardaz Ltd., Tehran, Iran 2004 - 2010.
- Project Manager and Senior Design Engineer, Maharan Eng. Corp., Tehran, Iran 1999 - 2004.

Publications:

Peer-Reviewed Journals:

- M. Tabari and A. Yazdani, "A Mathematical Model for Stability Analysis of A dc Distribution System for Power System Integration of Plug-In Electric Vehicles," Accepted to be published in *IEEE Transactions on Vehicular Technology*, IEEE Xplore Early Access, 2014.
- M. Tabari and A. Yazdani, "Stability of a dc Distribution System for Power System Integration of Plug-In Hybrid Electric Vehicles," *Smart Grid, IEEE Transactions on*, vol.5, no.5, pp. 2564-2573, Sept. 2014.

- M. Tabari and A. Yazdani, “An Energy Management Strategy for A dc Distribution System for Power System Integration of Plug-In Electric Vehicles,” Submitted to *IEEE Transactions on Smart Grid*, Sept. 2014.

Referred Conferences:

- M. Tabari and A. Yazdani, “A DC Distribution System for Power System Integration of Plug-In Hybrid Electric Vehicles,” in Power and Energy Society General Meeting (PES), 2013 IEEE, 2013, pp. 1-5.